

Design of a Sodium-cooled Epithermal Long-term Exploration Nuclear Engine

By
Peter Yarsky

B.S. Nuclear Engineering and Engineering Physics
Rensselaer Polytechnic Institute, 2002

SUBMITTED TO THE DEPARTMENT OF NUCLEAR ENGINEERING IN
PARTIAL FULFILLMENT OF THE REQUIREMENTS FOR A DEGREE OF

MASTER OF SCIENCE IN NUCLEAR ENGINEERING
AT THE
MASSACHUSETTS INSTITUTE OF TECHNOLOGY

September 2004

© 2004 Massachusetts Institute of Technology. All rights reserved.

Author

Peter Yarsky
Department of Nuclear Engineering
June 28, 2004

Certified by

Professor Andrew C. Kadak
Thesis Advisor

Certified by

Professor Michael J. Driscoll
Thesis Reader

Accepted by.....

Professor Jeffrey A. Coderre
Chairman, Department Committee on Graduate Students

Design of a Sodium-cooled Epithermal Long-term Exploration Nuclear Engine

By

Peter Yarsky

Submitted to the Nuclear Engineering Department on June 28, 2004 in partial fulfillment of the requirements for a degree of Master of Science in Nuclear Engineering at the Massachusetts Institute of Technology.

Abstract

To facilitate the mission to Mars initiative, the current work has focused on conceptual designs for transformational and enabling space nuclear reactor technologies. A matrix of design alternatives for both the reactor core and the power conversion unit were considered. Based on a preliminary screening of technologies using simplified analyses, a conceptual design was established for more detailed design work.

The boiling sodium Rankine cycle was selected for the power conversion unit, and the reactor core is an ultra high power density core with highly enriched uranium fuel. The sodium Rankine cycle has many advantages, lending to a highly efficient radiator and compact reactor core. The sodium-cooled, epithermal long-term exploration nuclear engine (SELENE) is designed to be scalable to meet many differing mission requirements.

The SELENE core is comprised of Nb-1Zr clad, lead bonded, UC plates in a honeycomb pattern. The fuel plates are arranged into a rectangular grid, roughly 25cm on each end. The fuel is in two zones, one is 97 a/o enriched in ^{235}U and the other is 70 a/o enriched in ^{235}U . The core is a fast spectrum reactor, BeO reflected, and ex-core controlled.

Three designs are proposed, the first is for a 10 MWth / 1.0 MWe Low Temperature (1300 K) system (SELENE-10-LT) and the second for a 10 MWth / 1.2 MWe High Temperature (1500 K) system (SELENE-10-HT) and the third for a 27 MWth / 2.6 MWe system (SELENE-30).

All of these designs utilize essentially the same system architecture. Three designs are proposed so that low power variants can be used to verify the technology and develop experience. The reactor systems may then be upgraded to a higher power level. The system lifetime is 9 effective full power months, corresponding roughly to a single trip from Earth to Mars and back.

Thesis Supervisor: Dr. Andrew C. Kadak
Title: Professor of the Practice, Nuclear Engineering

Table of Contents

1.0	INTRODUCTION	9
1.1	BACKGROUND.....	9
1.2	SCOPE OF THE CURRENT WORK.....	11
1.3	ORGANIZATION OF THIS THESIS.....	12
2.0	ARGON BRAYTON CYCLE	13
2.1	METHODOLOGY.....	13
2.2	THEORY.....	14
2.3	RESULTS.....	16
2.4	DISCUSSION.....	18
3.0	THERMIONIC POWER CONVERSION	21
3.1	SINGLE LAYER DESIGN.....	21
3.2	DUAL LAYER DESIGN.....	23
3.3	DIRECT CONTACT SINGLE LAYER.....	24
3.4	COMPARISONS.....	25
3.5	CONCLUSIONS.....	25
4.0	SIMPLIFIED SODIUM RANKINE CYCLE	27
4.1	SIMPLE RANKINE CYCLE SPECIFICATIONS.....	27
4.2	IDEAL ANALYSIS.....	27
4.3	REAL ANALYSIS.....	31
4.4	HIGH TEMPERATURE CYCLE.....	31
4.5	DISCUSSION.....	32
5.0	RADIOISOTOPE DOPING TO PREVENT COOLANT FREEZING	33
5.1	RADIOISOTOPES.....	33
5.2	ANALYSIS.....	33
5.3	CALCULATIONS.....	35
5.4	CONCLUSIONS.....	36
6.0	HEU FUELED ULTRA HIGH POWER DENSITY CORE	37
6.1	DESIGN CHANGES.....	37
6.2	CORE SIZE.....	38
6.3	CORE LIFE STUDIES.....	39
6.4	CONTROL MECHANISM.....	39
6.5	VOID REACTIVITY.....	40
6.6	CONCLUSIONS.....	40
7.0	SUMMARY AND SELENE OVERVIEW	43
8.0	SODIUM RANKINE CYCLE	47
8.1	BASIC CYCLE.....	47
8.2	TWO-PHASE FLOW IN MICRO GRAVITY.....	50
8.3	VAPOR SEPARATION.....	50
8.4	JET PUMP.....	50
9.0	THERMAL HYDRAULIC ANALYSIS	51
9.1	AVERAGE CHANNEL FINITE ELEMENT METHODOLOGY.....	51
9.2	LIQUID REGIME.....	54
9.3	TWO-PHASE REGIME.....	57

9.4	VAPOR REGIME.....	59
9.5	SELENE-10-LT.....	60
9.6	SELENE-10-HT.....	61
9.7	SELENE-30.....	62
10.0	REACTOR PHYSICS AND BURNUP.....	65
10.1	REACTIVITY LIMITED BURNUP.....	68
10.2	BURNABLE POISONS	71
10.3	POWER PEAKING FACTORS.....	73
10.4	FUEL SWELLING AND FISSION GAS.....	78
11.0	HOT CHANNEL ANALYSIS	79
12.0	OVERPOWER CONDITION AND REACTIVITY FEEDBACK.....	81
12.1	SPECTRUM HARDENING	82
12.2	LEAKAGE	83
12.3	DOPPLER FEEDBACK.....	83
13.0	LAUNCH ACCIDENTS	85
13.1	SODIUM REACTION WITH WATER.....	85
13.2	WATER MODERATION AND CRITICALITY	86
14.0	CONCLUSIONS AND RECOMMENDED FUTURE WORK	87
15.0	REFERENCES.....	89
16.0	APPENDICES.....	91
16.1	APPENDIX A: SELENE-30 MCNP4C2 INPUT DECK	92
16.2	APPENDIX B: SELENE-10-HT MCODE INPUT DECK.....	105
16.3	APPENDIX C: SELENE-30 AVERAGE CHANNEL THERMAL HYDRAULIC DATA.....	106
16.4	APPENDIX D: SELENE-30 1.3PPF HOT CHANNEL THERMAL HYDRAULIC DATA.....	110

LIST OF FIGURES

FIGURE 1:	BRAYTON CYCLE SCHEMATIC.....	14
FIGURE 2:	NET USEFUL WORK AS A FUNCTION OF MINIMUM CYCLE TEMPERATURE.	17
FIGURE 3:	DIAGRAM OF THE SINGLE LAYER THERMIONIC CONVERSION POWER PACKAGE.....	22
FIGURE 4:	CONCEPTUAL FUEL PLATE FOR SINGLE LAYER, DIRECT CONTACT TIC.....	25
FIGURE 5:	SODIUM SATURATION PROPERTIES	28
FIGURE 6:	EXIT QUALITY VS. OUTLET PRESSURE.....	29
FIGURE 7:	NET WORK VS. OUTLET PRESSURE	30
FIGURE 8:	UHPDC LAYOUT	37
FIGURE 9:	CORE MULTIPLICATION FACTOR AS A FUNCTION OF CORE DIMENSION	38
FIGURE 10:	REACTIVITY HISTORY FOR THE HEU UHPDC.....	39
FIGURE 11:	EFFECT OF CONTROL DEVICE ON BOL EIGENVALUE	40
FIGURE 12:	SIMPLIFIED SELENE SCHEMATIC (NOT-TO-SCALE).	45
FIGURE 13:	IDEAL SODIUM RANKINE CYCLE (EXTRAPOLATED) [TODREAS, ET AL.].	49
FIGURE 14:	UNIT CELL SCHEMATIC	52
FIGURE 15:	AXIAL UNIT CELL MODEL.....	66
FIGURE 16:	RADIAL PLANE CORE MODEL.	67
FIGURE 17:	ISOMETRIC VIEW OF FUEL PLATE ASSEMBLY.	67
FIGURE 18:	PARTIAL REACTIVITY HISTORY FOR SELENE-10.	68
FIGURE 19:	REACTIVITY HISTORY FOR SELENE-30.	70
FIGURE 20:	NORMALIZED FLUX PER UNIT LETHARGY FOR SELENE-10-HT.....	73
FIGURE 21:	AXIAL POWER SHAPE.	74
FIGURE 22:	VARIATION OF THE SODIUM DENSITY WITH AXIAL POSITION.	75
FIGURE 23:	ZONED FULL CORE RADIAL SLICE	76
FIGURE 24:	RADIAL POWER DENSITY VARIATION.....	77
FIGURE 25:	RATIO OF FLUX SPECTRA TO ILLUSTRATE SPECTRUM HARDENING	82

LIST OF TABLES

TABLE I:	CYCLE CHARACTERISTICS.....	17
TABLE II:	SENSITIVITY ANALYSIS	18
TABLE III:	PERFORMANCE MAP.....	31
TABLE IV:	DOPED COOLANT PROPERTIES[PARRINGTON, ET AL.].....	35
TABLE V:	RGP AND HEU COMPARISON.....	41
TABLE VI:	POWER CONVERSION TECHNOLOGY COMPARISON.....	43
TABLE VII:	SATURATED SODIUM PROPERTIES.....	54
TABLE VIII:	SELENE-10-LT OPERATIONAL PARAMETERS.....	61
TABLE IX:	SELENE-10-HT OPERATIONAL PARAMETERS.....	62
TABLE X:	SELENE-30 OPERATIONAL PARAMETERS.....	62
TABLE XI:	SELENE LIFETIME SUMMARY	70
TABLE XII:	RADIAL PEAKING FOR UNIFORM ENRICHMENT.....	76
TABLE XIII:	RADIAL POWER PEAKING IN THE ZONED CORE.	77
TABLE XIV:	HOT CHANNEL RESULTS FOR VARIOUS RADIAL POWER PEAKING FACTORS.....	79
TABLE XV:	DOPPLER REACTIVITY COEFFICIENT DATA.....	84

Author's Note

The author would like to thank Professor Andy Kadak and Professor Michael Driscoll for their guidance and support in completing this thesis. Thanks are also extended to Professor Mujid Kazimi, Professor Neil Todreas, Professor Jeffery Hoffman, and Dr. Walter Kato for their various contributions.

1.0 Introduction

For future space exploration initiatives, large power systems will be required. Specifically for a manned mission to Mars, systems capable of generating several megawatts of electric power will be required. The goal is to develop space nuclear power technologies that will facilitate these initiatives.

1.1 Background

As part of a design course at MIT, an ultra high power density plutonium fueled nuclear reactor core was developed for use in an electric powered propulsion system. The reactor was cooled with molten salt, which was passed through an internal radiator. The power conversion unit was based on next generation thermo-photovoltaic (TPV) technology. The core lifetime was approximately 600 EFPD and the system produced 4 MW of electric power [Dostal, et al.].

For several reasons, this technology will not be implemented in the short term for space exploration. Firstly, it requires TPV to operate at temperatures 100 K higher than what they have been demonstrated to operate at on Earth, and they must operate at higher efficiencies, requiring very high coolant temperatures; hence, the corrosive aspects of the molten salt would require development of next generation structural materials for the radiator.

To facilitate the mission to Mars initiative, a lower power system based on more conventional or state of the art technologies is desired. The scope of the current body of work examines the use of more traditional power conversion technologies to achieve a mid-range power system for short-term space exploration applications that are scalable to high power operations with incremental improvements.

This thesis examines both the thermal hydraulic and physics aspects of designing a nuclear electric power system for space applications. In the physics area, work was done to design a highly enriched uranium (HEU) fueled ultra-high-power-density core (UHPDC). In the area of thermal-hydraulics, the front end of the current work has been to evaluate alternative power conversion schemes. Gas and liquid metal coolants were evaluated in a matrix of power conversion options. Based on simplified analyses, the most promising power conversion strategies were identified.

In any space application, minimizing reactor mass is an ever present objective. However, mass is not the only concern. The motivations behind designing the plutonium core were twofold. Plutonium has a lower critical mass than uranium, and therefore, allows for a smaller core. Reactor Grade Plutonium (RGP), or the spent fuel plutonium from a LWR, was the proposed fuel material, in the form of PuC. RGP is comprised primarily of ^{239}Pu , ^{240}Pu , and ^{241}Pu . ^{239}Pu and ^{241}Pu have very large fission cross sections at both thermal and fast neutron energies. ^{240}Pu , while fissionable in a fast spectrum, is also a fertile material. The RGP core had a relatively shallow reactivity swing through life because uneventful capture in the plutonium isotopes did not reduce the effective inventory of “fissionable” materials.

With HEU fuel, the BOL core must be loaded with excess reactivity to accommodate for the burnup of fissionable ^{235}U , and though this is also the case with RGP fuel, the excess reactivity required is greater. This is because ^{235}U capture produces ^{236}U , which is not as likely to fission as the fertile plutonium isotopes. The greater BOL reactivity complicates the control mechanism design. The design of the HEU core will focus on core dimension requirements, lifetime studies, and design of the reactivity control mechanisms.

The thermal-hydraulic analyses conducted were simplified. Comparisons of potential power cycles were carried out. Previous work has looked a plethora of different options. Static and dynamic power conversion alternatives were explored.

Static conversion refers to power conversion units (PCU) without moving parts. These include thermionic converters (TIC) and thermo-photo-voltaics (TPV). Aside from being simpler, these PCU options also generate DC power.

Dynamic conversion refers to PCUs with moving parts. The primary examples are Stirling, Rankine, and Brayton cycles, which convert the working fluid heat to mechanical energy, which is then converted to AC power.

Since most devices rely on DC power, and moving parts typically reduce system reliability, space reactors will most likely rely on some form of static, direct power conversion technologies. However, static conversion technology is not very mature. TIC have been demonstrated to operate at ~15% efficiency at temperatures of ~1200 K, whereas TPV converters have shown ~20% efficiency at much lower temperatures. In either case the efficiency is heavily dependent on temperature.

For high power applications it is not certain that low efficiency static conversion systems will work, or that the space power system can operate in the required temperature regimes. Therefore, dynamic options such as those listed above must be considered.

The overall objective was to develop a conceptual design of a nuclear space power “package.” The package is the reactor and the PCU. The reactor is a HEU fueled UHPDC similar to the RGP fueled UHPDC designed previously at MIT. The PCU options were compared and a promising technology was selected for application in a package capable of producing at least 400 kWe with the ability to be scaled to the multi-megawatt regime.

The scalability of the different power packages was assessed and a conceptual design established based on the transformational nature of the more promising technologies.

Three power conversion technologies were evaluated and their properties are discussed in this thesis. TPV technology was already employed in a space reactor design conducted at MIT. TIC is similar to TPV in that TIC is also static and direct. Therefore the tradeoffs between TIC and TPV were evaluated to understand the range of applicability for TIC.

Dynamic power conversion approaches were also evaluated. A reference Brayton cycle (argon working fluid) and a reference Rankine cycle (sodium working fluid) were compared. These two cycles in particular were examined because of their scalability. Each of these dynamic cycles offers potential for multi-megawatt power as the temperature and pressure of the cycles are increased.

This thesis will describe the simple argon Brayton cycle, as well as power regimes where the cycle is competitive. The scalability of the cycle is assessed by determining the work that can be attained from the cycle with temperatures of the order of 1200 K. Higher temperatures require research into materials development to assure systems reliability. The cycle temperatures required to attain approximately 3 or 4 MW are also assessed. For the argon Brayton cycle, analysis has shown that temperatures of the order of 2200 K are required to reach the multi-megawatt regime.

The simple sodium Rankine cycle is a more promising alternative in terms of dynamic power conversion. Analysis of this cycle shows very promising results at low temperature and pressure (as much as 1 MW can be achieved in the 1200 K temperature range). The distinctive properties of

sodium allow for easily scaling the power to ~ 3 MW with coolant temperatures on the order of 1500 K at ~ 10 atm of pressure.

The body of this thesis will describe the argon Brayton cycle. The Brayton cycle is the proposed power conversion technology employed for the SAFE 400 program. Secondly TIC are described with respect to novel approaches for implementation. Thirdly, the sodium Rankine cycle is examined. The promising results of the sodium Rankine cycle analysis motivate work on enabling technologies to avert problems with liquid/vapor metal coolants with regards to reactor startup.

Particularly, coolant freezing was identified as a potential concern with regards to reactor startup. The reactor must be launched to achieve a “nuclear safe” orbit before operation can begin. A “nuclear safe” orbit is defined as an orbit where the orbit will not degrade. The reactor should not be operational, thus not producing radioactive fission products, until it is a sufficient distance from the Earth to ensure that the system will not reenter the atmosphere.

In delivering a liquid metal cooled system to this orbit, and assembling the power package with other components, steps must be taken to ensure that the coolant does not freeze before the reactor can be started. The novel approach of radioisotope doping was considered and evaluated to assess the applicability to the sodium Rankine cycle as well as its applicability to other liquid metal cooled systems.

The UHPDC is considered for use with any of these systems. Though in the case for next-generation TIC the core will undergo major design changes, it is worthwhile to examine the reference core. RGP is already radioactive, as higher isotopes of plutonium undergo spontaneous fission, therefore, the reactor fuel poses a safety concern prior to launch.

Analyses conducted at MIT confirm that the radiotoxicity hazard of the UHPDC is comparable to the Cassini Radioisotope Thermoelectric Generator (RTG) powered probe. However, if HEU can be used as an alternative fuel form with little or no penalty in performance and mass, then it is worthwhile to use HEU fuel.

This thesis discusses the design changes made to the UHPDC core with sodium coolant to facilitate operation and control with HEU fuel as opposed to RGP fuel. Along with the design changes, there are details as to the changes made to the ex-core control mechanism. As a result of the design changes, the benefits of using RGP fuel can be assessed numerically in terms of mass, radiotoxicity, and simplicity of reactor control.

1.2 Scope of the Current Work

Based on the aforementioned analyses, the most promising power conversion technology and the adapted HEU UHPDC were combined to form the basis for the SELENE design. The Sodium-cooled Epithermal Long-term Exploration Nuclear Engine (SELENE) is designed specifically to be scalable from low to high power with little or no changes to the system architecture. The low power variants are meant to act as transformational test beds to develop program experience and technology demonstration.

Three variants on the SELENE concept were designed based on thermal hydraulic and physics models for the reactor core. Thermal hydraulic models were used to evaluate the core under accident conditions and coupled with physics codes to determine a variety of nuclear design products and operational parameters for the various systems.

Lastly, the core was analyzed to determine power reactivity feedback coefficients and response to potential launch accidents. Overall, the goals for system scalability and safety are simultaneously met by designing the core with a reactivity-power coefficient of essentially zero.

1.3 Organization of this Thesis

This thesis will first describe in detail the simplified analysis used to compare the competing power conversion technologies in Chapters 2, 3, and 4. Based on the results of the simplified analyses, the sodium Rankine cycle appears very promising. To address the concerns with coolant freezing, radioisotope doping was evaluated and will be discussed in Chapter 5. Chapter 6 discusses the trade-offs between RGP and HEU fuel and discusses the required design changes to use HEU fuel.

The first eight chapters form the basis of the conceptual design of the SELENE system: the sodium Rankine cycle combined with the HEU UHPDC. The conceptual design is summarized in Chapter 7. The remainder of this thesis then describes more specifically the sodium Rankine cycle (Chapter 8) and the models used for thermal hydraulic analysis of the core (Chapter 9). The thermal hydraulics models are then used iteratively with the reactor physics models to evaluate design alternatives. The physics of the reactor core are discussed in detail in Chapter 10. Based on the power profiles and thermal hydraulics model, hot channel analyses were conducted to ensure fuel integrity under steady state operation as shown in Chapter 11.

Chapters 12 and 13 discuss the system response to accidents. The reactivity-power coefficient was calculated and verified to be essentially zero. Potential launch accidents were also evaluated, specifically for the case where the system is immersed in water. Chapter 14 provides a summary of the key aspects of the project, and the Appendices are included in Chapter 16.

2.0 Argon Brayton Cycle

A simple model was developed to explore the applicability of argon gas Brayton cycles for space reactor applications. Simple analyses were conducted to explore the power limitations for the cycle and establish power regimes where the cycle has competitive advantages versus direct energy conversion schemes.

Midrange power reactor applications are of current interest for supporting the Mission to Mars initiative. To support these applications, the current work examines the applicability of a simple argon Brayton cycle for space reactor power conversion. Midrange refers to power levels between 200 kWe to 1 MWe.

Brayton cycles are of particular interest because of the possibility of operating at very high temperature. Cycle heat rejection is limited to radiation losses, and therefore, higher fluid temperatures in the cold leg are preferred to maximize the useful work.

Ultimately, any cycle is limited by the Carnot efficiency, and therefore, cycles that operate at high cold leg temperatures relative to the hot leg will operate at low efficiencies. Cycle analysis, therefore, is aimed at arriving at maximum net work, which is often far from optimum efficiency. Additionally, to ensure lightweight and high system reliability, simple cycles are preferred.

2.1 Methodology

The argon simple Brayton cycle is analyzed based on a list of simplifying assumptions. Firstly, no consideration is currently given to the size or mass of components. In most space reactor applications the radiator and associated armor accounts for a large fraction of the total PCU mass. Secondly, an ideal gas approximation is used to determine the fluid thermodynamic properties.

To give a basis for the heat rejection limitations for the cycle, a radiator surface area of 180 m² is assumed, and the armor emissivity is assumed to be 0.85. The cycle contains both a compressor and a turbine. In Brayton cycles the overall efficiency is fairly sensitive to these component efficiencies; each of these components is assumed to have an efficiency of 0.90.

Further assumptions are made to simplify the thermodynamic analysis, firstly, an ideal gas approximation is used. Secondly, constant specific heat is assumed. Fluid properties ($k = 1.68$ and $c_p = 520.5 \text{ J/kgK}$) are taken at a temperature of 700 K, though the fluid will likely be at temperatures in excess of 1400 K in the hot leg of the cycle. Since this analysis is meant to explore the applicability of the argon Brayton cycle, such simplifying assumptions will yield results that, while not being completely accurate, give an order of magnitude for achievable net work.

Pressure losses are also dealt with approximately using a β -factor approach. In this case β is assumed to be 1.05, though in a compact system with high velocity flows, this is likely to be somewhat higher. The simple Brayton cycle with losses is shown in Figure 1. Reference points are labeled 1-4.

Brayton Cycle Using Constant Specific Heats

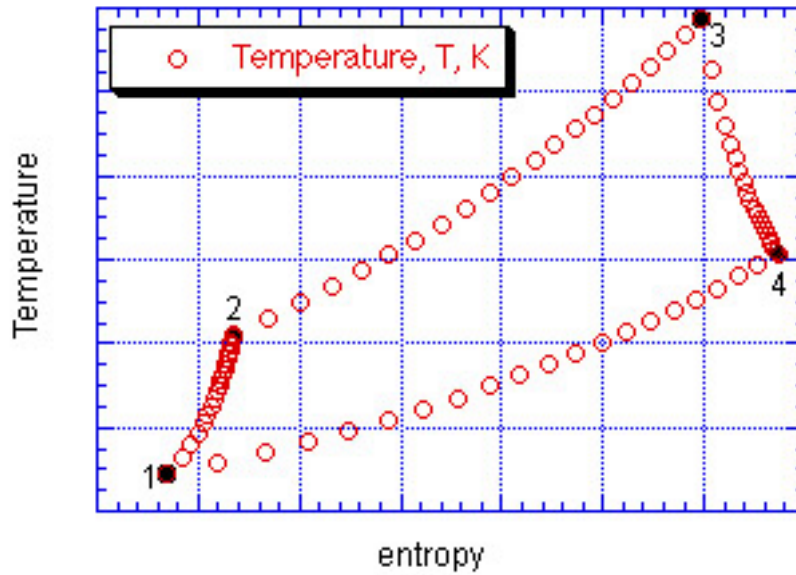


Figure 1: Brayton Cycle Schematic

The pressure losses are accounted for using the following β -factor formulation shown in Equation 1.

$$\beta = \left(\frac{p_4}{p_1} \frac{p_2}{p_3} \right)^{\frac{k-1}{k}} \quad (1)$$

where, k is the ratio of specific heats for the gas, and p is the pressure at a particular state point.

2.2 Theory

Using simple relations, we can derive expressions for the net work from the cycle as a function of the hot and cold temperatures of the cycle. To achieve this, we calculate the cycle efficiency as a function of the temperature. Then, multiply the radiation loss term by a function of the efficiency to determine the net work from the system.

A hot temperature (T_3) is then specified. By differentiating the net work equation, one can find the cold temperature (T_1) where the maximum net work is produced.

Let us first discuss the calculation of the cycle efficiency in terms of the turbine and compressor work per unit mass flow. The turbine and compressor specific work terms are given by Equation 2 for an ideal gas.

$$\frac{W_T}{\dot{m}} = w_T = \eta_T c_p T_3 \left(1 - \frac{1}{\left(\frac{p_3}{p_4} \right)^{\frac{k-1}{k}}} \right) = \eta_T c_p T_3 \left(1 - \frac{\beta}{\left(r_p \right)^{\frac{k-1}{k}}} \right) \quad (2)$$

$$\frac{W_{CP}}{\dot{m}} = w_{CP} = \frac{1}{\eta_{CP}} c_p T_1 \left(\left(\frac{p_2}{p_1} \right)^{\frac{k-1}{k}} - 1 \right) = \frac{1}{\eta_{CP}} c_p T_1 \left(\left(r_p \right)^{\frac{k-1}{k}} - 1 \right)$$

where, c_p is the specific heat of the gas at constant pressure, assumed constant, η is the component efficiency, and r_p is the cycle pressure ratio.

One can likewise define the specific reactor power, or reactor power per unit mass flow, given in Equation 3

$$\frac{Q_{RX}}{\dot{m}} = q_{RX} = c_p (T_3 - T_2) = c_p \left\{ T_3 - T_1 \left[1 + \frac{1}{\eta_{CP}} \left(r_p^{\frac{k-1}{k}} - 1 \right) \right] \right\} \quad (3)$$

The net work is defined as the difference between the turbine and compressor work. The cycle efficiency is the ratio of the net work to the reactor power.

$$W_{NET} = w_T - w_{CP}$$

$$\eta = \frac{W_{NET}}{q_{RX}} \quad (4)$$

The efficiency and the total heat rejection can be used to establish the actual net work and the mass flow rate. The heat rejection is given by a formulation of gray-body radiation shown in Equation 5.

$$Q_{rej} = \sigma \epsilon A T_C^4$$

$$W_{NET} = \left(\frac{\eta}{1 - \eta} \right) Q_{rej} \quad (5)$$

where, T_C is the average temperature of the fluid in the radiator, σ is the Steffan-Boltzmann constant, ϵ is the emissivity, and A is the radiator surface area.

The mass flow rate is the ratio of the net work to the specific net work. The system has not been closed yet. First, the average fluid temperature in the radiator has not been established, and whereas this typically involves integrating over the flow, a simplistic approach to approximating this temperature is shown in Equation 6.

$$T_C \approx \frac{1}{2}(T_4 + T_1) = \frac{1}{2} \left(T_3 \left[1 - \eta_T \left(1 - \frac{\beta}{r_p^{\frac{k-1}{k}}} \right) \right] - T_1 \right) \quad (6)$$

The system has three remaining degrees of freedom, though two of these are the high and low cycle temperatures, the last is the operating pressure ratio. We can determine the optimum pressure ratio by maximizing the specific net work. For an ideal cycle the result is well known and is shown in Equation 7.

$$(r_p)_{opt}^{ideal} = \left(\frac{T_3}{T_1} \right)^{\frac{k}{2(k-1)}} \quad (7)$$

When the component efficiencies and pressure losses are included, the pressure ratio can be determined using the same procedure; the final result is slightly different, as shown in Equation 8.

$$(r_p)_{opt}^{real} = \left(\eta_T \eta_{CP} \beta \frac{T_3}{T_1} \right)^{\frac{k}{2(k-1)}} \quad (8)$$

Though the product of the component efficiencies will reduce the optimum pressure ratio, the inclusion of the pressure loss factor increases the optimum pressure ratio. Together these effects will reduce the optimum pressure ratio slightly. The real treatment is used for the current analysis.

The previous equations can be combined to give the net work as a function of the hot and cold temperatures and the pressure ratio. By using the optimum pressure ratio, one has an equation that gives the net work for a given hot temperature as a function of the cold temperature.

2.3 Results

A computer is used to solve the system of equations numerically. Though one can manipulate the formulas to achieve a single closed form equation eliminating all variables besides the temperature limits and the net work, this approach allows one to simultaneously calculate a host of other parameters of interest.

The approach also allows for quick sensitivity analyses by changing temperatures and other input parameters. Ideally, the cycle should be relatively insensitive to small perturbations in the input parameters. The susceptibility of the net work is of particular interest once temperature limits are established.

Based on the input parameters, such as gas properties and component efficiencies, discussed above, the net work is calculated for hot leg fluid temperatures of 1200 K, 1400K, and 1600 K as a function of the cold leg temperature; the results are shown in Figure 2.

The low (1200 K) hot leg temperature (LTH) cycle is analyzed for comparison purposes. The most promising option here is near the mid (1400 K) hot leg temperature (MTH) cycle. The high (1600 K) hot leg temperature (HTH) cycle is analyzed as a potential option for future application.

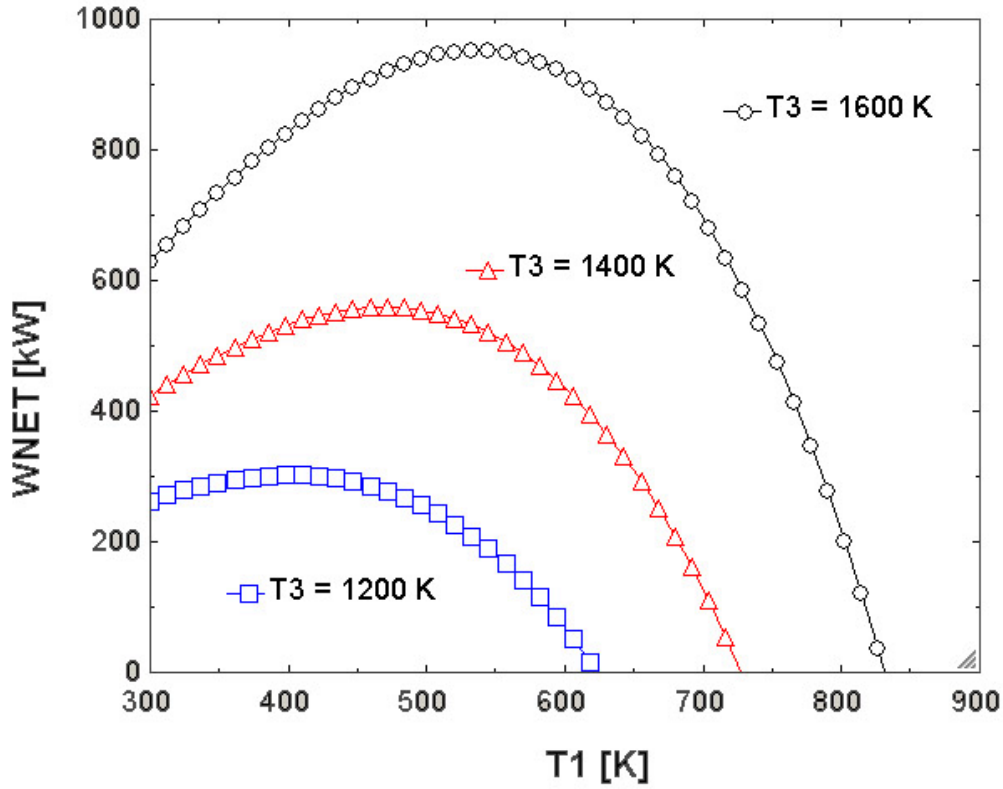


Figure 2: Net useful work as a function of minimum cycle temperature.

The figure clearly summarizes the achievable power for each temperature limit. For the LTH cycle, the maximum useful work is approximately 300 kW; for the MTH cycle, 550 kW; and for the HTH cycle, 950 kW.

The cycle characteristics for each of the proposed temperature limits are summarized in Table I.

Table I: Cycle Characteristics

	LTH	MTH	HTH
T1 (low)	400 K	473 K	533 K
T2	665 K	780 K	890 K
T3 (high)	1200 K	1400 K	1600 K
T4	830 K	970 K	1100 K
Net Work	300 kW	560 kW	950 kW
Thermal Efficiency	0.20	0.19	0.20
Mass Flow Rate	5.5 kg/s	9.1 kg/s	13 kg/s
Reactor Power	1.5 MW	3.0 MW	4.9 MW
Pressure Ratio	3.18	3.13	3.18

A quick sensitivity analysis is conducted on the MTH cycle to determine the susceptibility of the net work to small changes in the assumed parameters.

Table II: Sensitivity Analysis

Parameter	Nominal Value	New Value	Wnet	Susceptibility	
k	1.68	2	559.1	%Δ Wnet / %Δ k	0.00
cp	520.5	550	559.1	%Δ Wnet / %Δ cp	0.00
ηT	0.90	0.85	467.2	%Δ Wnet / %Δ ηT	2.96
ηCP	0.90	0.85	485.6	%Δ Wnet / %Δ ηCP	2.37
β	1.05	1.1	378.7	%Δ Wnet / %Δ β	-6.78
A	180	170	528.0	%Δ Wnet / %Δ A	1.00
T1	473	463	559.0	%Δ Wnet / %Δ T1	0.01

As can be deduced from the sensitivity study, the net work is most susceptible to changes in the component efficiencies and the pressure losses. Though the specifics of the design will dictate the final performance, in any case, it appears that the argon Brayton cycle can produce net work output on the order of several hundred kW.

2.4 Discussion

The results summarized by Figure 2 show a general trend in the net work as a function of the minimum cycle temperature. The curves are initially positively sloped. In the low temperature ranges, the improvement in heat rejection from raising the temperature trumps the loss in efficiency with increasing cold leg temperature.

Above the maximum point, the efficiency is reduced dramatically with increasing temperature, eventually yielding negative work. This decline occurs because the turbine work becomes increasingly small compared to the compressor work.

The formula for the optimum pressure ratio sets a maximum cold leg temperature. The ratio of pressures at the turbine inlet and outlet must be at least unity for there to be any turbine work. Therefore, the range of T_1 is specified in terms of T_3 as shown in Equation 9.

$$T_1 < \frac{\eta_T \eta_{CP}}{\beta} T_3 \quad (9)$$

When this condition is met, there is no turbine work. For the “maximum” temperature, the cycle has negative efficiency because of compressor work.

The results also indicate that increasing the high temperature of the cycle by 200 K approximately doubles the attainable net work from the cycle. This being the case, the argon Brayton cycle offers the potential to produce greater than 1 MW of power at very high temperatures (~ 1700 K). However, more technology development in the area of high temperature materials will be required to deploy such a system.

The LTH and MTH cycles may both be deployed. The LTH cycle will be a demonstration of the Brayton cycle that can eventually be scaled up in power from 300 kW to 550 kW.

For precursory unmanned mars missions PCU requirements are on the order of 200 kWe. This is comfortably achievable with the LTH cycle, at potentially even lower temperatures. For future

mission plans, if the argon Brayton cycle is adopted as the key power conversion option, improvements must be made in materials research such that the cycle temperature can be increased dramatically without loss of structural integrity.

To achieve net work on the order of 3 to 4 MW, the high temperature of the cycle must be greater than 2000 K. With a high temperature of 2200 K, the maximum net work is 3.4 MW with a low cycle temperature of 740 K and 19% thermal efficiency.

Based on the sensitivity analysis, component efficiencies on the order of 90% are required and fractional pressure losses must be kept to a minimum. This motivates the use of a high pressure cycle.

This Page Left Intentionally Blank.

3.0 Thermionic Power Conversion

Thermionics refers to the direct conversion of heat to electric current. Thermionic converters (TIC) work by using a high temperature source to liberate electrons from an emitter, which then preferentially flow towards a cooler collector. Though these devices operate at relatively low efficiencies up to temperatures near 1200 K, the potential to achieve efficiency on the order of 25% seems reasonable at emitter temperatures on the order 2200 K.

Previous analysis of a simple Brayton cycle for potential deployment with space reactors shows that 2200 K is the hot leg temperature required to generate 3 – 4 MW of electric power. Thermionics are compared with the Brayton cycle to establish the limits of useful work. Two scenarios are evaluated. A small power unit using a liquid metal cooled reactor is proposed. The first system will operate with a single layer thermionic power conversion system. A second, larger power unit is proposed, though without giving thought to the coolant, as thermionics can be utilized with direct contact with the fuel cladding. The second system makes use of dual layer thermionic converters where the collector of the first layer heats the emitter of the second layer.

The first system will operate between temperatures of 1200 K and 750 K. For these temperature ranges, lead efficiencies of 12.4% or higher have been demonstrated experimentally using closed space cesium converters [Fitzpatrick, et al.]. For higher emitter temperatures (2200 K) barium-cesium converters have been demonstrated to operate in excess of 12% efficiency at a collector temperature on the order of 1200 K. The second scheme layers the converters so that the barium-cesium collector acts as the heat source for the emitter for a closed space cesium converter.

In either case the heat rejection for a given radiator surface area will be the same. Therefore, the useful work of the dual layer system will be approximately 2.5 times the useful work from the single layer system. Since two designs are being proposed, they will be discussed separately, extrapolating the results from the single layer design to a dual layer design.

3.1 Single Layer Design

The single layer design uses a liquid metal cooled fast reactor to act as a heat source for a thermionic emitter. The hot coolant at the reactor outlet will flow through an inner annulus near the periphery of a cylindrical power package.

The power package is the combined reactor, radiator, piping, and shielding. The power package is armored with a high emissivity material that duals as a radiator. The reactor is located in the center of the cylindrical package. The collector of the thermionic conversion is located along the inner wall of the radiator. Figure 3 shows a simple schematic of the power package.

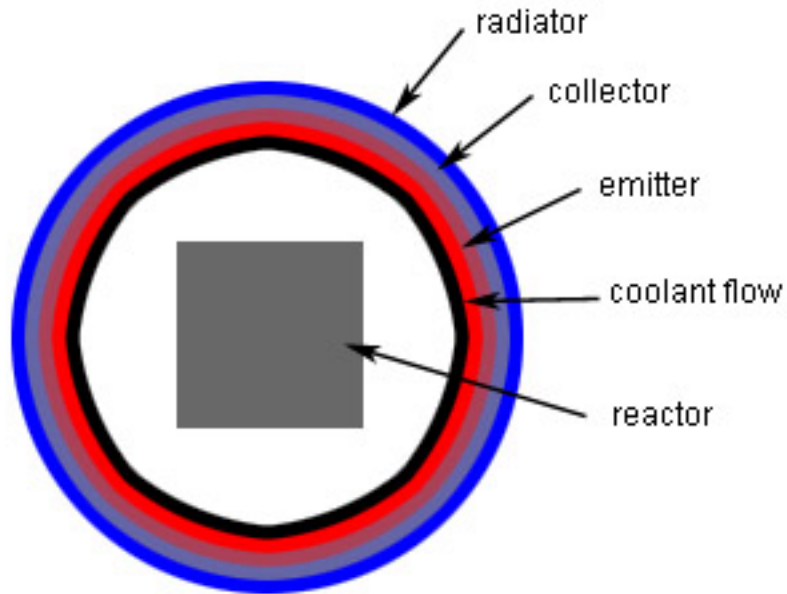


Figure 3: Diagram of the Single Layer Thermionic Conversion Power Package.

At atmospheric pressure, lithium has a boiling temperature of 1600 K. Since lithium has been proposed as an alternative coolant for the MSFR in previous work done at MIT, it is a reference coolant for this design. As an initial reference, closed space cesium converters are selected because they operate in the collector temperature range of interest.

The coolant temperature varies between 1200 K and 1300 K. The temperature range is selected firstly to be compatible with the converters, but secondly such that the difference between the coolant temperature at the core outlet and the boiling temperature of the coolant is $\sim 3 \Delta T_{\text{core}}$.

Thermoelectric-Electromagnetic (TEM) pumps are the reference liquid metal pumps for the power package. They are self regulating and self powered; these type of pumps have been tested for high temperature lithium (1400 K) and were suggested for the MIT space reactor design (MSFR) [Dostal, et al.].

Assuming negligible losses to pumping power, we can use the lead efficiency as the conversion efficiency. The assumption is reasonable because increasing the coolant temperature slightly will not compromise the relatively large margin, and the pumps operate directly from the heat in the molten metal flow. Therefore, increasing the temperature at the outlet will compensate for pumping losses.

We can calculate the radiated heat based on the assumed radiator surface area, which is the same as proposed for the argon Brayton cycle (180 m²). The emissivity is assumed at 0.85 and the radiator temperature is assumed to be the same as the collector temperature (750 K). The radiated heat is given by Equation 10.

$$Q_{rad} = \sigma \epsilon A T^4 \quad (10)$$

where σ is the Steffan-Boltzmann constant,
 ϵ is the radiator emissivity,
 A is the radiator area, and
 T is the radiator temperature.

Since we have assumed that pumping power can be easily compensated for, it is neglected in the current analysis, and the conversion efficiency is given by the lead efficiency. For closed space cesium converters operating between 1200 K and 750 K the demonstrated efficiency is 12.4%.

The radiated heat is calculated to be 2.7 MW. The net work available from the converter is given in Equation 11, with the efficiency given as 12.4%. In this scenario the net work is the electrical power generated by the flow of electrons from the emitter to collector.

$$W_{net} \approx W_{out} = \frac{\eta_L}{1 - \eta_L} Q_{rad} = 0.382 MW \quad (11)$$

where W is the work, either net or turbine, and
 η_L is the thermionic lead efficiency.

The thermionics look particularly attractive for the mid-range power applications. The single layer thermionic converter appears to be able to produce nearly 400 kWe of useful work with no need for moving parts or AC to DC conversion.

The thermionic converter has a given maximum thermal power density of 2.2 W/sq-cm [Fitzpatrick, et al.]. To ensure that this limit is not breached we assume a converter area approximately equal to the radiator area and then add the radiated heat to the net work and assume that is the thermal power. The resultant density is approximately 1.7 W/sq-cm. Though this is below the limit, the margin is questionable given the simplifying assumptions.

3.2 Dual Layer Design

The dual layered thermionic conversion system will look very different from the current system, though many aspects will remain the same. The dual layered approach “stacks” one thermionic material on another such that the high temperature collector heats the low temperature emitter of the second layer.

Barium-cesium converters operate a very high temperatures, yielding lead efficiencies of 12% - 15% with emitter temperatures of 2200 K and collector temperatures on the order of 1200 K. The high temperatures require novel approaches for heat removal from the reactor. Though this temperature was proposed for a high power argon cycle application, the need for ultra-high temperature materials may preclude the use of either scheme in the near future.

However, the high temperature collector of the barium-cesium can be near direct contact with the fuel inside the core. In that case, the fuel will exceed temperatures of 2200 K, however most ceramic fuel forms, UC in particular, have melting temperatures greater than 2600 K.

Pu-UC is the reference fuel form from the MSFR design, however, fuels with less egregious swelling properties are preferred in this application, so US and UN are proposed as alternatives.

The fuel heats the high temperature emitter directly; the rejected heat from the collector then heats the emitter for a low temperature layered converter. In this scenario, effective lead efficiencies of 25% are achievable, approximately double the efficiency in the single layered design.

Though the core and structures will be very different between the two designs, the radiator surface area limit still applies. Fuel elements will need to be designed to ensure that thermal power density limits of the barium-cesium and closed space cesium converters are not exceeded, additionally, fuel elements should be smaller to keep the fuel centerline temperature below the melting point with some margin.

A liquid metal coolant, most likely, will be used to cool the collector of the closed-space cesium converter. The coolant will then flow through a radiator. Ideally, the liquid metal will be near the liquid / vapor transition so that heat may be radiated with a near constant temperature.

Mercury, with a boiling temperature of 630 K at atmospheric pressure, should be considered as a heat rejection media. The liquid mercury coolant can enter the reactor core near the saturation temperature, remove heat from the collectors at near constant temperature, and then radiate the heat through a standard radiator similar to the one described for the single layered design. However, to maintain collector temperatures near 750 K, the mercury coolant will most likely be pressurized.

If we are limited to the same radiator area and temperature, the radiated heat will be the same, however, since the efficiency has at least doubled, the useful power increases from 400 kWe to 900 kWe.

3.3 Direct Contact Single Layer

Since the work output is intimately related to the radiated heat, and the radiated heat is heavily dependent on the temperature of the heat rejection, a single layer, direct contact TIC may also prove useful. To this end, we analyze a single barium-cesium converter in direct contact with the fuel cladding. In doing so, if a coolant with a phase transition near 1200 K (sodium near atmospheric pressure) could be used, then the effective temperature of the heat rejection would be 1200 K. The heat rejected becomes 18 MW. The efficiency drops to ~12 – 15%. If we assume 15% lead efficiency and neglect pumping losses, the net cycle work can be approximated by Equation 12.

$$W_{net} \approx W_{out} = \frac{\eta_L}{1 - \eta_L} Q_{rad} = \frac{0.15}{0.85} (18MW) \approx 3MW \quad (12)$$

If a lead efficiency of 12% is assumed, the work output drops from roughly 3 MW to 2.5 MW. This indicates that the direct contact, single layered concept can yield multi-megawatt work.

The core must be redesigned to fit these specifications. A honeycomb fuel design may prove impossible to couple with this concept. Therefore, the core will most likely be an array of plates with the cladding of each plate coated with TIC. The collectors of the TIC layers form the channel walls for coolant flow. Figure 4 illustrates a conceptual unit cell for the single layer core fuel plate.

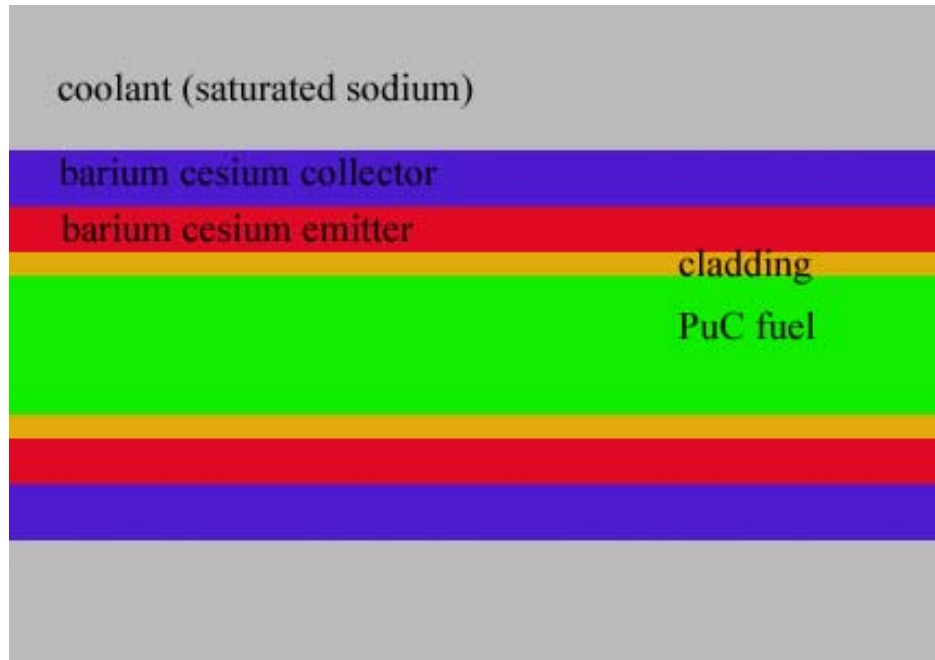


Figure 4: Conceptual Fuel Plate for Single Layer, Direct Contact TIC

The collector of the barium-cesium TIC will most likely require some cladding. Ideally this cladding will have good thermal conductivity to maintain the collector temperature at 1200 K and the TIC cladding may require two layers, each being good thermal conductors, while only one is a good electrical conductor. SiC for instance, may prove a necessary coating material for the TIC / Coolant interface cladding.

3.4 Comparisons

Fuel swelling will be a concern when it comes to the integrity of the thermionic converters, so work must be done to evaluate potential fuel materials and cladding candidates if thermionic conversion is to be pursued for higher power applications.

Compared with the Brayton cycle, the work output is higher for a comparable coolant temperature, however, there are concerns about the direct contact with the fuel, and the required fuel operating conditions. There is also a concern about the TIC efficiency after irradiation. The heat flux limit on the TIC materials means, particularly for a UHPDC, the TIC will be distributed through the core, in most likely a plate or pin configuration. The materials are therefore exposed to a hard neutron flux.

Additionally, some attention must be paid to the temperature profile in the radiator and along the collector of the TIC. In core, the power profile is relatively flat, and the TIC emitter will most likely have a relatively flat temperature profile axially. The collector of the TIC at the core outlet may have an increased temperature that inhibits its operation.

3.5 Conclusions

In the mid-range power applications thermionics are competitive with Brayton cycles. The thermionic conversion schemes have the benefit of no moving parts and direct energy conversion. Whereas coolant freezing may pose a concern for a liquid metal cooled or liquid/vapor metal cooled reactor, Brayton cycle startup for the power package may prove to be a complicated procedure.

In the mid-power range, either system is limited by the temperature of materials. At gas temperatures of 2200 K, the argon Brayton cycle appears capable of producing useful work in the multi-megawatt range. However, little consideration was given to the heat removal aspects of high temperature gas coolant in the MIT UHPDC concept. The thermionic dual layered concept, while requiring similar fuel temperatures, does not appear to pose an insurmountable core design problem.

The single layered, direct contact, high temperature scheme, though less efficient than the dual layered concept appears to be able to produce power in the multi-megawatt range. This is an initially unexpected phenomenon. If the heat rejection temperature is roughly isothermal throughout the radiator, as may be the case for a coolant at saturation, then this concept seems very promising. Sodium may be employed as a potential coolant in this case, Sodium has a saturation temperature of nearly 1200 K at approximately 1.05 atm.

4.0 Simplified Sodium Rankine Cycle

Sodium Rankine cycles are proposed for advanced space power applications. Particularly, sodium is useful because of the high boiling temperature at low system pressure, its neutronic inertness, and its heat removal properties.

For midrange power applications (several hundred kilowatts), it is advantageous to utilize the phase transition temperature in the radiator. When rejecting heat at a constant temperature, one makes the most effective use of the radiator area. Metals, historically, have been proposed for Rankine cycles for power conversion units in space applications. Both sodium-potassium eutectic (NKE) and mercury cycles have been proposed as early as 1950 [Deickamp].

This analysis is meant to form a basis for comparison with Brayton and thermionic power conversion options and establish the limiting amount useful work based on simple assumptions about the space power package.

4.1 Simple Rankine Cycle Specifications

The upper pressure limit is set such that sodium bulk boiling will occur near 1100 K. This pressure is slightly greater than atmospheric pressure. The lower pressure in the cycle will be established by the analysis, particularly given a limit to the turbine exit quality.

The turbine is assumed to have a component efficiency of 0.85 and the pumps are not explicitly treated in the analysis of the efficiency. For sodium, TEM pumps or a similar variation may be employed that will draw heat directly from the flow. At the current stage, no consideration is given to the exact design of these components.

Heat is rejected via a radiator with a high emissivity coating (0.85) and a surface area of 180 m². The temperature of the surface at steady state is assumed to be approximately equal to the saturation temperature of the sodium coolant at the low pressure end of the cycle.

Calculations will be performed for an ideal turbine, then the effect of real components will be assessed by varying the turbine efficiency between 0.95 and 0.80. Though 0.85 is the assumed efficiency for the design, the susceptibility of the design reference to this parameter is of key interest.

4.2 Ideal Analysis

Sodium saturation properties are plotted in Figure 5. The range of interest is the temperature range below 2100 R (1167 K). Some simplifications are made in the calculation of the net work. Firstly, we assume that only a small fraction of the net work is used for pumping, therefore, the reactor inlet enthalpy is assumed to be the same as the radiator exit enthalpy. Calculations of the pumping power will be used to justify this assumption, though for liquid metals pumping power tends to be small.

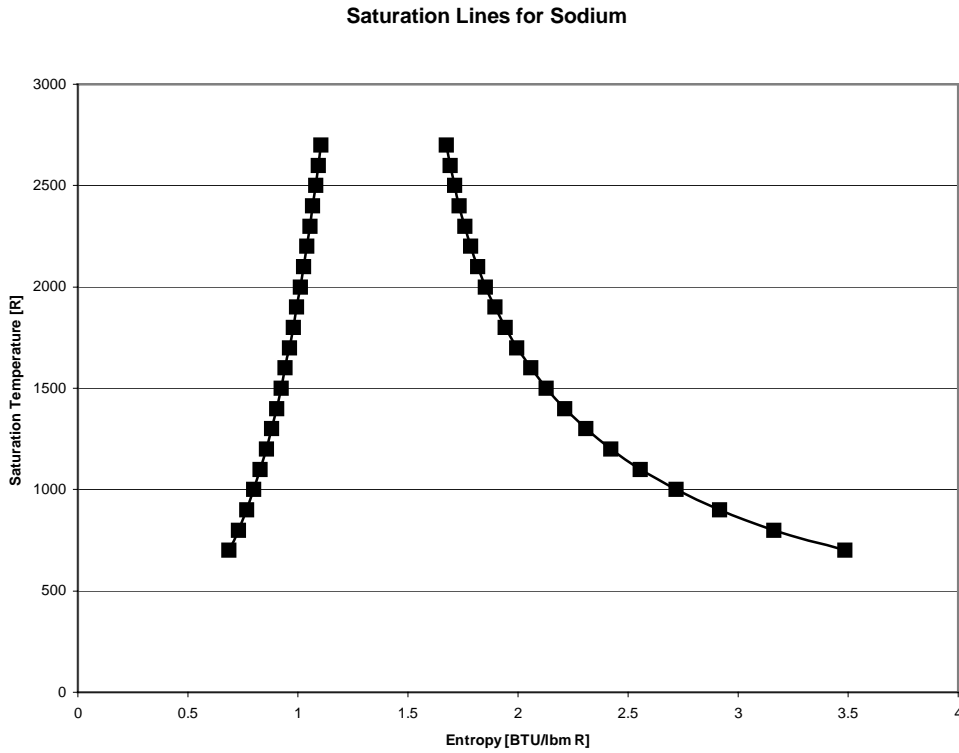


Figure 5: Sodium Saturation Properties

As an initial design iteration, the components are assumed to be ideal, in other words, the entropy of the coolant does not change when pressurized in the pump or expanded in the compressor. A real analysis will be done to show the sensitivity of the cycle to the efficiency of components.

Without details of vapor metal turbine design being accounted for, we set a limit to the exit quality of the turbine at $\sim 80\%$. However, this refers only to a design space, ideally the turbine exit quality will be in excess of 90% .

To calculate the heat rejected, one assumes a fixed radiator area of 180 m^2 , and that the surface temperature is the same as the coolant saturation temperature at the low pressure of the cycle. The heat is then rejected at a constant temperature at steady state. By making use of the phase transition in the radiator, one makes the fullest use of the area of the radiator.

The heat rejected is therefore a function of the low pressure of the cycle, and likewise the exit enthalpy of the turbine. The limit on the exit enthalpy sets a limit for the minimum pressure and likewise on the saturation temperature. Equation 13 gives the heat rejected from the cycle (assuming an effective heat sink temperature of 0 K).

$$Q_{rej} = \sigma \epsilon A (T_{LP}^{SAT})^4 \quad (13)$$

where σ is the Steffan-Boltzmann constant,
 ϵ is the radiator emissivity,
 A is the radiator area, and
 T is temperature.

Here the LP denotes the low pressure of the cycle, and SAT denotes saturation.

Figure 6 shows a plot of the turbine exit quality for a turbine inlet pressure of 15 psia as a function of the turbine outlet pressure.

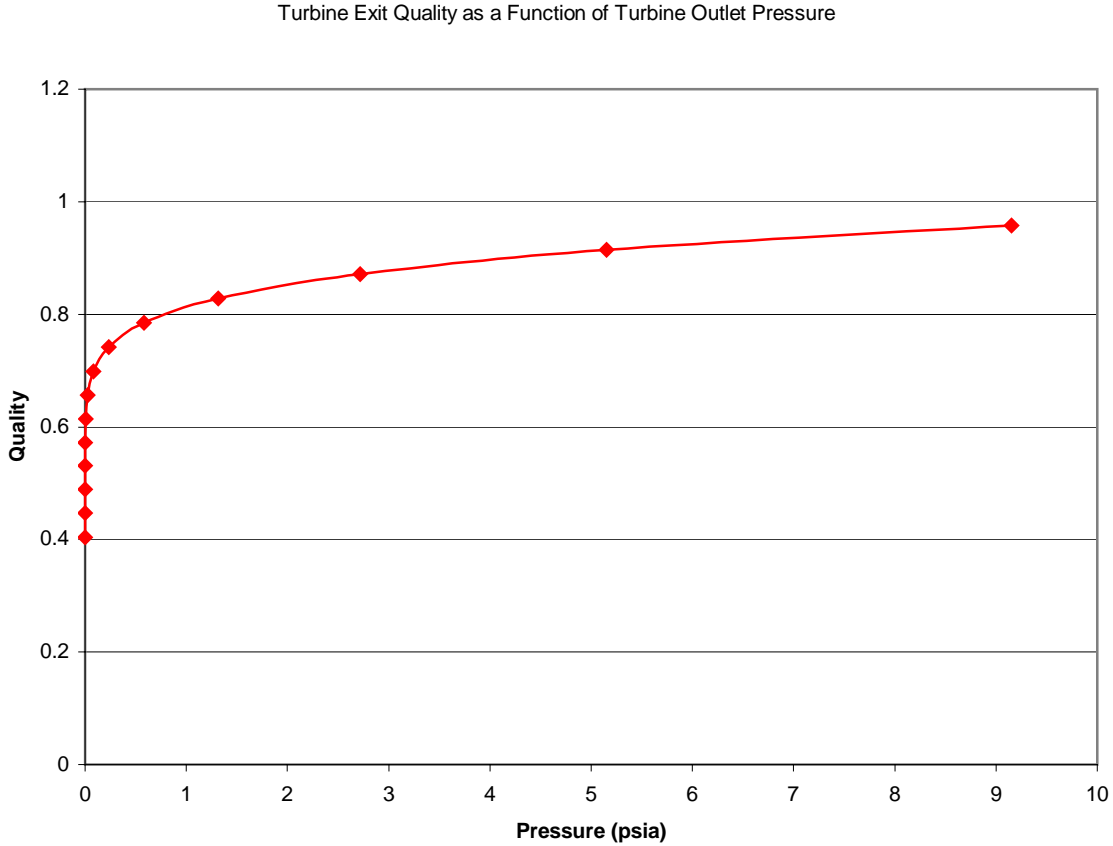


Figure 6: Exit Quality vs. Outlet Pressure.

By demanding exit qualities in excess of 80%, the design space is immediately limited to pressure in excess of 1 psia. If we further limit the exit quality to 90%, the design space is limited to turbine outlet pressures of 5 psia or greater. For the purposes of further analysis, the design space of short term interest will be for turbine outlet pressures on the order of 5 psia or slightly lower (depending on turbine efficiency).

The ratio of the turbine work to the reactor power is also calculated; for low pumping power this ratio is approximately equal to the cycle efficiency. This ratio can be directly calculated from the saturation properties of the sodium at the inlet and outlet pressures. The turbine work is then calculated given the heat rejected from the cycle.

Given the enthalpy drop across the turbine, and the turbine work, the mass flow rate can be calculated. The required pumping power, neglecting any losses, can then be calculated as the product of the volumetric flow rate and the pressure rise through the pump. The pressure rise is assumed to be approximately equal to the pressure drop across the turbine (neglecting losses). Subtracting the pumping power from the turbine work yields the net work. Figure 7 shows the net work as a

function of the outlet pressure, over a range from 1 psia to 15 psia (roughly turbine outlet qualities > 80%).

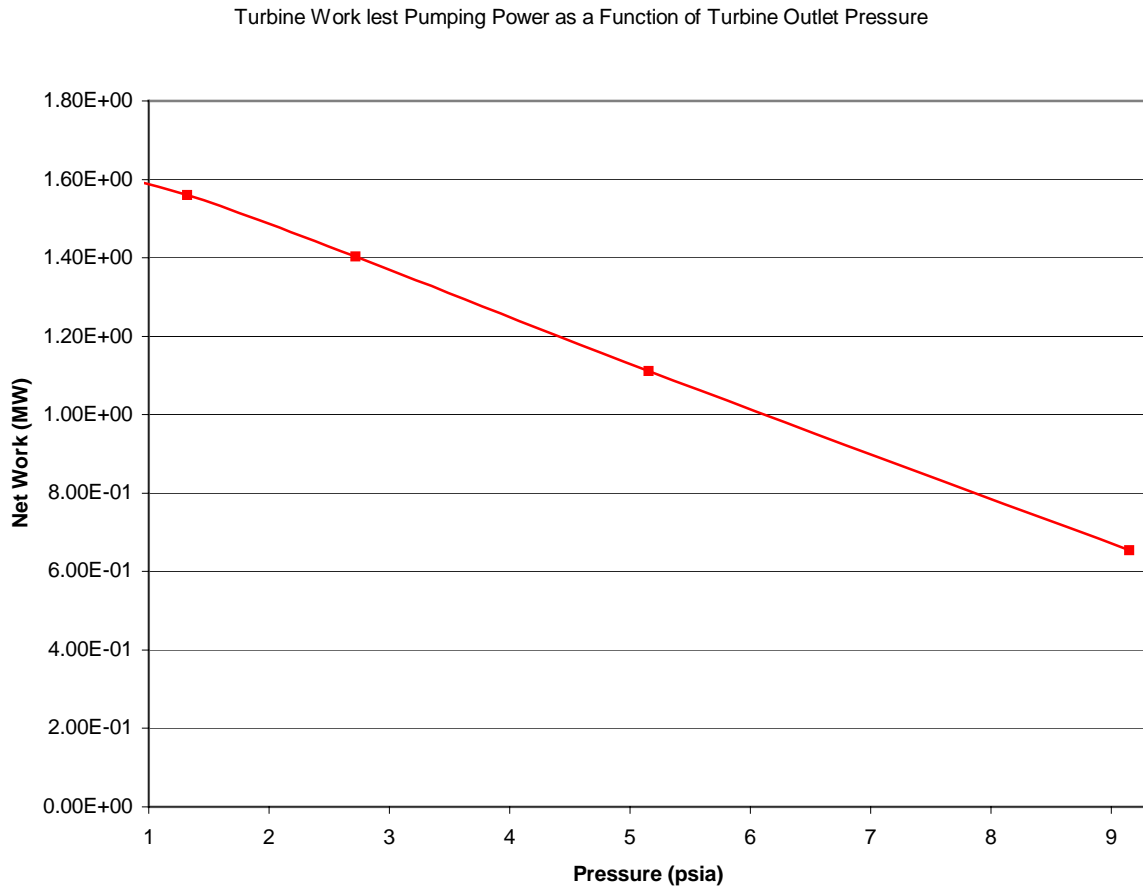


Figure 7: Net Work vs. Outlet Pressure

The net work decreases linearly with the pressure, which is expected. The exit quality is not very sensitive to outlet pressure for high pressures, however, the turbine work is incredibly sensitive; therefore, we define the minimum pressure acceptable given a limit by the turbo-machinery. Therefore, two potential cycles are proposed: a dry and a wet cycle. The dry cycle exit quality is taken at ~ 91% and the wet cycle exit quality is taken at ~ 78%.

For this scenario (the dry cycle) the cycle has a relatively small efficiency of only 9%, the net work is 1.1 MW, the turbine outlet pressure is 5.15 psia and the pumping power accounts for only 200 W (0.02% of the turbine work). The pumping power is calculated as the product of the saturated liquid specific volume, the pressure rise, and the mass flow rate. The radiator rejects approximately 10 MW of heat at a temperature of 1055 K. The core power is therefore approximately 11 – 12 MWth.

If the limit of the exit quality is relaxed to slightly lower than 80%, the wet cycle may be employed. The efficiency of the wet cycle is approximately 22%, and the net work is 1.6 MW. The radiator rejects 5.4 MW of heat at 890 K and the reactor power is reduced to 7 MWth. In the real analysis, accounting for turbine efficiencies, the exit quality will be higher than calculated for the ideal turbine.

Therefore, the limits given by the wet cycle establish an expected range of values for the work attainable from the real cycle.

The saturated vapor line on the T-s diagram is relatively steeply sloping, so given a limit on the turbine exit quality, increasing the system pressure can give an increase in the work. If the system temperature can be increased above the artificially imposed limit of 1167 K the attainable work can be increased with little concern to the turbine exit quality limit.

4.3 Real Analysis

Turbine efficiencies between 0.85 and 0.95 were tested. Comparisons were carried out on the basis of constant turbine exit quality. A limit of turbine exit quality of 0.90 was assumed. The pumping power for the sodium is neglected. The efficiency and turbine work are smoothly varying with quality; therefore, the turbine work and efficiency are calculated based on a linear interpolation on exit quality.

Table III summarizes a performance map for the turbine efficiency. In each case the upper temperature limit of 1167 K is assumed.

Table III: Performance Map

Turbine Efficiency	0.95	0.90	0.85
Cycle Efficiency	11%	11%	11%
Turbine Work [MW]	1.18 MW	1.15 MW	1.14 MW
Turbine Outlet Pressure [psia]	4.0	3.7	3.2

In each case, the turbine work varies between 1.14 and 1.18 MW. The calculation shows that the cycle output is not strongly dependent on the turbine efficiency; however, the turbine outlet pressure is more sensitive to the turbine efficiency and varies between 4 and 3 psia.

In all cases for 1 MW of power, the reactor power is approximately 10 MWth. This is inside the design envelope of the MIT UHPDC.

4.4 High Temperature Cycle

If we allow the cycle to go to higher temperatures, and thus higher pressures, one can harness more net work from the cycle. The sodium Rankine system is highly scalable because of the vapor saturation line, therefore, higher turbine inlet temperatures can be used with greater pressure drops and still maintain the turbine exit quality above 0.90.

A simple case is taken with the turbine inlet temperature equal to 1500 K (saturated) and the turbine efficiency is 0.90. If one expands from 150 psia (~10 atm) to 56 psia (~4 atm) in the turbine, the saturation temperature of sodium at the turbine outlet is approximately 1300 K. The exit quality in this case is 89.7%. The turbine work is 3.4 MW.

The high temperature cycle efficiency is 12.8%. This is better than the TIC single layer, direct contact scheme. The temperature of heat rejection is higher, and the efficiency is comparable.

4.5 Discussion

Additional problems must be addressed before applying the sodium-cooled reactor. Sodium has a violent exothermic reaction with water; therefore special attention must be paid to H₂O immersion accidents. Previous work at MIT showed that H₂O immersion for the UHPDC had a positive reactivity effect, and coupled with the potential for a sodium-water chemical reaction, this accident may have implications that preclude the use of this cycle.

If the power package and armor are designed to mitigate this particular accident, then the sodium Rankine cycle appears at least on par with the argon Brayton cycle. Though the two seem to be competitive at relatively low temperature (1200 K), the liquid metal coolant more easily facilitates the use of a UHPDC type reactor, because of the superior heat removal properties of the liquid / vapor metal.

In the higher temperature regime (1500 K), the sodium cycle outperforms the high temperature TIC concept. However, this marginal benefit may not outweigh the TIC advantage in terms of system reliability. The TIC concept requires neither moving parts nor AC to DC power conversion.

5.0 Radioisotope Doping to Prevent Coolant Freezing

One of the transformational technologies identified for space nuclear power conversion is a liquid/vapor metal Rankine cycle. A potential difficulty with deployment of such a technology is the startup of the reactor where the coolant may be frozen. To this end, a potential approach for averting coolant freezing is explored. A proposed solution to this problem is radioisotope doping, whereby the liquid metal coolant is mixed with radioactive isotopes to concentrations on the order of a few percent. The heat released by the decay of these isotopes may be sufficient to ensure the coolant does not freeze for a given time in space.

Specific examples are explored using simple analyses to determine if such a preventive measure is practical. Two types of metal coolants are examined, first lead or lead-bismuth eutectic (LBE) and secondly sodium or sodium-potassium eutectic (NKE).

5.1 Radioisotopes

For internal heating from radioactive decay, either β^+ or α emitters are preferred. These two decay products will deposit most of their energy directly in the coolant. The isotopes that decay by means of β^+ emission may be less effective than α emitters; however, in metal coolants the electron density is relatively high and an effective fraction may still be deposited. Furthermore, α emitters typically release more energy per decay than β^+ emitters and have longer half lives.

For lead cooled reactors, polonium 210 (^{210}Po) is of particular interest for three reasons. First, it has relatively long half life (139 days). Second it emits a high energy α (5.3 MeV), and third, the decay product is ^{206}Pb [Parrington, et al.].

Several isotopes of bismuth decay through β^+ emission. Bismuth isotopes may be of particular use in doping lead or LBE coolant. ^{206}Bi and ^{205}Bi are both of interest. Each emits positrons with 0.98 MeV of energy. The half lives are 6.243 days and 15.31 days, respectively [Parrington, et al.].

For sodium-cooled reactors, magnesium 23 (^{23}Mg) is of interest. This isotope of magnesium β^+ decays to ^{23}Na with a half life of 11.3 seconds. The β^+ energy is 3.1MeV [Parrington, et al.].

5.2 Analysis

To evaluate the effectiveness of a particular isotope, a heat balance is established where the radioisotope heating exactly balances radiation losses when the coolant is at the melting temperature. From this relationship, the break-even concentration of the doping radioisotope can be established..

The initial concentration of the radioisotope can then be inferred as a function of the time to freezing. In other words, if a time window is set, then the initial concentration of the radioisotope can be calculated.

The radiation losses are calculated the same as before assuming that the temperature of the radiator is the melting temperature at atmospheric pressure for either coolant, and a given radiator size of 180 m². This condition is true at the onset of freezing. Atmospheric melting temperatures are used because liquid metal cooled systems tend to operate at pressures near atmospheric.

$$Q_{loss} = \sigma \varepsilon A (T_m)^4 \quad (14)$$

where σ is Steffan-Boltzmann constant,
 ε is the radiator emissivity,
 A is the radiator area, and
 T_m is the melting temperature.

The heat added by the decay of the radioisotope can be calculated based on the particle energy, the decay constant, the number density, and the coolant volume in Equation 15.

$$Q_{decay} = E \lambda N V \quad (15)$$

where E is the particle energy,
 λ is the decay constant,
 N is the number density, and
 V is the coolant volume.

At breakeven these two quantities are the same. The number density of the radioisotope at breakeven is easily calculated in Equation 16.

$$N = \frac{\sigma \varepsilon A (T_m)^4}{E V \lambda} \quad (16)$$

However, the doping fraction, which is the ratio of the number density of the radioisotope to the number density of the nominal coolant, is the quantity of interest (given in Equation 17).

$$f = \frac{N}{N^{cool}} = \frac{\sigma \varepsilon A (T_m)^4}{E V \lambda} \frac{M}{\rho N_{av}} = \left(\frac{\sigma \varepsilon A}{V N_{av}} \right) \frac{M (T_m)^4}{\lambda \rho E} \quad (17)$$

where ρ is the density,
 M is the atomic mass, and
 N_{av} is Avagadro's number

The volume of the coolant is not yet known. The radiator dimensions may be specified. The radiator is a cylinder encapsulating the reactor and BOP. One can establish an upper bound of the break-even doping fraction by assuming that the coolant volume is as much as 50% of the volume bound by the surface of the cylindrical radiator, as shown in Equation 18.

$$f = \left(\frac{\sigma \varepsilon A}{V N_{av}} \right) \frac{M (T_m)^4}{\lambda \rho E} = \left(\frac{4 \sigma \varepsilon}{R N_{av}} \right) \frac{M (T_m)^4}{\lambda \rho E} \quad (18)$$

where R is the radiator radius.

We will assume that the radiator radius is 3 m. The parenthetical term in the expression is constant, and the second term contains all of the coolant properties. The first term is calculated to be $0.107 \times 10^{-30} \text{ W/m}^3/\text{K}^4$. If the doping fraction is higher than the limit specified in the equation above, then coolant freezing will not occur.

The time to the onset of freezing and the initial doping concentration are related by the breakeven limit and the radioisotope decay constant, shown in Equation 19.

$$t = \frac{1}{\lambda} \ln\left(\frac{f_0}{f}\right) \quad (19)$$

where t is the time window to freezing,
 f is the breakeven doping fraction
 f_0 is the doping fraction at the time of launch

5.3 Calculations

Table IV includes the properties for lead and sodium (and associated radioisotopes). The LBE and SPE coolants are options where the results are roughly applicable. However, the doping fraction is highly sensitive to the melting temperature, so calculations are meant only to indicate a proof of principle.

Table IV: *Doped Coolant Properties [Parrington, et al.]*

	Lead	LBE	Sodium
Density (g/cc)	11.35	11	0.971
Atomic Mass (amu)	207.2	208	23
T_{melt} (K)	600	400	370
	²¹⁰Po	²⁰⁶Bi	²³Mg
Half Life (sec)	12009600	539395.2	11.35
Decay Constant (sec⁻¹)	5.77161E-08	1.28505E-06	0.061070236
Energy (pJ)	0.848	0.157	0.496

The limiting doping fraction can be calculated based on these properties. For the lead coolant, the doping fraction limit was calculated to be 5.16; since the fraction is greater than unity this system does not appear feasible. Even if LBE is considered, the melting temperature drops from 600 to 400 K with a doping fraction of 1.02. This consideration is still not feasible.

Sodium appears more promising; however, the margin to freezing will never be large because the half-life of ²³Mg is quite small. The limiting doping fraction of the coolant is 1.56×10^{-6} . If the initial doping fraction is twice the break-even limit, the system can remain in space for only 11.32 seconds before the onset of freezing. If we limit the initial doping to 10%, the margin to freezing can be calculated. The concentration ratio is approximately $(1/2)^{22}$. Therefore, the margin we purchase through doping is only 4 minutes, roughly. This time is so small that the radioisotope will have completely decayed before the system is launched from Earth.

LBE with radioactive Bismuth is considered as well. This is a prime candidate for the radioisotope doping approach. The ²⁰⁶Bi positron decay has a half life of 6.243 days and decays to ²⁰⁶Pb. The limiting break-even doping fraction is approximately 25%. If an initial concentration of 50% ²⁰⁶Bi is assumed, the melting temperature of the LBE is approximately 400 K. The system can remain in space for a few days before the onset of freezing, although the exact margin is not known because the melting temperature is sensitive to the bismuth fraction. If we assume that a 25% bismuth / 75% lead eutectic has the same melting temperature as a 50% bismuth / 50% lead eutectic, then the system can remain in space for as long as 6 days before the onset of freezing. However, the melting

temperature will probably increase as the bismuth decays, thus reducing the temporal freezing margin.

5.4 Conclusions

Though applicable in some cases, radioisotope doping does not appear to be a feasible solution to liquid metal freezing in many cases. The largest barrier is the relatively large doping fractions required to sustain the system above the melting temperature for a period of time on the order of a few days.

There are other concerns with this approach that will limit its use. Firstly, it is difficult to acquire large quantities of these radioisotopes. The coolant would be incredibly expensive, and it is not certain that the materials can be acquired in any large amounts. Another concern is launching the radioactive material. Though RTGs are routinely launched, RTGs and this approach differ in that the radioactive doping agent in the coolant is distributed through the entire reactor coolant system. The distributed nature of the radioactive material may be of concern for anticipated launch accidents, especially since it is in liquid form rather than in an inert, high melting point compound as in RTGs.

Though radioisotope doping may appear as a feasible solution in some cases, there are a plethora of practical concerns that preclude its use. Radioisotope coolant doping was found only to be even potentially applicable in the case of LBE cooled reactors. Since sodium is of primary concern based on performance of the sodium Rankine cycle, further study of radioisotope doping is not recommended, as it does not appear to be a feasible approach for averting sodium freezing.

6.0 HEU Fueled Ultra High Power Density Core

The Reactor Grade Plutonium (RGP) Ultra High Power Density Core (UHPDC) was redesigned for use with Highly Enriched Uranium (HEU) fuel. The fuel form is UC in plates. The plates are clad with niobium refractory metal. Several design changes were made to improve performance for the HEU system and reduce the reactor mass.

After making substitutions for materials in the core, the core size was evaluated to assess the minimum core size necessary to meet comparable performance standards set by the RGP UHPDC. Afterwards, the same control mechanism (direct leakage) for the RGP UHPDC was evaluated for the HEU UHPDC. Lastly, void reactivity worth was evaluated to ensure that in the case of an accident the control mechanism could still shut down the reactor.

Figure 8 shows a layout of the UHPDC with honeycomb plate type fuel.

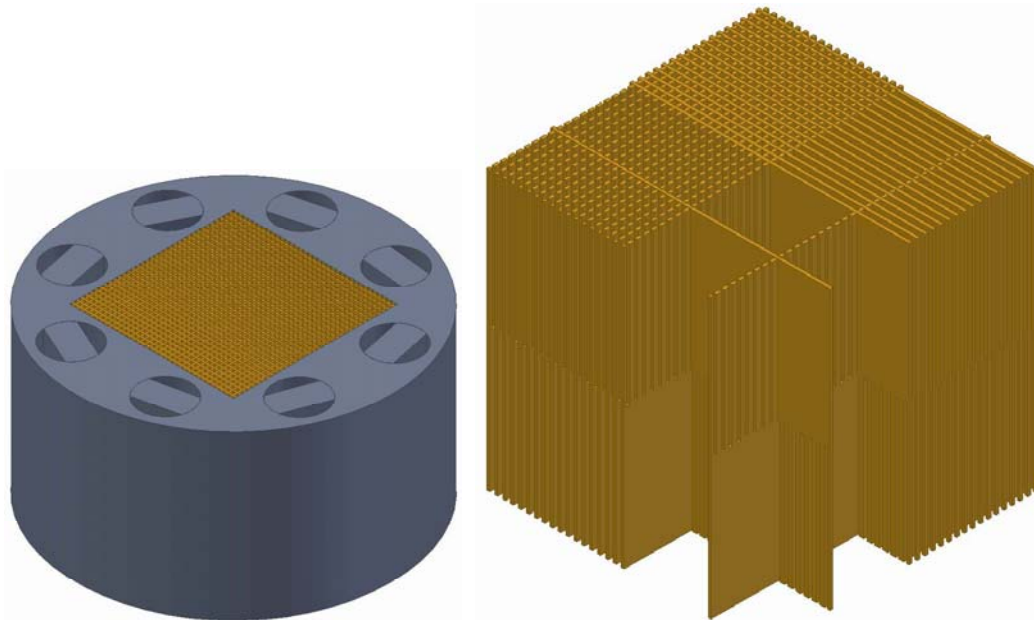


Figure 8: UHPDC layout

6.1 Design Changes

The reference UHPDC used lithium or molten salt coolant. The redesigned HEU core uses sodium coolant. This is to more accurately reflect the neutronic behavior of the system when coupled directly with the sodium Rankine cycle, sodium heat pipes, or even the TIC direct fuel contact concept where the secondary side of the TIC is cooled with sodium.

Another change is in the reflector material. In the reference case Zr_3Si_2 was used as an axial and radial reflector. Zr_3Si_2 is a relatively high albedo reflector that does not contribute heavily to neutron slowing down. The neutron yield for plutonium and the capture to fission ratio are sensitive to the spectrum; therefore the reflector was chosen for the RGP core to mitigate spectrum softening from the return current. HEU is not as sensitive, and therefore a reflector with a higher albedo can be used even if that reflector softens the spectrum. Therefore, the HEU UHPDC uses a BeO reflector.

6.2 Core Size

A BOL study was done with 90% enriched UC fuel. The core is modeled as a smear of homogenous fuel, clad, and coolant in a cube of varying dimension. The BOL reactivity was calculated using MCNP. Based on preliminary screening, a core dimension of 25 cm was selected. Figure 9 shows a plot of the BOL eigenvalue (k_{eff}) as a function of the core dimension. In each case the minimum reflector thickness is 6 cm.

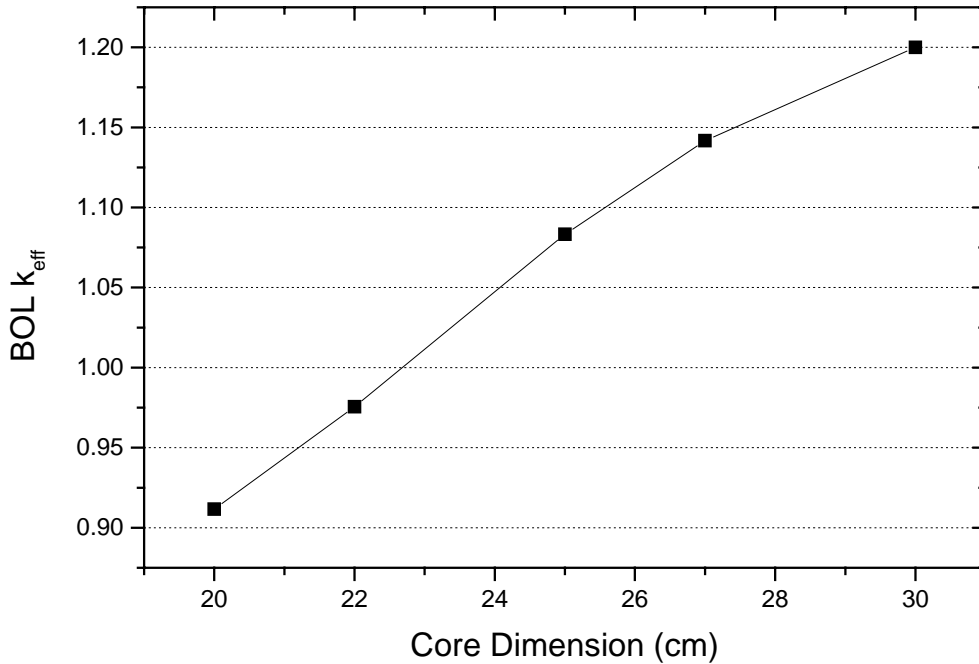


Figure 9: Core Multiplication Factor as a Function of Core Dimension

The RGP UHPDC has a BOL eigenvalue of 1.1. In the HEU case, the core dimension is 25 cm and the leakage is reduced such that 1.08 is sufficient to reach reasonable, though somewhat lower, burnup. The target burnup is approximately 40 MWD/kgHM (4.25 a/o), which corresponds to 380 EFPD (2 round trips) at 10 MW of thermal power and 1 MWe.

The RGP UHPDC was designed for 11 MW. When the core dimension is increased to 25 cm from 20 cm, the core volume roughly doubles, therefore, the HEU UHPDC will be able to produce ~20 MW of thermal power at the same power density.

For the high temperature sodium Rankine cycle PCU, a reactor thermal power of 27 MW is required to produce 3.4 MWe. The high power may require increasing the core dimension because of power density constraints. However, if a single reactor with core dimension of 25 cm is used to produce 27 MW of thermal power, the required burnup for 190 EFPD (1 round trip) is approximately 55 MWD/kgHM (5.7 a/o).

6.3 Core Life Studies

Burnup calculations were performed on the core model using MCODE, which is a code that couples MCNP and ORIGEN. The reactivity is plotted as a function of burnup for 10 MW of thermal power. The burnup behavior will not be heavily dependent on the power density because of the hard neutron spectrum and consequently relatively small fission product absorption cross sections. A plot of the HEU UHPDC reactivity as a function of burnup is shown in Figure 10.

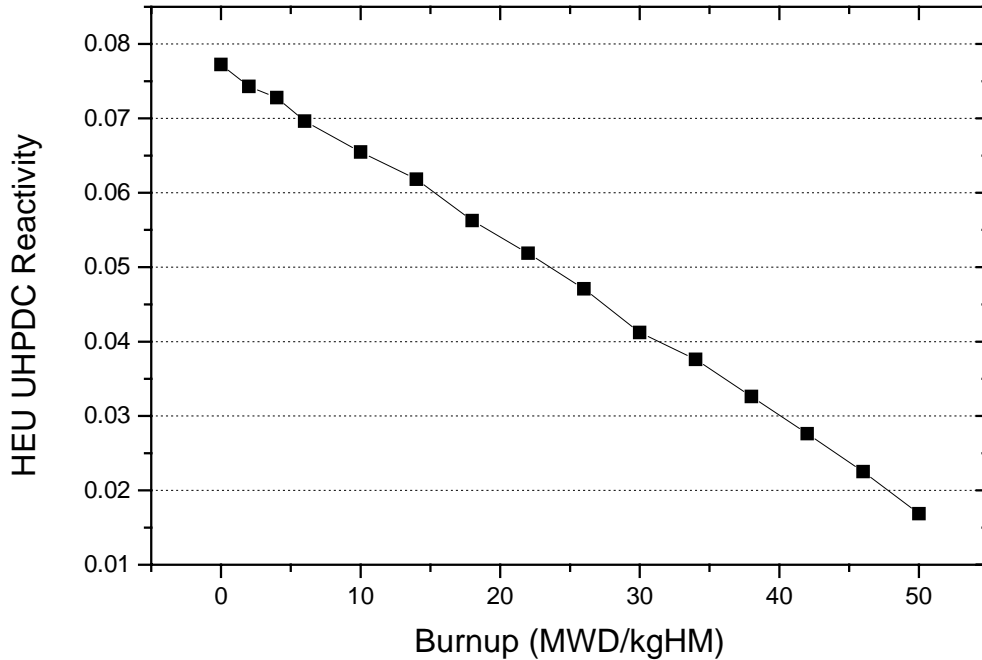


Figure 10: Reactivity History for the HEU UHPDC.

For the low power system (10 MWth) the desired burnup is 40 MWD/kgHM. This is easily achievable with the current design. In pushing the reactor system to 27 MWth, an effective full power life of 190 EFPD (or 55 MWD/kgHM burnup) seems achievable with minor or no changes to the design.

6.4 Control Mechanism

The RGP UHPDC uses direct leakage for reactivity control. The control mechanism is a series of rotating reflector plates that change the effective density of the reflector by as much as 50%. The reflector density in the BOL core model for the HEU UHPDC is varied between 100% and 50% to see the effect of the control device on the core reactivity. The core is most reactive at the BOL, and therefore, if the core can be brought to subcritical conditions at BOL, the control mechanism will be capable of fully controlling the reactivity swing through the life of the core.

Figure 11 shows the HEU UHPDC eigenvalue as a function of the reflector density. The dramatic drop in reactivity is expected because the small, cube-shaped core has a very high leakage probability.

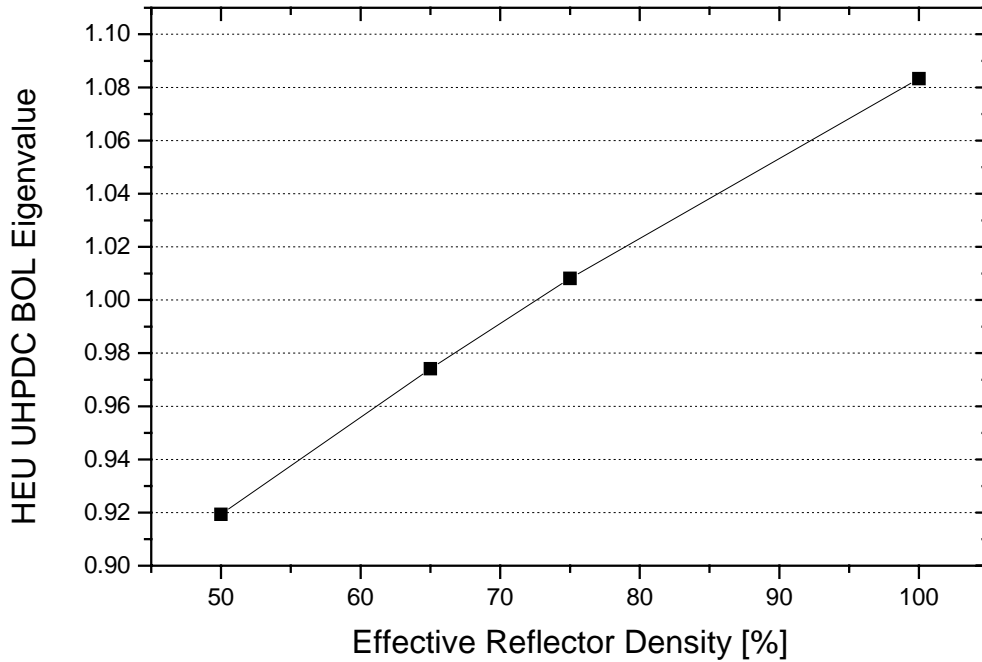


Figure 11: Effect of Control Device on BOL Eigenvalue

There is every confidence based on this BOL criticality behavior that direct leakage control will be sufficient to control the reactivity swing with the HEU UHPDC through burnup.

6.5 Void Reactivity

Void reactivity worth was evaluated for the HEU UHPDC. The worst case for voiding is when the coolant in the core is voided, but sequesters liquid coolant in the axial reflectors. Though the void reactivity in this scenario will be positive because there is no negative feedback due to enhanced axial leakage, it is calculated to ensure that the reactivity control devices will ensure shutdown as well as evaluating the shutdown margin during an accident scenario. This case was evaluated at BOL using the MCNP model.

Rotating drums in the radial reflector control the core. The drums have a reactivity worth that is effectively the same as altering the density of the radial reflector material between 50% and 100%. With the radial reflector effective density set at 50% (shutdown configuration) and the core coolant voided, the reactivity is negative, though higher than predicted from the shutdown configuration at BOL. The eigenvalue for the voided BOL core is 0.954(12), which is somewhat greater than the nominal shutdown configuration (eigenvalue of approximately 0.92 as shown in Figure 11).

6.6 Conclusions

The HEU UHPDC core characteristics are tabulated in Table V and compared with parameters from the RGP UHPDC. The HEU UHPDC appears to be a reasonable alternative. The HEU UHPDC volume is roughly double that of the RGP UHPDC.

Table V: RGP and HEU comparison

	RGP	HEU
Power	11 MWth	10 MWth
Core Dimensions	20x20x20cm	25x25x25cm
Total mass	185 kg	320 kg
Reflector thickness	6 cm	6 cm
Reflector material	Zr ₃ Si ₂	BeO
Coolant	(50:50NaF-ZrF ₄) molten salt	Na
Coolant volume fraction	40v/o	40v/o
Fuel	RG Pu carbide	90% enriched U carbide
Fuel volume fraction	55 v/o	55 v/o
Fuel element geometry	plates, arranged in honeycomb grid	plates, arranged in honeycomb grid
Cladding	Nb based refractory alloy	Nb based refractory alloy
k-eff BOL	1.1	1.08
EOL fuel burnup	12 a/o	4.3 a/o
Core lifetime	570 EFPD	380 EFPD

The RGP UHPDC reflector is much more dense than the HEU UHPDC reflector, and therefore the difference in mass is not as dramatic as initially expected, however, the HEU UHPDC mass is more than 70% higher than that of the RGP UHPDC.

Though the RGP UHPDC outperforms the HEU UHPDC with respect to critical mass and core lifetime, there is every assurance that an HEU UHPDC will still meet the minimum needs of a manned mission to Mars program.

This Page Left Intentionally Blank.

7.0 Summary and SELENE Overview

The current body of work has analyzed several power conversion technologies in terms of their likelihood for meeting the stringent demands of a Mars exploration program. Though the results of these studies are applicable to enabling a manned mission to Mars, the results are universal for any space nuclear power program.

The sodium Rankine cycle in combination with a highly enriched uranium fueled ultra high power density core may be sufficient to meet the power needs for future space exploration or other space applications. The issues related to coolant freezing, however, have yet to be solved.

Table VI summarizes briefly the results of analyses conducted on a variety of power conversion technologies. The highlighted options are for high power applications. Based on the comparison, the choice for developing the high temperature sodium Rankine cycle is obvious. Though the analyses have been simplified, the sodium Rankine cycle has a clear advantage.

Table VI: Power Conversion Technology Comparison

		T(hot)	T(rej)	Work	Efficiency
TIC	1 (low T)	1200 K	750 K	0.4 MW	12%
	2 (high T)	2200 K	750 K	0.9 MW	25%
	1 (high T)	2200 K	1200 K	2.5 MW	12%
Ar Brayton		1600 K	850 K	0.95 MW	20%
Na Rankine	low T	1200 K	1000 K	1.1 MW	11%
	high T	1500 K	1300 K	3.4 MW	13%

In addition to surveying several technology options for power conversion, the MIT RGP UHPDC was redesigned for HEU fuel. The trade offs between the two fuel forms can be established in an extensive cost-benefit analysis based on figures tabulated here as well as in previous work done at MIT concerning the radiotoxicity of the RGP at launch. There are many benefits to RGP including a much smaller and longer life system. However, an HEU UHPDC will still meet the needs for the Mars initiative.

The sodium Rankine cycle and thermionic conversion appear as likely candidates for future research initiatives in the area of space nuclear power. For a manned mission to Mars nuclear power systems must be capable of producing several megawatts of electric power.

Sodium Rankine cycle technology will require, in particular, research in the area of vapor metal turbines that can sustain relatively high exit quality. It is as of yet, unclear how such a turbine would be manufactured, or how large such a turbine would be. Additionally, the issues related to sodium freezing before the reactor is operational is another area of concern where future work is warranted.

TIC is another candidate for high power applications. Though the power levels are not as high as for the sodium Rankine cycle, TICs produce direct current without the need for moving parts in the system. To this end they reduce system complexity and increase system reliability. The largest hurdles in the implementation of the direct contact approach are the impact of fast fluence on TIC performance and the need for collector cladding.

The boiling sodium Rankine cycle was selected for the power conversion unit in the current work, and the reactor core is an ultra high power density core with HEU fuel. The sodium Rankine cycle

has many advantages, including high temperature quasi-isothermal heat rejection. The sodium-cooled, epithermal long-term exploration nuclear engine (SELENE) is designed to be scalable to meet many differing mission requirements.

The SELENE core is comprised of Nb-1Zr clad, lead bonded, UC plates in a honeycomb pattern. The fuel plates are arranged into a rectangular grid, roughly 25cm on each end. An isometric view of the reactor core is shown in Figure 8. The fuel is in two zones, one is 97 a/o enriched in ^{235}U and the other is 70 a/o enriched in ^{235}U . The core is BeO reflected, with a minimum radial thickness of 6cm.

Three designs are proposed, the first is for a 10 MWth / 1.0 MWe Low Temperature (1300 K) system (SELENE-10-LT) and the second for a 10 MWth / 1.2 MWe High Temperature (1500 K) system (SELENE-10-HT) and the third for a 27 MWth / 2.6 MWe system (SELENE-30). The LT and HT designators refer to the low and high temperature variants of the SELENE-10 design respectively.

The goal of the current work is to design a reactor and power conversion system that can easily be evolved from low to high power. SELENE is scalable from 1.0 MWe to 2.6 MWe with only incremental changes in the design. For the purposes of scalability and safety, the system is designed to have a reactivity-power coefficient of essentially zero in the range of operation. The technology for SELENE is transformational and smaller power systems can be used to demonstrate the technology and develop operational experience.

Three SELENE variants are proposed. Each of the variants operates with the same system components but operates in different temperature and flow regimes. The SELENE-10-LT, or the low temperature variant of the 10 MWth SELENE is meant to act as a technology test for the sodium Rankine power conversion and the reactor core. The temperature limits are not as high, thus requiring a less stringent materials development program and more reasonably assured system performance before scaling to higher temperature.

The SELENE-10-HT is the low power, high temperature variant. This cycle operates at slightly higher efficiency because of the higher temperature and low sodium velocity. The SELENE-30 is the most demanding design in terms of high sodium temperature and high sodium velocity. The low power variants will act as test beds to verify and test the technology necessary for the high power system.

SELENE was specifically designed to deliver multi-megawatt electrical power for use with a VASIMR (variable specific impulse magneto hydrodynamic rocket). The VASIMR will require on the order of 10 MWe. At the current power levels, 4 reactors will be required to power the VASIMR. A first generation SELENE will be capable of producing approximately 1 MWe of power, ideal for conventional electric propulsion, such as ion or Hall thrusters.

The SELENE is designed to fit inside a Titan IV rocket and meet the mass limitations for launch using this vehicle. It is yet uncertain if this is the launch vehicle that would be used for the SELENE however.

The unique SELENE design uses a cylindrical radiator that acts as armor for the core and balance of plant. The radiator consists of a series of tubes arranged to form an annulus at the inner periphery of the radiator. The tubes are inside the balance of plant armor, and the outer armor is coated with a high emissivity coating. A simple schematic of the system is depicted in Figure 12.

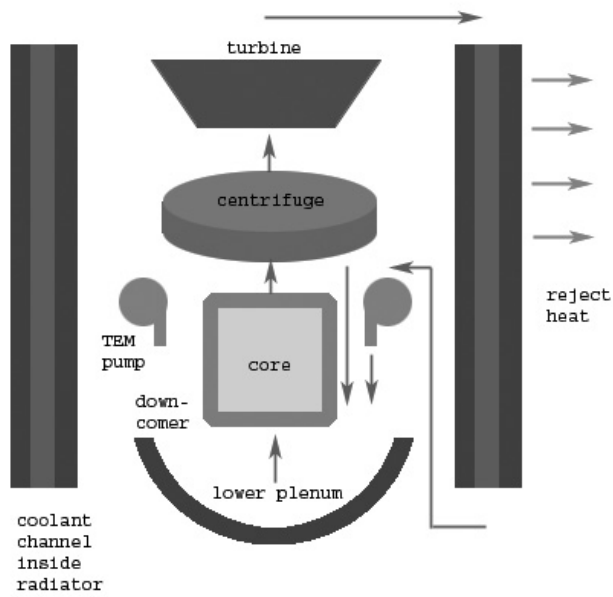


Figure 12: Simplified SELENE Schematic (not-to-scale).

The arrows on the right indicate that heat is rejected from the cycle by radiation; the arrows inside the radiator indicate the path of the sodium flow. Though the cycle will be discussed in more detail in subsequent sections, the unique design features are the dual purpose of the radiator to act as armor for the balance of plant.

This Page Left Intentionally Blank.

8.0 Sodium Rankine Cycle

The sodium Rankine cycle was selected for the power conversion for a variety of reasons. The coolant was selected because of its excellent heat removal properties, neutronic inertness in a hard spectrum, engineering experience with the coolant in terrestrial fast reactors, and its saturation properties. The blend of these characteristics makes sodium the ideal coolant for a space nuclear reactor. However, sodium has many drawbacks, including a relatively high freezing temperature and high chemical reactivity.

Liquid metals have been used in previous space reactor design because of their excellent heat removal capabilities, lending to high power density cores. Specifically in the case of SP-100, liquid lithium was selected for the reactor coolant. The primary motivation for selecting the Rankine cycle is the ability to reject heat quasi-isothermally. The potassium and sodium Rankine cycles are under investigation by NASA currently specifically because the phase transition allows for isothermal, high temperature heat rejection, lending to highly efficient radiators, and the fluid properties of the metals lend to small, compact cores.

8.1 Basic Cycle

Though the basic Rankine cycle is well understood based on terrestrial experience, many differences manifest themselves when working with high temperature, two-phase flows in micro-gravity. The basic cycle will be described, as well as the design envelope. Specific concerns related to micro-gravity and the high temperature will be discussed in subsequent sections.

In the cold leg of the cycle, the two-phase mixture from the turbine outlet flows through a radiator. The radiator is an armored cylinder with coolant channels that encases the core. If we neglect the pressure losses in the radiator, the coolant will be isothermal at the low pressure saturation temperature as the sodium condenses. In the analyses, the sodium temperature in the radiator is assumed constant, and approximately equal to the temperature of the radiator surface. To accommodate for the conduction temperature drop between the channel wall and the radiator surface, a conservative emissivity is assumed. Though these details will be discussed at further length in the subsequent sections, by making simplifying assumptions one can clearly illustrate the advantages of a Rankine cycle for space applications.

Let us assume that a Rankine cycle can operate at the Carnot efficiency and that the temperature of the radiator is the same as the saturation temperature of the cycle on the cold leg. If this is the case, we can write a simple relationship for the attainable useful work from the cycle, as shown in Equation 20.

$$W = \frac{\eta}{1 - \eta} Q_{RAD} \quad (20)$$

where W is the useful work,
 η is the efficiency of the cycle, and
 Q_{RAD} is the heat rejected by the radiator.

We can use the expression for the Carnot efficiency in terms of the hot and cold leg temperatures (in this case the high pressure and low pressure saturation temperatures of sodium, respectively), and express the reject heat in terms of the temperature. When we substitute in the appropriate relations, we arrive at Equation 21.

$$W = \frac{\eta}{1-\eta} Q_{RAD} = \frac{1 - \frac{T_C}{T_H}}{\frac{T_C}{T_H}} (\varepsilon \sigma A T_C^4) = (\varepsilon \sigma A) \left(\frac{T_H}{T_C} - 1 \right) T_C^4 = (\varepsilon \sigma A \Delta T_{core}) T_C^3 \quad (21)$$

where, T_C is the low pressure saturation temperature of the coolant,
 T_H is the high pressure saturation temperature of the coolant,
 ΔT_{core} is the temperature change across the core,
 ε is the emissivity of the radiator surface,
 A is the surface area of the radiator, and
 σ is the Steffan-Boltzmann constant.

If we assume that the temperature change across the core is a given constant, one can see that the useful work that can be attained from the cycle is given as the third power of the cold leg temperature. If the coolant on the cold leg side were not isothermal, one would have to integrate the heat transfer along the radiator length, correcting for the drop in temperature as the coolant rejects heat. For the case of a Brayton cycle, the heat is rejected at an effective temperature that is well below the turbine outlet temperature. In the case of the Rankine cycle, one makes the fullest use of the given radiator area by radiating heat at nearly the same temperature throughout.

By examining this simplistic model, one can arrive at conclusions about the design for a high power space nuclear reactor that may seem counterintuitive. In terrestrial applications, a primary design goal is to maximize the efficiency of a cycle to harness as much energy from the nuclear fuel as possible. For space applications, one of the primary constraints is the mass and volume of the radiator and armor. Effectively, the radiator surface area is constrained by the launch vehicle capability. To this end, it is essential to fully utilize the given radiator area and maximize the useful work by increasing the cold leg temperature of the cycle to as high as possible. By increasing the cold leg temperature, given an absolute limit by the fuel melting temperature (with some margin) it can be seen that the efficiency (here taken as the Carnot efficiency) will be smaller than for Rankine cycles as used terrestrially. The reactor only accounts for a small fraction of the mass therefore the goal is to maximize the useful work from the cycle without much consideration to the efficiency of the cycle.

Other limits exist beyond the melting temperature of the fuel, and there are other considerations that manifest themselves when one looks at the other components of the system. Of particular interest are the effects of pump and turbine irreversibility on the cycle efficiency, turbine exit quality on the reliability of the components, and sodium velocity on the integrity of the core structural components.

This work is not focused on the specifications for the turbine or pump design. Therefore, efficiencies for these components are assumed. As well as limitations on exit quality for the turbine. The pump will most likely be designed based on technology such as the thermo-electric electro-magnetic (TEM) pumps used in the SP-100 program [Dostal, et al.]. The turbine will be constructed out of a robust, high temperature material. For the purposes of this analysis, the turbine efficiency is assumed to be 90% and the pump efficiency is assumed to be 50%. One can see in later sections that the system power is not sensitive to the pump efficiency because of the very low pump work required.

The turbine outlet quality is limited such that the two-phase sodium flow from the outlet of the turbine will have a flow quality of at least 90%. This is to avoid significant damage to turbine blades as a result of liquid drop impingement. Terrestrial steam turbines operate typically with exit quality in

excess of 90%, currently it is not certain if 90% is too low to give reasonable assurance of turbine reliability at very high temperature.

Though there are concerns specific to operating the Rankine cycle in space due to the lack of gravity, the basic cycle remains very similar to those currently employed terrestrially. The methods for computation of flow characteristics will be discussed in subsequent chapters. Figure 13 illustrates a potential sodium Rankine cycle with ideal components on a T-s diagram.

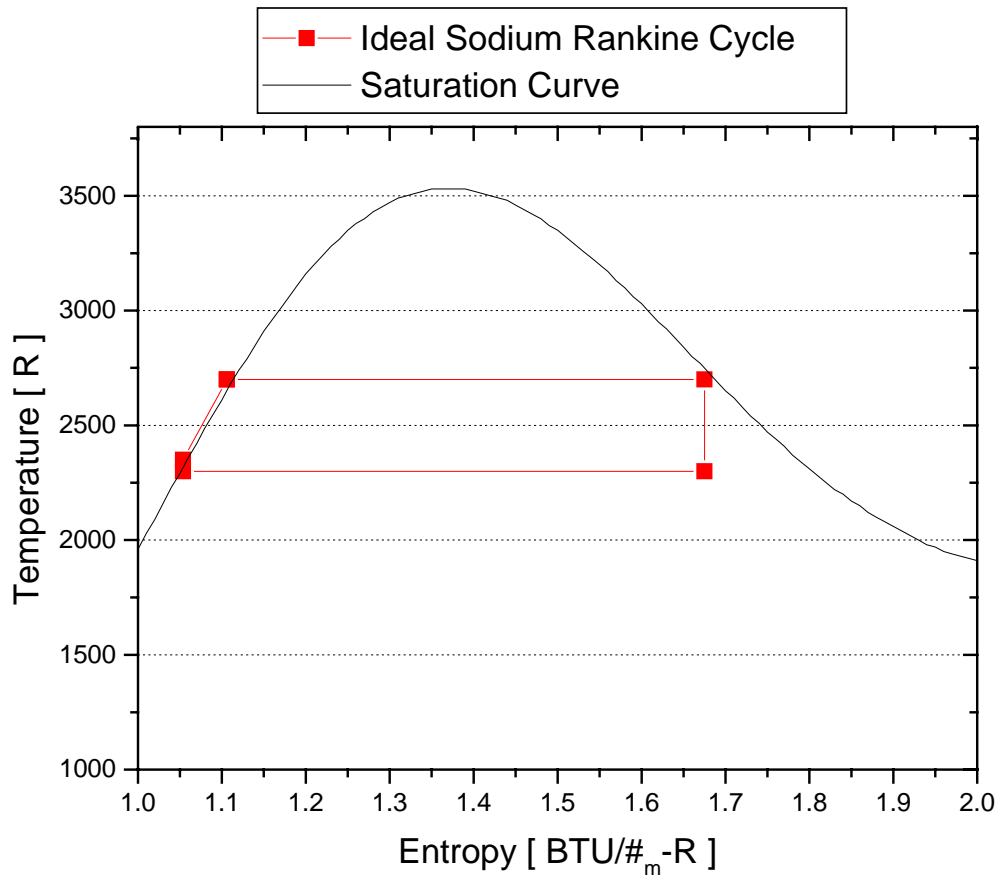


Figure 13: Ideal Sodium Rankine Cycle (extrapolated) [Todreas, et al.].

Sodium liquid is pumped through the reactor core. In the core, the sodium is heated by the nuclear fuel elements and begins to boil. The sodium vapor is separated from the two-phase flow after passing through the core, and the sodium vapor expands through a turbine. As the sodium expands, part of the vapor condenses to liquid in the turbine. The two-phase, low pressure sodium then enters the radiator coolant channels, where it rejects heat to the radiator, and condenses further to a saturated liquid. The saturated liquid is then pumped back into the core. Though this type of power conversion cycle is well understood, there are many key differences between operating such a cycle on Earth and in space. These differences are addressed in the following sections.

8.2 Two-phase Flow in Micro Gravity

The major difference between the space Rankine cycle and the terrestrial Rankine cycle is the absence of gravity in space. It is critical to account for this difference because the buoyancy force that arises due to gravity leads to different flow regimes with dramatically different heat removal properties.

The buoyancy force refers to the tendency for vapor in a two-phase flow to rise through a core faster than the liquid portion of the flow, contributing to a difference in the velocities of the two-phases. This is an area of particular interest for space applications, and currently research is being done at Texas A&M University on boiling sodium flow characteristics in micro-gravity [Valota]. For the purposes of this analysis, however, a homogenous equilibrium model is used to calculate heat transfer and flow characteristics for the flow. Though this approach is often a poor approximation for terrestrial applications, the absence of gravity eliminates the buoyancy force that drives vapor to flow more quickly than liquid. Therefore, it is likely that two-phases will travel through the core with similar velocities, making the homogeneous equilibrium model more appropriate. However, it should be noted that the use of this model as an appropriate means for calculating heat transfer characteristics is conjectural at this stage.

8.3 Vapor Separation

For terrestrial Rankine cycles, gravity plays an important role in the separation of the vapor and liquid phases at the core outlet. The low density vapor naturally rises above the liquid due to the buoyancy force. Without gravity, it is likely that the surface tension of the liquid would drive the flow to form dispersed sodium droplets in the vapor.

At the core outlet, the sodium flow will be predominantly vapor, however, the core exit quality may only be as large as 65%. The quality is far too low to be sent to the turbine directly, so the vapor must be separated from the liquid. To perform the separation, a centrifuge will likely be required.

The centrifuge will operate beyond the core outlet as shown in Figure 12. The sodium is driven into the centrifuge by the pumping pressure. The centrifuge is essentially a ring that rotates. The friction between the ring wall and the fluid as well as the viscosity of the fluid leads to the formation of a vortex. The centrifugal force will drive the flow to separate, thus forming a vapor core and liquid annulus. The liquid is drawn to the periphery of the vortex because of its higher density. The vapor in the core of the centrifuge can then be directed to the turbine. The liquid in the annulus must be directed through a down-comer back into the core.

8.4 Jet Pump

Directing the liquid flow through a down-comer to reenter the core is also complicated by the absence of gravity. On Earth, the pressure head produced by the density difference between the two-phase sodium in the core, and the liquid sodium in the down-comer would be sufficient to redirect the flow. Though, the exact method for accomplishing this in space has not been decided, it is suggested that a jet pump may be able to create a suction force that will draw the sodium liquid annulus from the centrifuge back through the core. The primary coolant TEM pump can pump the cool liquid sodium from the radiator through a nozzle into the down-comer and potentially drag the heated sodium back through the reactor core.

9.0 Thermal Hydraulic Analysis

Thermal hydraulic analysis is done using a finite elements approach for an average channel to compute the average flow characteristics and useful work attainable from the cycle for three variants of the SELENE design. For purposes of assessing the viability of the design a parallel approach is used to conduct hot channel analyses as discussed in a subsequent chapter.

This chapter will cover the methodology for computing the average channel flow and heat transfer characteristics. The core is based on an ultra-high power density core design using simplified models, and while the design process is iterative, the methodology will be discussed in detail here along with results from the final computations for the completed design, relegating the relevant discussion about the reactor physics component of the design to the following chapter.

The core is a series of Nb-1Zr clad UC fuel plates in a honeycomb pattern. The pitch between plates is 5.5 mm. The cladding thickness is approximately 0.085 mm. Though the plates seem very small, the University of Florida has proposed similar fuel arrangements with equally narrow fuel elements and verified manufacturing processes for these types of elements [Dostal, et al.].

The UC fuel is stoichiometric and taken at a smear density of 85% theoretical density for the SELENE-10 variants and 90% for SELENE-30. The smear density refers to the mass of fuel in the plates divided by the volume. The smear density is always less than the theoretical density because the fuel is manufactured or packed with some porosity and bond material to accommodate for fuel swelling and expansion. The bond material is lead, which will melt without a change in density during reactor startup.

Though the fuel manufacturing process has not been fully analyzed, there are a variety of concerns with developing this fuel form. These will be discussed at greater length in a later chapter. The honeycomb pattern of the fuel plates forms approximately 2000 small channels with a square cross sectional flow area. The equivalent diameter for these channels is 3.68 mm. The core is 25 cm tall along the flow path with 2 axial reflector regions each 6 cm long, for a total flow channel length of 37 cm.

9.1 Average Channel Finite Element Methodology

The thermal hydraulic analysis of the core is conducted on an average flow channel for the core. The channel is modeled with 100 planar slices through the active region, and 1 for each reflector region, for a total of 102 axial slices. In the core region each slice is 2.5 mm tall along the flow direction and 5.5 mm on each side. Figure 14 shows a cross-sectional view of the unit cell.

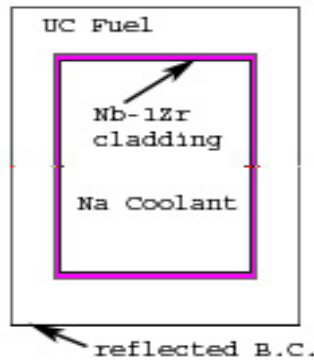


Figure 14: Unit Cell Schematic

Since the sodium boils in the channel above the core inlet, several models are needed to model the heat transfer and pressure drop in the core. The ultimate parameter of interest is the peak fuel temperature. The honeycomb pattern and thin cladding will facilitate keeping the fuel temperature relatively near the saturation temperature of the sodium.

Since both the pressure drop and heat transfer characteristics must be calculated in each cell, and there are three potential regimes for the sodium flow, a variety of models and assumptions are used. First, the sodium flow in the average channel may be either liquid, or two-phase. In the hot channel there is the potential to superheat the sodium, so there is a third regime where the entire flow is vapor. In the two-phase regime, the homogenous equilibrium model is used, and in the first and second regime, appropriate steps are taken to calculate the pressure drop and heat transfer using single phase models. In the following sections, the equations used will be discussed separately for each regime.

In the case of the average channel, the equations are set up such that a computer can iterate the mass flow rate until the system converges. This is done by comparing the calculated sodium temperature at the point of boiling to the saturation temperature and ensuring a small enough error as well as assuring that the heat rejected from the radiator is correct for the given mass flow rate. Since sodium properties are taken from a variety of sources, and there are only 100 elements in the core model, the tolerance on the saturation temperature is rather large (approximately 3%).

The thermal hydraulic analysis is coupled with the reactor physics calculations, particularly when determining the axial power profile. A reactor model is used to calculate the power shape based on 25 axial slices, and the power in each cell is converted to a normalized power fraction. The heat generated in each axial slice of the thermal hydraulic model is taken as one quarter of the power fraction for the more coarse 10 mm slices in the reactor physics model. The distribution of the power axially in the core determines the distribution of the sodium density in the channel. This is then fed back into the reactor physics model to calculate the axial power shape. This procedure was repeated until the solution converged. This is a tedious procedure, and only the final results will be quoted in this thesis.

Since the calculation is iterated on the mass flow rate, the mass flow rate is first calculated based on the heat rejected by the radiator and the saturation properties of the sodium. Equation 22 shows a heat balance that relates the change in enthalpy in the radiator to the radiator temperature.

$$Q_{RAD} = \varepsilon \sigma A T_C^4 = \dot{m}_{RAD} (h_{TO} - h_{PI}) \quad (22)$$

where, the left hand side of the equation is the radiation rejection heat,
 \dot{m}_{RAD} is the mass flow rate,
 h_{TO} is the turbine outlet enthalpy
 h_{PI} is the pump inlet enthalpy

Without knowing the pump work apriori, it is very difficult to set up an iterative process to calculate the core inlet enthalpy. However, the core is very small, and there is no gravity, lending to a small pressure drop. Since the pump is operating on high density liquid metal, the required pump work will be very small; this will be substantiated by calculations of the core pressure drop and cold leg volumetric flow rate in later sections. However, since very little pump work is needed, the iteration process can be greatly accelerated and simplified if the pump inlet and core inlet enthalpy are assumed to be approximately the same. This assumption has been verified by noting the small requirement on pumping power at the end of the calculation.

The emissivity is assumed to be 85%. Coatings are available with emissivity as high as 93%, The lower value is assumed to add conservatism to the calculation since the assumption that the radiator temperature is approximately the sodium saturation temperature effectively increases the calculated amount of reject heat.

The turbine outlet enthalpy is calculated based on the requirement that the turbine outlet quality be 90%. This is calculated according to the saturation properties of sodium at the low pressure of the cycle as shown in Equation 23.

$$h_{TO} = h_g^{LP} (x_{TO}) + h_f^{LP} (1 - x_{TO}) = h_g^{LP} (0.90) + h_f^{LP} (0.10) \quad (23)$$

where, h_g^{LP} and h_f^{LP} represent the enthalpy of saturated vapor and liquid respectively, and x_{TO} is the quality at the turbine outlet.

Recall that the mass flow through the radiator must be equivalent to the mass flow rate of vapor from the core. The mass flow rate through the core can then be calculated based on the exit quality of the flow from the core. Equation 24 shows the relationship between the known radiator mass flow rate, the core exit quality, and the core mass flow rate.

$$\dot{m}_{RAD} = x_{ex} \dot{m}_{CORE} \quad (24)$$

where, x_{ex} is the exit quality at the core outlet, and
 \dot{m}_{CORE} is the mass flow rate through the core.

The outlet quality is calculated based on the heat transfer from the fuel to the sodium. For each design, the saturation properties of sodium at the low and high pressure of the cycle must be specified. The inherent assumption is that the saturation properties do not change through the height of the core. This is the case where the core pressure drop is small compared with the operating pressure. For the calculated cases the pressure drop across the core is at most 4.4% of the operating pressure. Despite the slight pressure change through the core, as one examines the saturation properties for sodium, one can see that the properties are indeed not very sensitive to the pressure.

Table VII summarizes the saturation properties for the three proposed systems, giving the saturation enthalpies, specific volumes, saturation pressure for a given temperature, heat capacity, conductivity, and the viscosity.

Table VII: Saturated Sodium Properties

T_{sat}^1	K	1000	1278	1300	1500
P_{sat}^1	bar	0.200	2.780	3.260	11.139
h_g^1	kJ/kg	5044.7	5134.1	5140.5	5194
h_f^1	kJ/kg	1020.3	1373.7	1402.4	1671.4
v_g^1	m ³ /kg	16.60	1.44	1.24	0.40
v_f^1	m ³ /kg	0.0012808	0.0014051	0.0014163	0.0015308
$c_p(l)^1$	kJ/kgK	1.2529	1.2992	1.3057	1.3845
$c_p(v)^1$	kJ/kgK	2.6337	2.6053	2.5895	2.3543
$k(l)^1$	W/mK	54.24	44.70	44.00	38.24
$k(v)^2$	W/mK	0.045	0.048	0.048	0.050
$\mu(l)^1$	kg/ms	0.0001808	0.0001454	0.0001433	0.0001279
$\mu(v)^3$	kg/ms	0.00001475	0.00001475	0.00001475	0.00001475

1:[NTUA], 2:[Fink, et al.], 3:[Fan, et al.]

Having specified the iteration scheme used to solve for the core mass flow rate, the equations used for the heat transfer and pressure drop calculations in each axial cell for each regime will be described below.

9.2 Liquid Regime

Though there are three proposed configurations for the SELENE, in each case the sodium is subcooled at the inlet of the core. The formulae for heat transfer and pressure drop in the single-phase portion at the bottom of the core are relatively simple. The finite element approach balances the heat generated in each cell with the net outflow of energy from the cell. The heat generated in the average channel is calculated by taking the total core power, dividing by the number of channels and then multiplying by the power fraction in the cell as calculated by the reactor physics codes.

The inlet enthalpy is assumed to be the same as the radiator outlet even though there will be a slight difference because of the energy added by the main circulation pump. It is also assumed that the subcooled liquid is incompressible and has a constant specific heat at constant pressure. Given these assumptions it is possible to calculate the change in enthalpy and the change in sodium temperature across the axial slice according to Equations 25 and 26.

$$\frac{P}{N} f_i = \dot{m}_{CHANNEL} (h_i^{out} - h_i^{in}) = \frac{\dot{m}_{CORE}}{N} (h_i^{out} - h_i^{in}) \quad (25)$$

$$h_i^{out} = h_{i+1}^{in}$$

where, P is the core thermal power,
 $\dot{m}_{CHANNEL}$ is the average mass flow rate through a channel in the core,
 N is the number of channels in the core,
 f_i is the power fraction in the ith slice,
 $h_{i,out}$ is the enthalpy of the flow at the upper axial face of the ith slice, and

h_i^{in} is the enthalpy of the flow at the lower axial face of the i th slice

For the temperature we can relate the change in enthalpy to the change in temperature by using the specific heat and assuming that the pressure drop through the core is small.

$$\begin{aligned} c_p (T_i^{out} - T_i^{in}) &= (h_i^{out} - h_i^{in}) \\ T_i^{out} &= T_{i+1}^{in} \end{aligned} \quad (26)$$

where, T_i^{out} is the temperature of the flow at the upper axial face of the i th slice, T_{i+1}^{in} is the temperature of the flow at the lower axial face of the $(i+1)$ th slice, and c_p is the specific heat at constant pressure.

Given the properties at the inlet of the core, one can increment through the axial slices from 1 to 25 through the core equating the outlet enthalpy and temperature of a given cell to the inlet enthalpy and temperature of the next cell.

This approach is valid until the outlet temperature exceeds the saturation temperature, at which point saturated boiling occurs. At this point the methodology for calculating the flow heat transfer is changed. However, the temperature of the fuel and pressure drop must still be calculated.

The pressure drop from friction and acceleration are calculated for each slice. The mass flux, flow velocity, and Reynolds number are calculated simply according to the formulae in Equations 27, 28, and 29 respectively.

$$G = \frac{\dot{m}_{CHANNEL}}{A} = \frac{\dot{m}_{CHANNEL}}{D_{eq}^2} \quad (27)$$

where, G is the mass flux
 A is the cross sectional area, and
 D_{eq} is the equivalent hydraulic diameter.

$$v = \frac{G}{\rho} \quad (28)$$

where, v is the flow velocity, and
 ρ is the sodium density.

$$Re = \frac{\rho v D_{eq}}{\mu} \quad (29)$$

where Re is the Reynolds number, and
 μ is the viscosity.

In the liquid regime there is no pressure drop due to acceleration (assuming incompressible flow), so only the friction pressure drop need be considered. Since the flow velocity is high in each case, the flow is taken to be turbulent and the McAdams and Blasius relations are used to calculate the friction factor. The McAdams relation is used when the Reynolds number is greater than 30,000 and the Blasius relation is used otherwise. The McAdams and Blasius relations are shown below in Equations 30 and 31 respectively [Todreas, et al.].

$$f = \frac{0.184}{\text{Re}^{0.2}} \quad (30)$$

where f is the friction factor.

$$f = \frac{0.316}{\text{Re}^{0.25}} \quad (31)$$

The friction pressure drop is thus calculated for a given cell by the formula shown in Equation 32

$$\Delta p_{f_i} = \frac{-f}{2D_{eq}} G^2 v_f (z_i^{out} - z_i^{in}) \quad (32)$$

where, Δp_{f_i} is the friction pressure drop across cell i,
 z_i^{out} is the axial position at the top of the ith axial slice, and
 z_i^{in} is the axial position at the bottom of the ith axial slice.

The total pressure drop is found at the end of the calculation by summing all of the individual pressure drops across each of the cells.

The next step in the calculation is to find the fuel temperature. This calculation is done in two steps. First the heat transfer coefficient for the sodium must be calculated. Once the heat transfer coefficient is known, a thermal resistance approach is used to calculate the fuel temperature based on the sodium temperature. The heat transfer coefficient is calculated using a Lyon-Martinelli correlation, shown in Equation 33 [Chen].

$$h = \left(7.0 + 0.024[Pe]^{0.8}\right) \frac{k_f}{D_{eq}} = \left(7.0 + 0.024 \left(\frac{GD_{eq}}{\mu_f}\right)^{0.8} \text{Pr}_f^{0.8}\right) \frac{k_f}{D_{eq}} \quad (33)$$

where, h is the heat transfer coefficient,
 k_f is the thermal conductivity, and
 Pr_f is the Prandtl number for the saturated liquid.

Based on the heat transfer correlation, we can calculate the thermal resistance between the center of the fuel plate and the bulk sodium. The thermal resistance in any axial cell is given by Equation 34.

$$R_{th} = \frac{1}{h} + \frac{x_c}{k_c} + \frac{x_F}{4k_F} \quad (34)$$

where, R_{th} is the thermal resistance,
 x_c is the clad thickness,
 x_F is the fuel thickness,
 k_c is the clad conductivity, and
 k_F is the fuel conductivity.

The conductivity of the cladding is assumed to be constant and is 53.7 W/m-K [Hodgman]. The fuel conductivity is a function of temperature. The fuel conductivity in the first cell is predicted based on the sodium inlet temperature. The fuel conductivity in each successive cell is evaluated for the fuel temperature in the previous cell. The fuel conductivity correlation is given in Equation 35 [Lewis].

$$k_{F_i} = 10.28 + (0.00973)T_{F_{i-1}} - (0.00000188)T_{F_{i-1}}^2 \quad (35)$$

where, k_{Fi} is the fuel conductivity in the i th cell in W/m-K, and T_{Fi} is the fuel temperature in the i th axial cell.

Based on the thermal resistance, we can calculate the difference in temperature between the fuel and the bulk coolant given the heat flux. The heat flux is calculated directly from the channel dimensions and the cell power. Equation 36 shows the temperature difference as a function of the dimensions, cell power, and thermal resistance for an arbitrary axial cell.

$$T_{Fi} - T_{bi} = q''_i R_{th} = \frac{q_i}{4D_{eq}(z_i^{out} - z_i^{in})} R_{th} \quad (36)$$

where, T_{bi} is the bulk temperature (previously calculated), q''_i is the heat flux in the i th cell, and q_i is the cell power in the i th cell.

Given the system of equations, once the mass flow rate is known, the pressure drop and fuel temperature can be calculated. The peak fuel temperature is found at the end of the calculation by searching through the cells to find the cell with the greatest fuel temperature; however, this final search cannot be conducted until the heat transfer equations are solved for the two-phase region as well.

9.3 Two-Phase Regime

In the portion of the core where the sodium flow is two-phase, a very similar procedure is used to calculate the fuel temperature and flow conditions. There are two major differences. Firstly, correlations have to be used for two-phase heat transfer and pressure drop, secondly, the sodium bulk temperature in this regime is constant.

The liquid flow formulae are used until the enthalpy at the top of a given cell exceeds the saturated liquid enthalpy. A new set of formulae is then used to compute the heat transfer and pressure drop for successive cells. The two-phase flow is approximated with a homogeneous equilibrium model.

The enthalpy is calculated the same way in the two-phase regime as in the liquid regime. The bulk temperature does not change in the two-phase regime, unlike the liquid regime. The change in enthalpy is used to calculate the flow quality as shown in Equation 37.

$$x_i^{out} = \frac{h_i^{out} - h_f}{h_g - h_f} \quad (37)$$

where, x_i^{out} is the quality at the top of the i th cell.

The enthalpy in the i th cell is assumed to be the same as the quality at the outlet of the i th cell. Given the enthalpy in the i th cell, using the homogenous equilibrium model, the void fraction can be calculated according to Equation 38 [Todreas, et al.].

$$\alpha = \frac{(h_f - h_i)\rho_f}{\rho_g h_i - \rho_f h_i - h_g \rho_g + h_f \rho_f} \quad (38)$$

where, α is the void fraction, and h_i is the enthalpy in the i th cell.

The first step in calculating the heat transfer coefficient is to calculate the Martinelli parameter according to the approximate expression in Equation 39. The ratio of the viscosities is neglected (taken as unity). This is a valid assumption because the Martinelli parameter is only loosely dependent on the viscosity.

$$\frac{1}{X_{tt}} = \left(\frac{x}{1-x} \right)^{0.9} \left(\frac{\rho_f}{\rho_g} \right)^{0.5} \left(\frac{\mu_g}{\mu_f} \right)^{0.1} \approx \left(\frac{x}{1-x} \right)^{0.9} \left(\frac{\rho_f}{\rho_g} \right)^{0.5} \quad (39)$$

where X_{tt} is the Martinelli parameter.

Based on the Martinelli parameter, the enhanced flow multiplier can be calculated for use in a modified Lyon-Martinelli heat transfer correlation. Equation 40 is the relation used to predict the enhanced flow multiplier. It is only applicable when X_{tt} is greater than 10 [Todreas, et al.].

$$F = 2.35 \left(0.213 + \frac{1}{X_{tt}} \right)^{0.736} \quad (40)$$

where F is the enhanced flow multiplier.

When the Martinelli parameter is less than 10, the enhanced flow multiplier is taken as unity. The modified Lyon-Martinelli correlation for the convective heat transfer is shown in Equation 41 [Chen].

$$h = \left[\delta + 0.024 F \left(\text{Re}_f^{0.8} \right) \left(\beta \text{Pr}_f \right)^\alpha \right] \frac{k_f}{D_{eq}} \quad (41)$$

$$\alpha = 0.4x$$

$$\beta = (1-x) + \frac{\text{Pr}_g}{\text{Pr}_f}(x)$$

$$\gamma = (1-x) + \frac{k_g}{k_f}(x)$$

$$\delta = 7.0(1-x)$$

Heat transfer from nucleate boiling is neglected. As will be shown in subsequent sections, the void fraction of the flow increases dramatically after the onset of bulk boiling, giving rise to a high velocity flow of predominantly sodium vapor. Under these conditions the convective portion of the heat transfer will be dominant. Additionally, neglecting the heat transfer due to boiling will give a conservative estimate of the peak fuel temperature. In terrestrial applications, lower power density systems have much less dramatic changes in coolant density with core axial height, and thus there is a significant portion of the core where appreciable nucleate boiling occurs and the coolant velocity, due to the more subtle change in coolant density, does not increase as dramatically through short distances, therefore it is only valid to neglect nucleate boiling in high power density cores where the coolant reaches large void fraction shortly after the onset of boiling.

The thermal resistance is calculated the same way as for the liquid regime with the heat transfer coefficient given by Equation 41. The pressure drop calculations, however, are different because the pressure drop due to acceleration must be considered in the two-phase region. The pressure drop due to friction is given in Equation 42.

$$\Delta p_{f_i} = \frac{-fG^2}{2D_{eq}} v_f \left(1 + \frac{v_g - v_f}{v_f} x_i \right) (z_i^{out} - z_i^{in}) \quad (42)$$

The pressure drop across the i th cell due to the acceleration is given by the formula in Equation 43. The difference is taken from the top and bottom of the i th cell.

$$\Delta p_{a_i} = G^2 \left[v_f \frac{(1-x)^2}{1-\alpha} + v_g \frac{x^2}{\alpha} \right]_{z_i^{in}}^{z_i^{out}} \quad (43)$$

where Δp_{a_i} is the pressure drop across the i th cell due to acceleration.

The total pressure drop is the sum of the pressure drops due to acceleration and gravity. In the average channel the flow at the exit of the channel is still two-phase. Therefore, the total pressure drop and maximum fuel temperature can be calculated based on the formulae in this section and the previous section. In the hot channel, where the power density is greatest, there is the potential to superheat the sodium. In that case formulae are necessary for evaluating heat transfer and pressure drop in the vapor regime.

9.4 Vapor Regime

The enthalpy is calculated in each cell, once the flow enthalpy exceeds the saturated vapor enthalpy, the flow is purely vapor. The vapor regime and the liquid regime are similar in that the sodium temperature increases with the axial position. However, a key difference is that the sodium density is related to the temperature, whereas in the liquid regime the sodium was assumed to be incompressible and independent of the temperature.

The change in the sodium temperature is computed using Equations 25 and 26, except the vapor specific heat is used instead of the liquid specific heat.

If one neglects the effect of pressure drop on the sodium properties, the sodium density is purely a function of the temperature. An ideal gas model is used to model the sodium density in the vapor regime. The sodium density as a function of temperature is given in Equation 44 and is evaluated at the temperature of the sodium at the bottom of any given cell.

$$\rho_i = \frac{T_{sat}}{T_i^{in}} \frac{1}{v_g} \quad (44)$$

where T_{sat} is the saturation temperature, and ρ_i the sodium density in the i th cell.

Other than the change in density, the pressure drop is calculated according to the formulae used in the liquid regime. The heat transfer coefficient is calculated according to the modified Dittus-Boelter formula shown in Equation 45 [Chen]. In any case, the heat transfer coefficient tends to be very

large, and thus the heat transfer from the fuel is almost entirely dictated by the fuel/clad conduction thermal resistance.

$$h = 0.024(\text{Re})^{0.8} \text{Pr}_g^{0.4} \frac{k_g}{D_{eq}} \quad (45)$$

The following sections in this chapter will summarize the results of the average channel analysis for the three proposed SELENE designs. The key parameters are the low and high temperatures of the cycle, operating pressure, the pressure drop, pump work, the useful work output, efficiency, mass flow rate, reactor power, radiator size, maximum sodium velocity, and maximum fuel temperature.

9.5 SELENE-10-LT

The SELENE design is transformational. Three designs are proposed specifically so that operational experience can be gained with simpler, low power, lower temperature versions before developing and launching a high power, high temperature system.

The first proposed design is for a relatively low temperature, low power system, SELENE-10-LT. The reactor power is 10 MWth and the saturation temperature at the operating pressure is 1300 K. The cycle operates at approximately 10.7% efficiency and rejects heat at 1000 K. The net useful work extracted from SELENE-10-LT is 1.07 MWe.

The turbine work is calculated based on the enthalpy drop across the turbine, an assumed turbine efficiency of 90% and the mass flow rate in the radiator. These parameters are calculated using Equations 23, 24, and 25. Equation 46 shows the formula for calculating the turbine work. The net useful work from the cycle is the difference between the turbine work and the pump work.

$$W_t = \eta_T \dot{m}_{RAD} (h_g - h_{TO}) \quad (46)$$

where, W_t is the turbine work, and
 η_T is the turbine efficiency.

The pump work is calculated based on the pressure difference between the hot and cold legs of the cycle and the pressure drop across the core. The pressure drop is calculated by summing the pressure drops across all of the cells in the model according to Equations 32, 42, and 43. The pump work formula is given in Equation 47.

$$W_p = \frac{1}{\eta_P} \dot{m}_{RAD} v_f (p_H - p_L + |\Delta p_{CORE}|) \quad (47)$$

where, W_p is the pump work,
 η_P is the pump efficiency,
 p_H is the hot leg or operating pressure,
 p_L is the cold leg pressure, and
 Δp_{CORE} is the pressure drop across the core.

The pump efficiency is assumed to be 50%. Experience with TEM pumps in the SP-100 program shows that such pumps with lithium coolant operate at efficiencies near 30%; the greater efficiency is selected here to reflect improvements in the technology since the SP-100 program [Dostal, et al.].

However, the pump work is on the order of several kilowatts, and subsequently a very small fraction of the net useful work.

The specific volume at the hot leg and cold leg pressures are very similar, so for the calculation the specific volume is taken at the hot leg pressure. In any case, the required pumping work is small so these approximations have very little impact on the final result. The net useful work is the difference between the turbine work and the pump work. However, increasing the pump work by an order of magnitude would still only have a marginal impact on the net useful work from the cycle. The cycle efficiency is the ratio of the net useful work to the reactor thermal power. Table VIII summarizes the operational parameters for SELENE-10-LT.

Table VIII: SELENE-10-LT Operational Parameters.

Hot Leg Temperature	1300	K
Hot Leg Pressure	3.26	bar
Cold Leg Temperature	1000	K
Cold Leg Pressure	0.20	bar
Peak Fuel Temperature	1351	K
Core Pressure Drop	0.14	bar
Sodium Outlet Velocity	108	m/s
Mass Flow Rate	2.84	kg/s
Net Useful Work	1.07	MW
Pump Work	2.48	kW
Efficiency	10.72	%
Radiator Size	180	m ²

While the axial power distribution is explicitly included in the unit cell model, the peak fuel temperature here refers to the peak fuel temperature in the average cell, and the radial power profile is not taken into account for the purposes of calculating the aggregate core behavior. The radial power distribution is taken into account when calculating the peak fuel temperature for the hottest channel, as described in a subsequent chapter.

If the cycle temperature is increased, a low power system can still be developed based on the same reactor thermal power and the sodium velocity can be reduced. The SELENE-10-HT is the same reactor with a high temperature variant of the sodium Rankine cycle.

9.6 SELENE-10-HT

The sodium average channel velocity in the SELENE-10-LT motivates the design for a parallel system with lower velocity flow to address concerns with very fast sodium flow. Experience from both the SELENE-10-HT and SELENE-10-LT will help to address the concerns with operating the reactor with high temperature and high velocity flows. Table IX summarizes the SELENE-10-HT operational parameters.

Table IX: *SELENE-10-HT Operational Parameters.*

Hot Leg Temperature	1500	K
Hot Leg Pressure	11.14	bar
Cold Leg Temperature	1000	K
Cold Leg Pressure	0.20	bar
Peak Fuel Temperature	1576	K
Core Pressure Drop	0.04	bar
Sodium Outlet Velocity	35	m/s
Mass Flow Rate	2.43	kg/s
Net Useful Work	1.18	MW
Pump Work	8.07	kW
Efficiency	11.81	%
Radiator Size	180	m ²

The cycle efficiency is higher than the SELENE-10-LT and the useful work is also a little higher for the same reactor thermal power (10 MWth). Experience from deploying these two systems will be essential in demonstrating the technology necessary to develop and operate the high temperature, high power version of the SELENE, which will rely on rapid sodium flows and high temperature operation.

9.7 SELENE-30

The SELENE-30 is a 27 MWth system with high temperature, high velocity sodium coolant. The operational parameters are summarized in Table X. The high thermal power is required to draw enough useful work to power a VASIMR with approximately 4 systems. The fuel temperature in the SELENE-30 is higher than in the previous cases. It is still significantly lower than the melting temperature for the fuel form (UC), but poses some concerns under transient conditions. The SELENE-30 core size may be increased to lengthen the reactivity limited lifetime, and hence effective full power days (EFPD) of core life. By doing so the power density will be reduced and the mass increased. For this design, a small core is being developed to have enough EFPD of life for one mission to Mars.

Table X: *SELENE-30 Operational Parameters.*

Hot Leg Temperature	1500	K
Hot Leg Pressure	11.14	bar
Cold Leg Temperature	1278	K
Cold Leg Pressure	2.74	bar
Peak Fuel Temperature	1606	K
Core Pressure Drop	0.43	bar
Sodium Outlet Velocity	100	m/s
Mass Flow Rate	9.72	kg/s
Net Useful Work	2.66	MW
Pump Work	26.34	kW
Efficiency	11.49	%
Radiator Size	180	m ²

Appendix C of this thesis contains many relevant plots produced by the thermal hydraulics model for the SELENE-30. The plots include, but are not limited to: the density, velocity, fuel temperature, and heat transfer coefficient variation over the length of the core.

This Page Left Intentionally Blank.

10.0 Reactor Physics and Burnup

Reactor Physics calculations were performed with MCODE. MCODE is a code developed at MIT that couples MCNP4c2 and ORIGEN2.1 to do reactor burnup calculations. Several core models were developed. An axial unit cell model of one coolant channel was developed to determine the axial power shape. A 2D plane model was also developed to investigate the radial power peaking. Lastly, a full core model was developed with axial and radial segments so that enrichment could be graded to flatten the radial power shape and evaluate the reactivity limited burnup, and thus determine the cumulative energy in the reactor.

The core is comprised of interlocking fuel plates in a honeycomb grid pattern. The plates form segregated square channels. Sodium flows in the square interstitial regions. The plates have a pitch of 5.5 mm, are 1.82 mm thick, and have an active height of 25.3 cm. The plates include 6 cm of BeO reflector in the plate at the top and bottom of the core. The plates are 25.3 cm long in either direction. There are 45 coolant channels in each radial direction, for a total of 2025 coolant channels and 2209 fuel plates. There are 47 fuel plates in either radial direction, however, the end plates have only one half of the normal uranium loading and the remainder is additional cladding. The core is radially sheathed in 6.75 mm of Nb-1Zr cladding, thus separating the fuel plates from the BeO radial reflector.

An axial unit cell model was used in conjunction with the thermal hydraulic model to predict the axial variation of the sodium density and axial power shape. The axial power peaking factor was analyzed using this model. The axial unit cell model is a single coolant channel with reflective boundary conditions at the centerline of the fuel on each side of the square. A diagram of the axial cell model is shown in Figure 15.

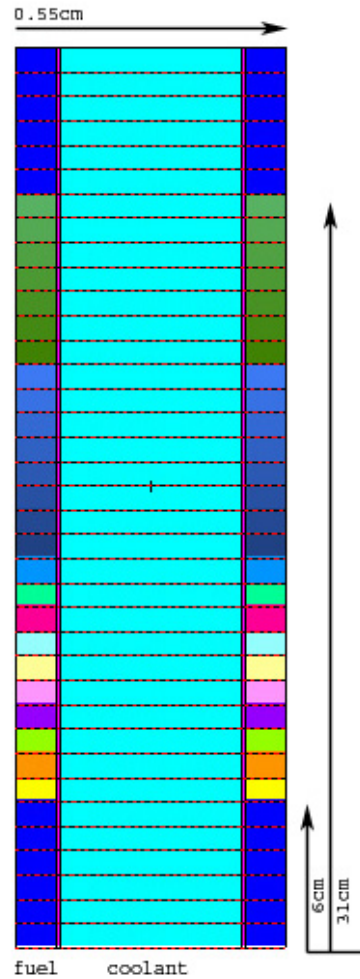


Figure 15: Axial Unit Cell Model.

The BeO reflector is modeled in MCNP4c2 as 6 axial slices each 1 cm thick. The fuel is segmented into 25 axial slices each 1 cm thick for a very accurate axial power distribution. The central region is the sodium coolant. The thermal hydraulic model accepts the discrete axial power distribution and predicts the sodium density variation axially. This sodium density distribution is then fed back into the axial cell model to recalculate the axial power shape. As will be shown later, the answer rapidly converges because of the very slight axial power peaking factor.

A radial plane model was also developed; the plane is the midplane of the core and the coolant channels are modeled with the core average sodium density. The model diagram is shown in Figure 16. This model was used to calculate the radial power shape. As will be discussed in subsequent sections of this thesis, the radial power was peaked towards the periphery of the core near the BeO reflector. The cause for the outward biased power shape is the spectral shift towards thermal as a result of moderation in the reflector. To reduce the radial peaking at the core periphery, an inner and outer fuel zone was included in the full core model, such that the uranium enrichment in the two zones could be graded to reduce power in the core periphery.

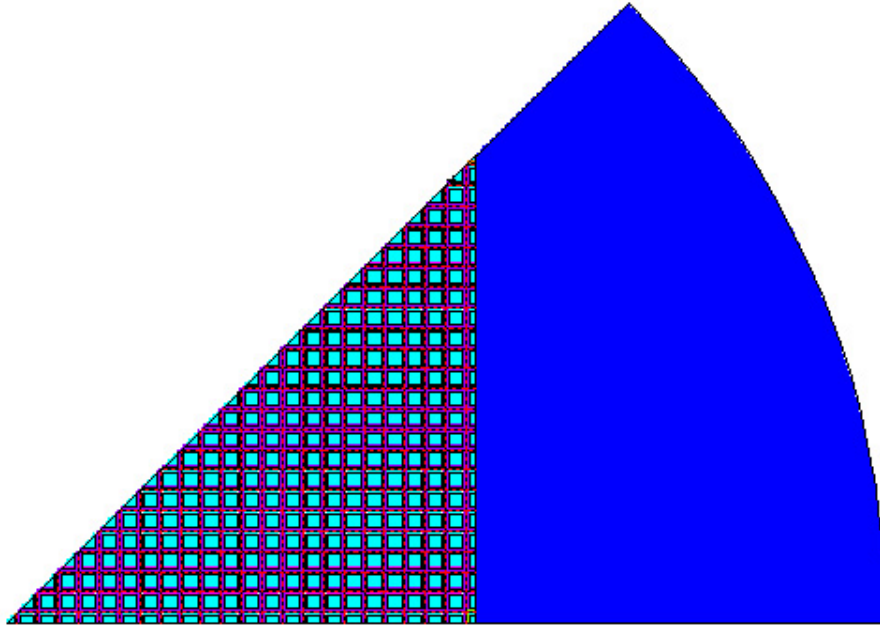


Figure 16:Radial Plane Core Model.

The radial plane core model is 1/8 core symmetric. The full core model, though including the axial variation in sodium density and axial reflectors is also 1/8 core symmetric. The MCNP4c2 input deck of the full core model is included in Appendix A of this thesis. A schematic of the core plate configuration is shown in Figure 17. The partial diagram shows an isometric view of the fuel plates with several removed.

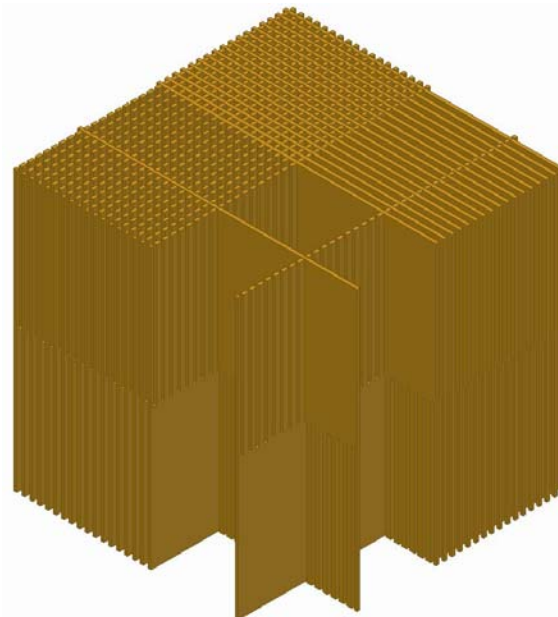


Figure 17:Isometric View of Fuel Plate Assembly.

The plates will be manufactured with interlocking “fingers” in one half of the plate. An individual plate will extend the entire core length. The fuel is modeled with a smear density between 85% and 90% of the theoretical density; the remainder of the volume will be used for a fuel bond material

which is not currently modeled in the reactor physics calculations. Though several potential bonding materials may be used, including perhaps a solid carbon buffer, the most promising candidate is liquid lead. While lead has excellent heat conduction properties and is neutronically inert in a fast spectrum, thermal expansion and expansion upon melting remain concerns. The density variation between room temperature and hot-full power will be approximately 11% [Zinov'ev]. The density variation, while complicating the manufacturing and startup of the reactor does not appear to be an insurmountable problem. The melting point of lead is 600K, well below the sodium temperature in the cold leg; The boiling point of lead is 2200 K, well below the fuel temperature of 1600 K under steady state operation, and still above the predicted 1900 K for extreme conditions. Lead has been identified as a candidate; however, no final choice has been made for the fuel bond.

10.1 Reactivity Limited Burnup

The reactivity limited burnup for the core is evaluated using a linear reactivity model (LRM) based on a few calculations of the core reactivity near the beginning of life (BOL). MCODE was used to calculate the core reactivity at BOL and after a burnup of 2 MWD/kgHM, 4 MWD/kgHM, 6 MWD/kgHM, and 10 MWD/kgHM. Based on the last three data points a linear regression was used to fit the data to a linear function. The initial two data points were excluded from the calculation because it overestimates the BOL reactivity. The reactivity falls dramatically early in life as the core reaches equilibrium concentration of strongly absorbing fission products.

Two cases were analyzed. In the first case the fuel smear density is 85% of the theoretical density. It is a very conservative quantity given the predicted fuel swelling rate, and a likely choice for SELENE-10 variants. The results of the regression gave an R^2 of 0.998, indicating that the trend is very nearly linear. The results of the calculation are plotted in Figure 18.

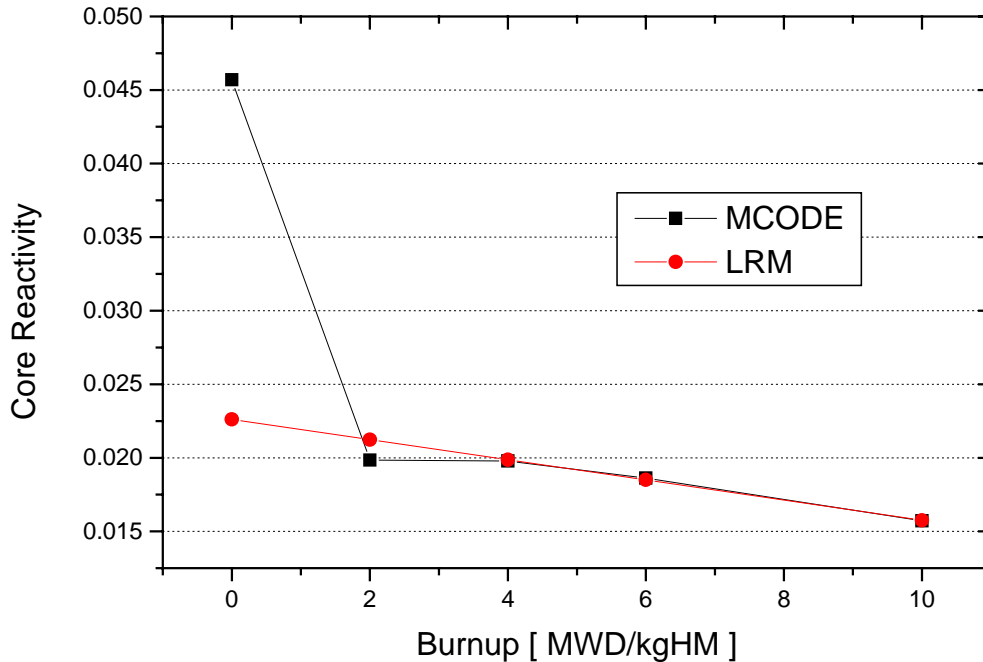


Figure 18: Partial Reactivity History for SELENE-10.

The LRM is given by Equation 48. Equation 48 is solved for the burnup point where the reactivity is 0, this is the definition of the reactivity limited burnup for a single batch reactor.

$$\rho = \rho_0 - AB = 0.022609 - 0.00069B \quad (48)$$

where, ρ_0 is the BOL reactivity accounting for steady state fission product poisoning,
 ρ is the instantaneous uncontrolled core reactivity,
 B is the instantaneous core burnup, and
 A is the slope of the trend line.

The cumulative energy is the total reactor power integrated over the lifetime of the reactor. The cumulative energy is calculated by taking the product of the heavy metal loading of the core and the reactivity limited burnup. By increasing the smear density (up to the limit given by the fuel swelling), the reactivity limited burnup and heavy metal loading are both increased. The effective full power lifetime of the core is given by the ratio of the cumulative energy to the reactor thermal power. Equation 49 shows the formula for calculating the effective full power lifetime (EFPL) of the core.

$$EFPL = \frac{\rho_0}{A} \frac{M}{P} = \frac{B_d}{p} \quad (49)$$

where, EFPL is the effective full power life,
 M is the mass of fuel,
 P is the reactor thermal power,
 B_d is the end of life, or reactivity limited burnup, and
 p is the specific power.

The specific power for the SELENE-10 core is 114 kW/kgHM, the predicted reactivity limited burnup is 33 MWD/kgHM. Given the result of Equation 48, the SELENE-10 EFPL is approximately 290 days.

The second case is for a fuel smear density of 90%, this will be required for the high power SELENE-30 variant in order to have enough cumulative energy in the reactor for at least one complete round trip to and from Mars. Figure 19 depicts the reactivity history for the SELENE-30 given the increased fuel smear density. The BOL reactivity is higher than in the case for the SELENE-10, though not outside the limit on controllable excess reactivity predicted for similar cores .

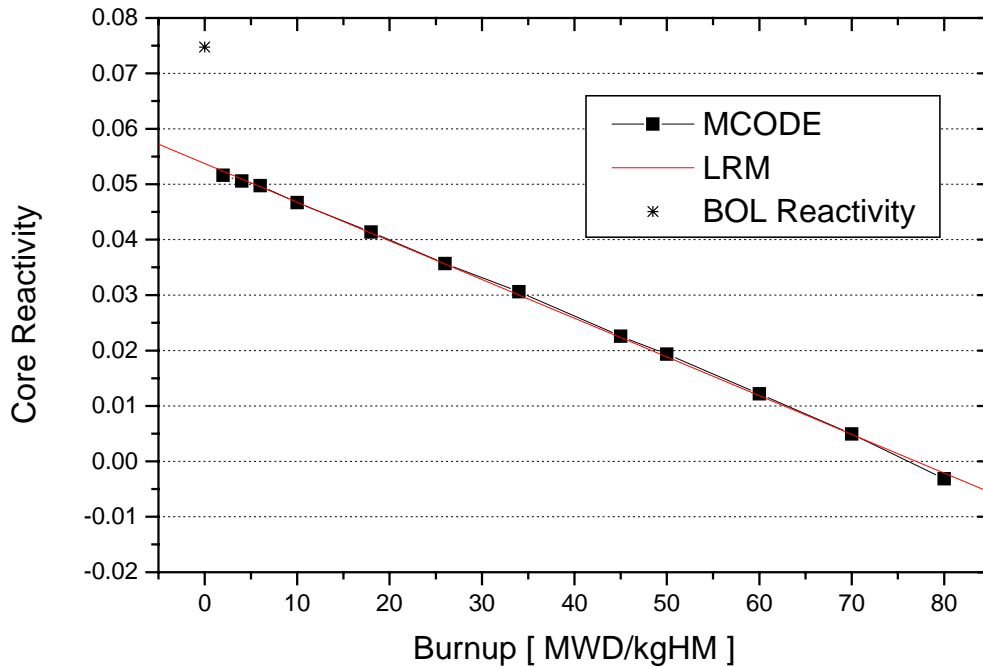


Figure 19: Reactivity History for SELENE-30.

The reactivity history was similarly fit with an LRM, the BOL reactivity is not included in the statistical sample, and the R^2 is 0.999. The LRM predicted reactivity limited burnup is 78 MWD/kgHM. This history is based on 11 of the 12 burnup steps (neglecting the BOL). Compared with the results in Figure 19, one can see that the LRM is an excellent model for predicting the SELENE core reactivity.

Table XI summarizes the reactivity limited burnup, cumulative energy, and EFPL for the SELENE-10 and SELENE-30. The EFPL in each case is approximately 9 months. When the smear density was increased from 85% to 90% for the SELENE-30 the increased loading and increased reactivity limited burnup compared with the SELENE-10 increase the cumulative energy dramatically so that the two systems have comparable effective full power lives.

Table XI: SELENE Lifetime Summary

		SELENE-10	SELENE-30
Thermal Power	kW _{th}	10,000	27,000
Heavy Metal Loading	kg _{HM}	87.7	92.8
Specific Power	kW _{th} /kg _{HM}	114.0	290.9
Reactivity Limited Burnup	MWD/kg _{HM}	33	78
Cumulative Energy	MWD	2,894	7,238
Effective Full Power Life	Days	289	268

10.2 Burnable Poisons

Burnable poisons were evaluated as an alternative approach to ex-core reflector control to potentially simplify the steady state operation of the reactor. A simplified analytical approach was employed.

The reactivity contribution of a burnable poison distributed in the reactor core is approximately given by the expression in Equation 50. It should be noted that this expression is only true when the burnable poison is distributed nearly homogenously and the core eigenvalue is near unity.

$$\rho^{BP} \approx \frac{\Sigma_a^{BP}}{\nu \Sigma_f} = \frac{N^{BP} \sigma^{BP}}{\nu N^{25} \sigma_f} \quad (50)$$

where ρ^{BP} is the reactivity contribution from the burnable poison,
 σ^{BP} is the absorption cross section of the poison,
 σ_f is the fission cross section,
 N^{BP} is the number density of the poison,
 N^{25} is the number density of the ^{235}U , and
 ν is the fission neutron yield.

Given that the core reactivity obeys an approximately linear behavior, we can calculate the slope of the reactivity through the effective full power life by computing the ratio of the calculated intercept in the LRM to the EFPL of the core. We can also calculate the time dependence of the number density of the burnable poison based on the neutron flux. The goal being to equate the reactivity contribution from the burnable poison to the excess reactivity of the core at BOL. Equation 51 shows a relationship for the burnable poison number density given the excess reactivity at BOL.

$$\rho^{BP} = \rho_0 = \frac{N^{BP} \sigma^{BP}}{\nu N^{25} \sigma_f} \quad (51)$$

$$\frac{N^{BP}}{N^{25}} = \rho_0 \frac{\nu \sigma_f}{\sigma^{BP}}$$

where ρ_0 is the excess reactivity at the BOL, and is given by the LRM intercept.

The rate of change of the reactivity contribution from the burnable poison is proportional to the rate of change of the number density of the burnable poison assuming that the fissile number density is approximately constant, which, in the case of small atomic percentage burnup is approximately the case. The rate of change in the reactivity contribution from the burnable poison is given in Equation 52.

$$\frac{d\rho^{BP}}{dt} \approx -\frac{\sigma^{BP}}{\nu N^{25} \sigma_f} N^{BP} \sigma^{BP} \phi \quad (52)$$

If we equate the rate of change in the burnable poison reactivity contribution to the time rate of change of the excess reactivity (which is approximately linear) we can relate the burnable poison absorption cross section to the number density of the poison, as shown in Equation 53.

$$\frac{\rho_0}{EFPL} = \frac{\sigma^{BP}}{vN^{25}\sigma_f} N^{BP} \sigma^{BP} \phi$$

$$\frac{N^{BP}}{N^{25}} (\sigma^{BP})^2 = \frac{\rho_0}{EFPL\phi} v\sigma_f = \frac{\rho_0}{\Phi} v\sigma_f$$
(53)

where Φ is the fluence.

Given the result of Equations 50 and 52, we can solve for the cross section of the burnable poison that would be required to meet the needs of the core near BOL, the result is shown in Equation 54.

$$\frac{N^{BP}}{N^{25}} (\sigma^{BP})^2 = \rho_0 \frac{v\sigma_f}{\sigma^{BP}} (\sigma^{BP})^2 = \rho_0 v\sigma_f (\sigma^{BP}) = \frac{\rho_0}{\Phi} v\sigma_f$$

$$\sigma^{BP} = \frac{1}{\Phi}$$
(54)

The burnable poison loading can now be calculated from Equation 50 and 53 as shown in Equation 55.

$$\frac{N^{BP}}{N^{25}} = \rho_0 \frac{v\sigma_f}{\sigma^{BP}} = \rho_0 v\sigma_f \Phi$$
(55)

For characteristic approximate values for the parameters, we can greatly narrow the search for the burnable poison candidates to control the reactivity. The core flux is going to be approximately 0.9×10^{14} /cm²-sec for a 10 MWth design on average. For an approximate effective full power lifetime of 350 days, the fluence is 0.0027 1/b. Based on Equation 54, the desirable absorption cross section is approximately 370 b. For a reactivity swing of 0.02, a fission yield of 2.5, and a fission cross section of 1.4 b, according to Equation 54, the desirable poison loading is 0.02%. These calculations would be rough estimates for the poison loading requirements for the SELENE-10 variant.

Since the reactor spectrum is relatively hard, the fluence relatively small, it will be practically impossible to control the entire core reactivity with burnable poison alone. The reactivity contribution at BOL from the burnable poison is related to the product of the loading and the cross section. For the given reactivity trend, it is desirable to load a very small amount of absorber with a very strong absorption cross section. However, in the epithermal reactor spectrum, standard poisons have absorption cross sections on the order of 10s of barns, not nearly 300 - 400 barns. Therefore, while the poisons may reduce the burden on reactivity control devices, they cannot account for the entire reactivity swing.

Also, the cross sections are so small that the burnable poison will not likely be self shielded. In the case of this relatively hard spectrum core, the burnable poison will act as though homogeneously distributed. In thermal reactors, where the 1/v cross section and low lying resonances contribute greatly to self shielding, the ash-layer burnout of the poison allows one to shape the reactivity contribution from the poison such that it decreases linearly with burnup [Driscoll, et al.]. It will be unlikely that such can be accomplished for a hard spectrum reactor. The flux spectrum in the inner core is plotted in Figure 20.

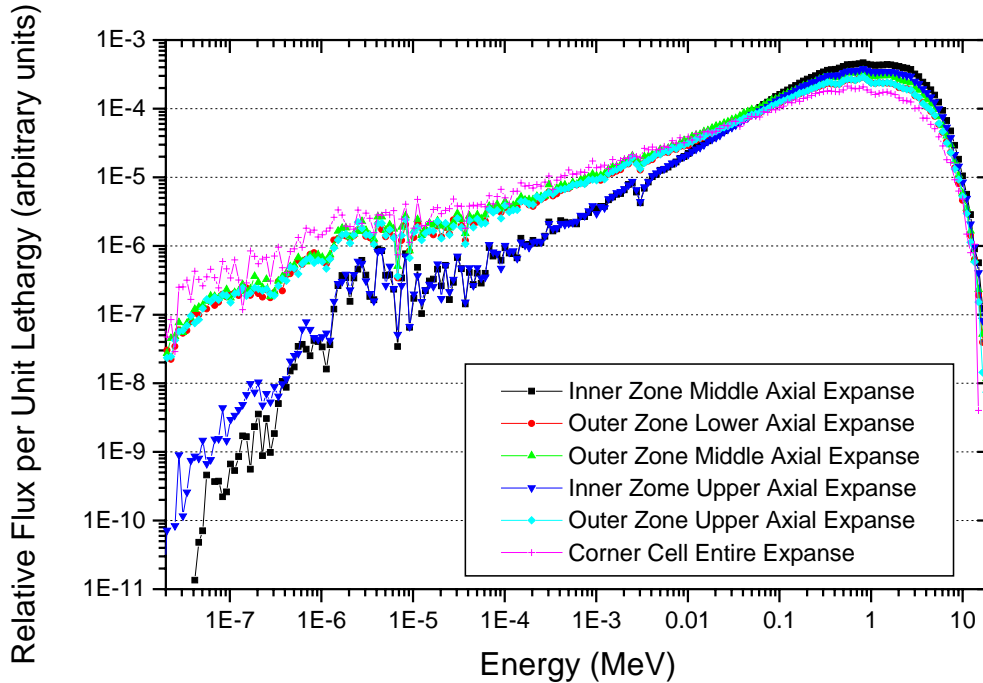


Figure 20: Normalized Flux per Unit Lethargy for SELENE-10-HT.

The most important aspects of the flux are the high energy, the fission source peak around 1 MeV, and the spectra in the outer zones, which tend to be much softer than the spectra in the inner zones. The spectra are shown here to illustrate the hardness of the neutron spectrum.

Since the rate of change of the burnable poison contribution to the core reactivity is the same as the slope of the excess reactivity at BOL, and the burnable poison will burnout more quickly than predicted by a linear model (because there is little if any self-shielding) the reactivity will increase from 0 during early burnup and reach a peak reactivity sometime during the middle of core life.

Since burnable poison cannot be used to control the reactor, and the reactivity swing is no greater than that predicted for earlier designs of ultra high power density space reactors, the current approach to reactor control will still rely on the ex-core control drums, even for steady state operation because it will be impossible to match the reactivity trend with burnup using burnable poisons alone.

10.3 Power Peaking Factors

The axial power peaking factor is calculated using a unit cell model as mentioned previously. The axial unit cell model was coupled with the thermal hydraulics model to calculate the axial power shape and the axial variation in the sodium density. The calculation rapidly converged because the axial power shape is almost completely independent of the axial variation of the sodium density.

A flat power profile was assumed for the SELENE-10-HT thermal hydraulic model, and the resultant axial variation of the sodium density was fed into the axial unit cell model. The axial power shape for several burnup steps is plotted in Figure 21.

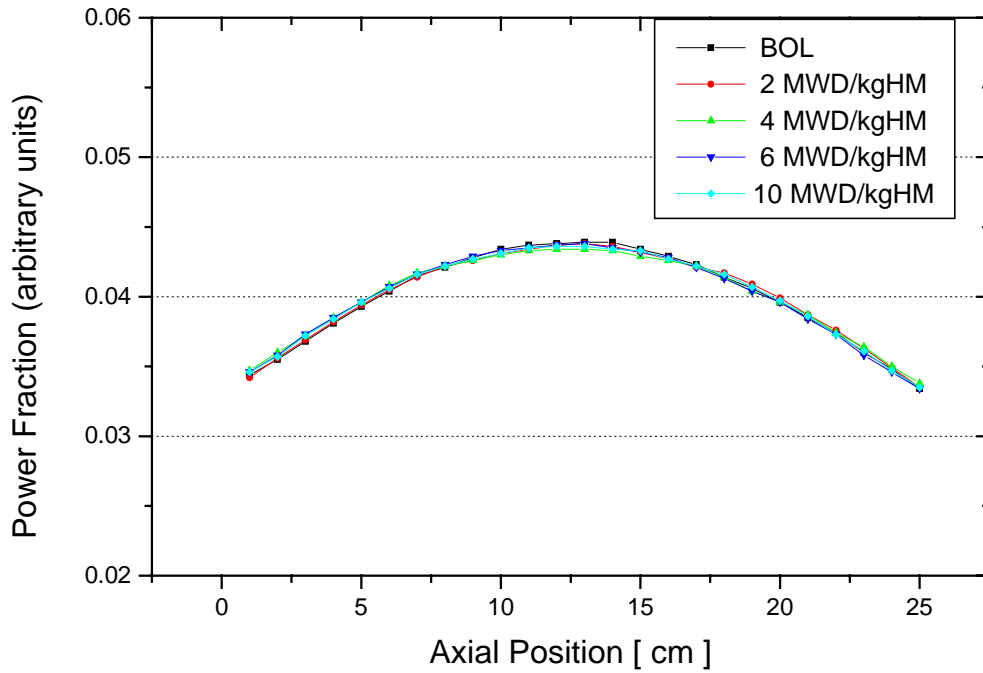


Figure 21: Axial Power Shape.

From the figure it is clear the power shape is very slightly biased towards the core bottom; this is because the neutron streaming through the coolant channels is retarded by the liquid sodium at the core inlet, however, the sodium vapor at the core outlet allows neutrons to leak through the coolant channels more easily. While noting the reason for this shift, its overall effect is negligible. The power shape, additionally, does not change with burnup. The axial power peaking factor is 1.10.

The sodium density is plotted in Figure 22. The sodium density varies dramatically from the core inlet to the core outlet; however, this variation has little effect on the axial power shape, which retains the expected chopped cosine shape.

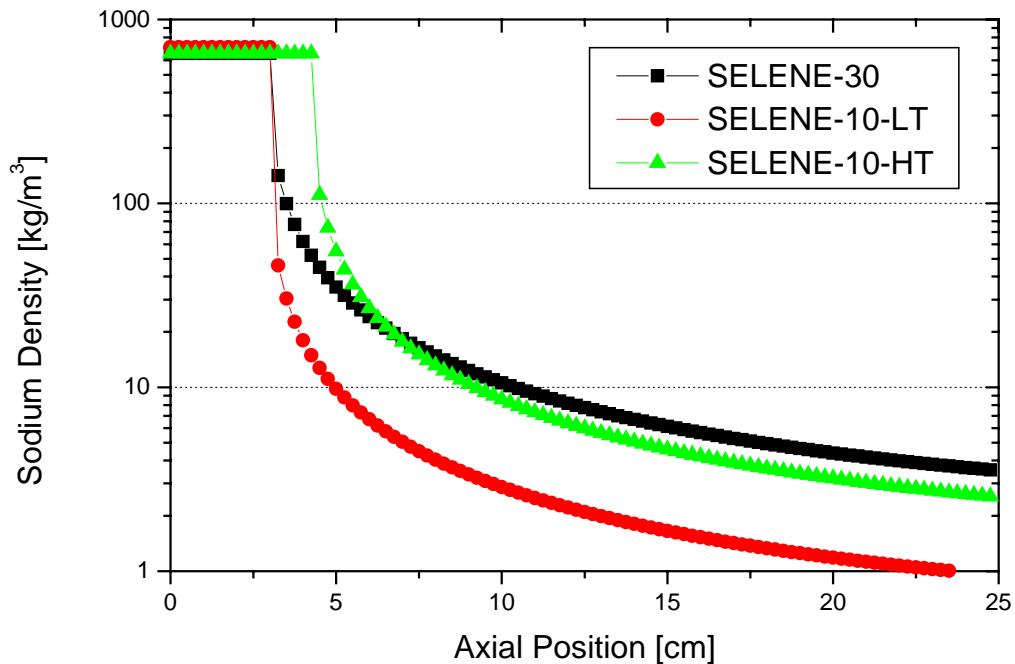


Figure 22: Variation of the Sodium Density with Axial Position.

Note the log scale on the sodium density axis of the plot in Figure 22. The sodium density is reduced by a full decade near the onset of boiling at 5 – 7 cm. The sodium density is further reduced by another decade by 10 cm, and finally at the core outlet is approximately 1/300 – 1/750 the density at the core inlet.

Given the dramatic change in sodium density, the center peaked axial power shape, the very small radial power peaking factor, and the general similarity in sodium density in each case, the same power profile is assumed for all of the designs to conduct nominal operation calculations. When analyses are done for reactivity-power coefficients the sodium profile for SELENE-30 under nominal and accident conditions is included to calculate accurate reactivity feedback coefficients.

The radial power peaking factor was calculating using a midplane two-dimensional model. The plane is comprised on small unit cells and the power density in 9 cells was tracked compared to the average of the remaining cells. The center cell, the corner cells (4), and the cells on the core edge between the corner cells (4). An initial trial was run with a uniform enrichment of 93 a/o. The power was dramatically peaked towards the cells at the periphery of the core near the BeO reflector. The neutron spectrum is significantly softer in these regions, and thus the fission cross section of ^{235}U is dramatically higher for these cells. Table XII summarizes the ratio of the cell power density to the average power density. The power density, though quoted in kW/cc is an arbitrary figure because the model height is nominally 1 cm with axial reflective boundary conditions.

Table XII: Radial Peaking for Uniform Enrichment.

Cell Location	Power Density [kW/cc]	Cell / Average
Center	12.18	0.97
Corner	81.38	6.48
Face	80.28	6.40
Average	12.55	1.00

The results show that the center cell is very near the average, indicating that the power peaking is localized at the first few cells near the radial reflector. To reduce the radial power peaking factor, the enrichment was zoned into an inner and outer core. In the inner core enrichment was increased to 97 a/o enrichment from the baseline configuration. The outer two rows of coolant channels are loaded with 70 a/o enriched fuel. Since the power peaking is most egregious in the corner, the corner power density is tallied and compared with the average power density.

A full core model was created with 6 fuel zones. There are 2 radial zones (inner and outer core) for 3 separate axial zones. This is done so that the sodium density variation can be included in the calculation. The radial power peaking factor is then calculated by taking the axial average of the inner and outer zone power densities and comparing that with the average in a single cell at the corner of the core at the periphery. The new core configuration is summarized in Figure 23.

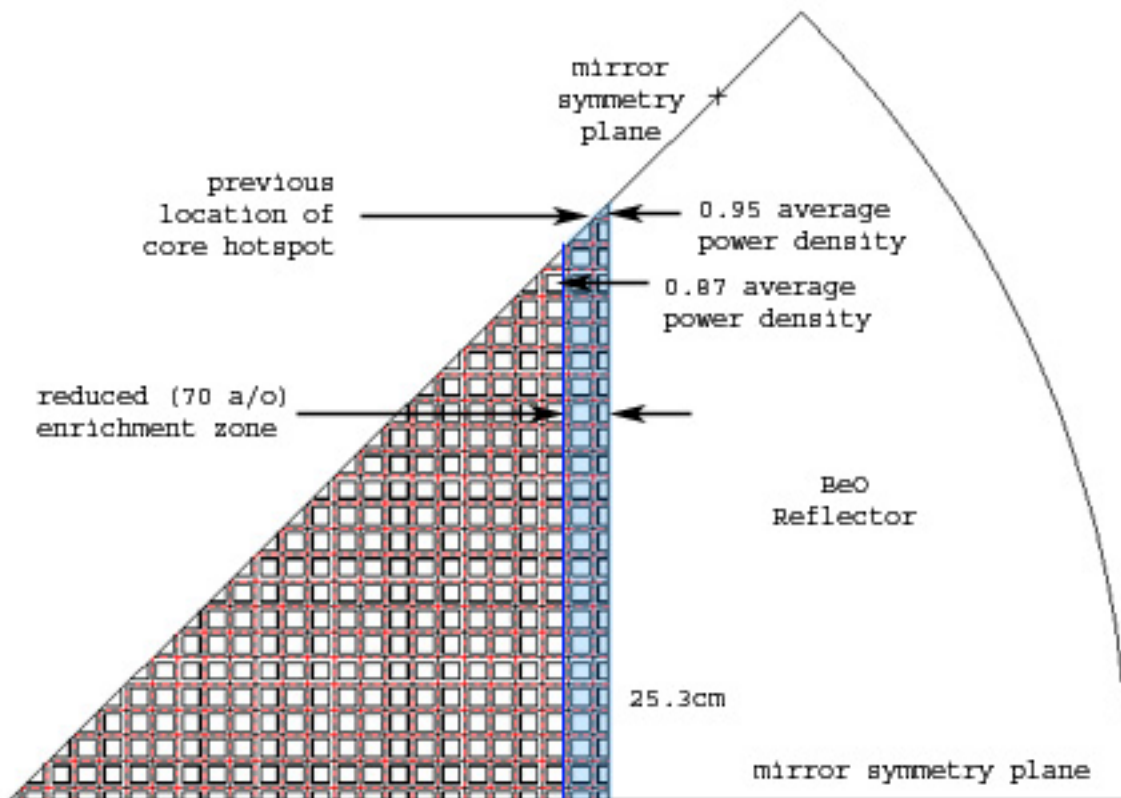


Figure 23: Zoned Full Core Radial Slice

The radial power peaking factor, noting that the inner fuel zone power shape is very flat, is merely the ratio of the maximum power density in any zone to the average. Table XIII summarizes the results of the power density comparison to calculate the radial power peaking factor. The inner and outer corners refer to the cells labeled in Figure 23. The inner corner cell was tallied to ensure that the low enrichment zone was sufficiently large to shield the inner fuel zone from thermal return current from the reflector.

Table XIII: Radial Power Peaking in the Zoned Core.

Zone Location	Power Density [kW/cc]	Zone / Average
Inner Zone	1.194	1.03
Outer Zone	0.983	0.85
Outer Corner	1.099	0.95
Inner Corner	1.004	0.87
Center	1.164	1.01
Average	1.158	1.00

The results of Table XIII show that the radial power peaking factor is 1.03. To add conservatism to the calculations, values of 1.10 and 1.30 will be used in the hot channel analysis for comparison.

The variation of the radial power during burnup was also investigated. The plot in Figure 24 shows the variation in local power density with burnup. The plot clearly shows that the power shape is holding roughly constant during burnup.

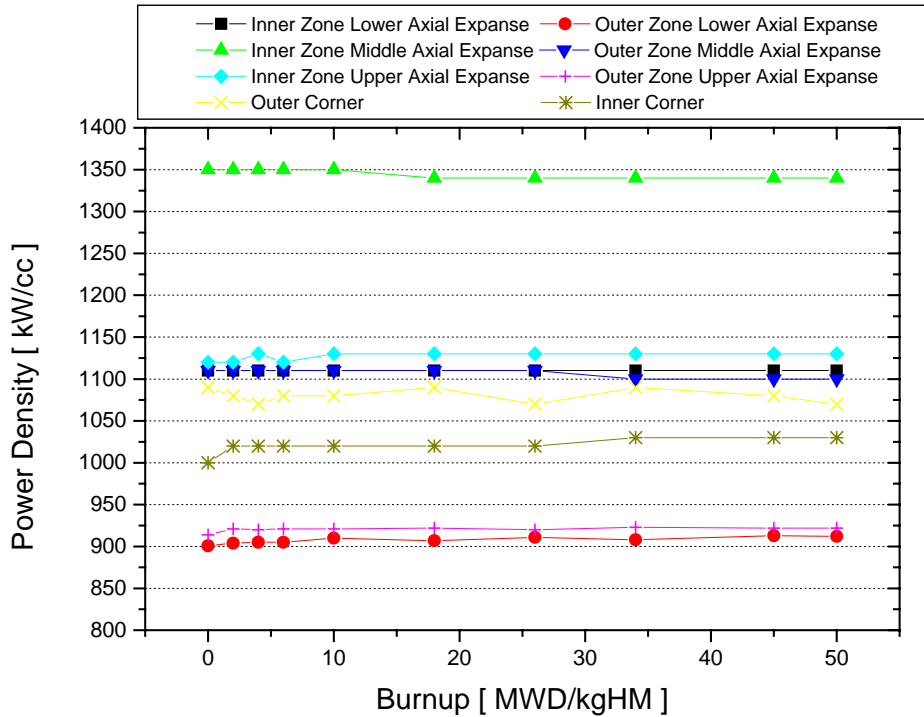


Figure 24: Radial Power Density Variation

Though the cube reactor is known for high power peaking factors, the SELENE core is unique given its very small size, hard neutron spectrum, and moderating reflector. The small size (hence large geometric buckling), coupled with the large migration length of fast neutrons means that the reactor has a flat power shape. Additionally, the graded enrichment with the moderating reflector flattens the power near the corners of the core because the enrichment and spectral shift are balanced in terms of their contribution to the fission cross section in the areas where peaking would otherwise be most egregious.

10.4 Fuel Swelling and Fission Gas

A correlation was used to predict the fuel swelling at high temperature to determine the smear density of the fuel in the plates. The correlation is given in Equation 56 for fuel temperatures less than 1900 K [Oggianu, et al.].

$$\frac{3\Delta D}{D_F} \frac{1}{Bu} = 1 \quad (56)$$

where D is the fuel dimension, and
Bu is the burnup in atom fraction.

For a target burnup of 4.3 a/o, assuming rectilinear geometry, the fuel will swell by approximately 9%. Therefore the smear density of 85% is conservative, as the SELENE-10 cores will not likely reach such high burnup. For the SELENE-30 core, the margin for fuel swelling is reduced and the smear density is taken at 90% of the theoretical density.

While the effects of fuel swelling from fission gas production may be predicted, the fuel design must additionally accommodate for the accumulation of fission gas in the fuel plates outside of the fuel itself. Proposed solutions include absorbing carbon buffers or plena at the top and bottom of the fuel plates in the core. A more detailed analysis will need to be carried out, particularly to assess the transport and absorption of fission gas through the fuel, bond material, and any buffer under high temperature conditions in micro-gravity. Depending on the surface tension of the bond, if a liquid bond such as lead is used, the behavior of fission gas will differ.

11.0 Hot Channel Analysis

Analysis was done of the hot channel of the reactor to ensure that fuel melting would not occur under steady state conditions. This analysis was performed using approximately the same procedure as calculating the fuel temperature for the average channel for each of the proposed designs.

The primary difference between the hot channel analysis and the average channel analysis is the iteration technique. In the case of the average channel, the core exit quality, and radiator heat rejection were used to calculate the core mass flow rate, which in turn was fed back into the calculation to compute a new core exit quality. In the hot channel analysis, the iteration parameter is not the mass flow rate. The hot channel and the average channel share the same pressure drop.

In each case the average channel pressure drop was calculated. Each channel in the core will have the same pressure drop as the flow in each channel adjusts to meet the driving pressure force and the given flow resistance in each channel.

The approach for calculating the hot channel fuel temperature is to multiply the cell power by the radial power peaking factor for every cell. Recall that the axial power shape is already an input to the average channel calculation. The mass flow rate is set to a specific value starting with the average channel mass flow rate and the pressure drop across the channel is calculated. The mass flow rate is reduced until the channel pressure drop matches the pressure drop as calculated for the average channel. The highest fuel temperature is calculated in the same manner as before and compared with the melting temperature for UC (2575 K [Matzke]). Table XIV summarizes the results of these calculations quoting the hot channel mass flow rate and peak fuel temperature for the SELENE-30 design.

Table XIV: Hot Channel Results for Various Radial Power Peaking Factors.

Radial Power Peaking Factor	Peak Fuel Temperature	Core Pressure Drop	Channel Mass Flow Rate	Outlet Velocity	Exit Quality
	[K]	[bar]	[g/s]	[m/s]	
1.00	1606	0.4309	4.800	99.6	0.696
1.03	1604	0.4308	4.635	103.4	0.748
1.10	1600	0.4311	4.311	111.9	0.873
1.30	1834	0.4260	3.976	133.5	> 1

The SELENE-30 design is the most demanding in that it has the highest fuel temperature and sodium velocity of the three proposed. If the SELENE-30 hot channel indicates a fuel temperature well below the melting temperature of UC, then the other two designs will also be within the design envelope. SELENE-30 is the only design also to be evaluated under over-power conditions because the other designs are more conservative.

The peak fuel temperature decreases with radial power peaking factor slightly until the coolant becomes superheated. The reason being that nucleate boiling heat transfer was neglected and only convection was considered. This was assumed to be a valid assumption because of the very rapid decrease in the sodium density with axial position after the onset of boiling. However, for small values of the radial power peaking factor, the increased velocity improves the convection and keeps the peak fuel temperature very near the nominal value of 1600 K even though the opposite effect (though similarly small) would be expected because of the nucleate boiling heat transfer. Only when

the coolant reaches superheated conditions near the outlet does the peak fuel temperature increase significantly.

The calculations are performed by iterating the mass flow rate until the pressure drop is within a certain error tolerance from the average channel pressure drop. In the case of low power peaking factor, very tight error tolerances were held. Though the pressure drop should be the same in each case, there is a noticeable error for the large power peaking factor of 1.3. Since the sodium becomes superheated in this channel, the equations do not converge well on account of there being three sets of equations necessary to calculate the fuel temperature. Therefore the error tolerance on the pressure drop was relaxed as shown in the table for the result to converge. Since the calculated pressure drop is slightly lower than the nominal, the actual mass flow rate will be slightly higher than calculated here and the fuel temperature (1834 K) is conservative. Associated plots from the thermal hydraulic model for the 1.3 power peaking factor are located in Appendix D of this thesis.

The results indicate that even for a radial power peaking factor that is much higher than the calculated value, and even under conditions where the sodium reaches superheat, the fuel is still maintained below the melting temperature. The goal is to keep the temperature below 1900 K. Above 1900 K the swelling rate increases dramatically, and if operating at this temperature for extended periods, the fuel could potentially swell to the point of failing the clad or deforming the coolant channel geometry.

Under accident conditions the fuel should remain below 2500 K, and under steady state conditions the fuel should remain below 1900 K. The results from the hot channel analysis indicate that while under steady state conditions, even if the power peaking were larger than indicated by the calculations, the fuel would still be below 1900 K, this is the case even when the sodium coolant becomes superheated to a certain extent.

12.0 Overpower Condition and Reactivity Feedback

The overpower condition is evaluated to check the power feedback coefficient for the core. The core thermal power is increased by 18%. This may be the case for a small, rapid reactivity insertion. The thermal hydraulic model is used to predict the new fuel temperature and sodium properties.

The new fuel temperature is used to predict the thermal expansion of the fuel. Given the thermal expansion, the mass is maintained constant in the reactor physics model, and the density as well as model geometry is changed to reflect the increased fuel size. Additionally, the sodium density at the core outlet will be reduced, and though this has a small contribution to the physics of the core, as shown during the axial power profile calculation, this effect is also included in the overpower condition model. The core reactivity is calculated using MCNP4c2. The results are compared with the nominal core reactivity. The reactivity is affected by three physical processes, which are discussed in the following sections.

The fuel temperature predicted from the thermal hydraulic model is used to predict the fuel thermal expansion in order to determine the change in core size as a result of an accident leading to an 18% overpower event. The thermal expansion dilation of UC is given by the formula shown in Equation 57 [Stahl, et al.]. This formula is accurate between temperatures of 300 – 1700 K.

$$\frac{\Delta L}{L_0} = -3.22 \times 10^{-3} + (9.71 \times 10^{-6})T + (1.4 \times 10^{-9})T^2 \quad (57)$$

where, L refers to the UC element dimension.

The volume of the fuel element is given by the dimension cubed, therefore, the volume change can be calculated and the density can be adjusted to maintain the same mass as shown in Equation 58.

$$\begin{aligned} M &= d_0 (L_1 L_2 L_3) = d' (L_1' L_2' L_3') \\ L_i' &= L_i + \Delta L_i = L_i \left(1 + \frac{\Delta L}{L_0} \right) \\ d' &= d_0 \frac{(L_1 L_2 L_3)}{L_1 \left(1 + \frac{\Delta L}{L_0} \right) L_2 \left(1 + \frac{\Delta L}{L_0} \right) L_3 \left(1 + \frac{\Delta L}{L_0} \right)} = d_0 \frac{1}{\left(1 + \frac{\Delta L}{L_0} \right)^3} \end{aligned} \quad (58)$$

where, L_i refers to one of the three dimensions of the UC element,
M is the mass of fuel in an element,
 d_0 is the nominal density,
 d' is the expanded density, and
 L_i' is the expanded dimension.

The fuel temperature nominally is 1600 K; with an 18% overpower accident, the fuel temperature reaches 1620 K. Though possible to measure and compute the fuel thermal expansion under these conditions, the change in fuel dimensions is only 0.03% and the density is 99.9% of the nominal value. Therefore, the affects of sodium density and temperature are calculated without changing the dimensions of the core. Overall, the thermal expansion calculation is meant to show that the thermal expansion from the nominal condition to the 18% overpower accident condition will contribute a

negligible reactivity affect. However, this model may be used for the analysis of accidents where the fuel temperature increases more dramatically, or doing analyses of the reactor startup.

SELENE-30 is designed to have a zero-reactivity change after a sudden increase in power. Although most hard spectrum reactors have positive void coefficient, SELENE-30 has a void coefficient of essentially zero. The physical processes that contribute to the void coefficient are described below.

12.1 Spectrum Hardening

The overpower accident will cause more sodium to boil, and thus the core will have a higher void fraction. It is common in hard spectrum reactors for coolant void to increase the core reactivity. The coolant in all reactors contributes to neutron moderation and parasitic absorption. In hard spectrum reactors, the coolant spectrum averaged absorption cross section is small, and in most cases the absorption effect is negligible.

When coolant voiding occurs, the neutrons are not moderated by the coolant, and thereby the core neutron spectrum hardens. As the spectrum hardens, the fast capture cross section for the fissile species declines relative to a flat, or even increasing fission cross section, thus adding reactivity.

The flux spectra are very similar between the two cases, so the ratio of the flux spectra is taken to illustrate the slight hardening effect. The relative spectrum is plotted in Figure 24. The ratio is computed by finding the normalized flux spectrum per unit lethargy in each case, since the energy division is the same between the two cases, the ratio is calculated directly by taking the ratio of the normalized flux per unit lethargy for each energy. The upward trend of the curve shown in Figure 25 clearly illustrates that the sodium voiding results in a slightly harder neutron spectrum.

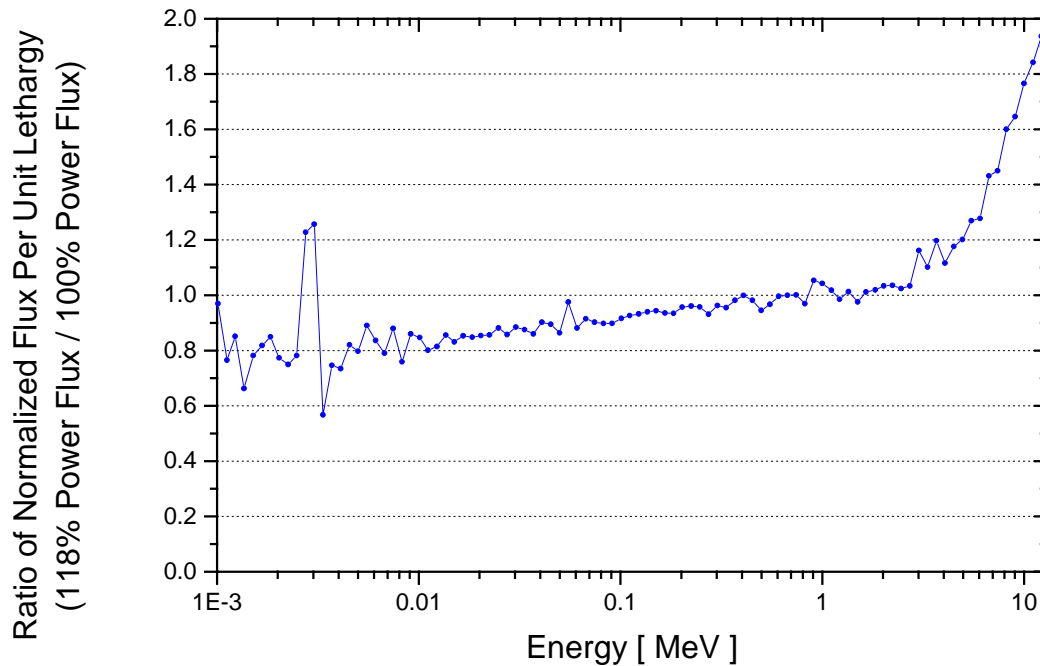


Figure 25: Ratio of Flux Spectra to Illustrate Spectrum Hardening

The neutron collisions that occur in the coolant affect the flux spectrum, but the coolant also prevents the neutrons from streaming through the coolant channels. To approximately calculate the reactivity affect of spectrum hardening alone, the sodium density was smeared axially along the coolant channels in the core model. The sodium is uniform axially and radially and taken as the average predicted by the thermal hydraulics model.

Since the coolant is uniform, comparing the nominal and overpower cases on this basis removes any large differences based on leakage as a result of axial neutron streaming. The uniform sodium density under nominal power conditions has a BOL core eigenvalue of 1.080(78) and the overpower uniform sodium case has a BOL core eigenvalue of 1.081(22) yielding a reactivity difference of +0.0004 or a positive reactivity worth of \$0.06 (the delayed neutron fraction is calculated to be 0.0065 by removing delayed neutron cross sections from the MCNP4c2 model and calculating the reactivity worth of the delayed neutrons based on the difference in core eigenvalues).

12.2 Leakage

The spectrum hardening calculation specifically removes significant changes as a result of the neutron streaming. The sodium density is dramatically different at the top and bottom of the core, and the dense sodium at the bottom of the core shifts the power distribution somewhat towards the bottom of the core.

The power shift as shown in Figure 21 results primarily from the neutron streaming that occurs at the top of the core. There is significant neutron scattering in the dense liquid sodium at the bottom of the core, thus impeding neutron streaming through the bottom. The sodium density gradient is included in the full core model by having three axial zones in the core and averaging the nominal condition and overpower condition sodium density in these three regions.

Compared with the nominal and overpower uniform density cases, the core eigenvalue is higher. The eigenvalue is increased because the high sodium density in the base of the core significantly impedes axial neutron streaming at the base, thus reducing the core leakage. When the power increases, more sodium boils and while increasing the void hardens the spectrum and increases the reactivity, as the boiling length is reduced, the axial leakage at the bottom of the core also increases. SELENE-30 is designed such that these two affects together will yield a zero-reactivity change.

The overpower and nominal core conditions are compared based on eigenvalue to determine the actual change in reactivity resulting from the voiding. The nominal core eigenvalue is 1.084(40) and the overpower core eigenvalue is 1.084(48). These eigenvalues are essentially exactly the same. Thus, while it has been shown that the spectrum hardening contributes positive reactivity, the increased neutron leakage exactly compensates with a negative reactivity contribution.

The previous calculation assumes that the sodium flow has not stopped. As analyzed in the homogenous core calculation, sodium voiding with sequestered liquid in the reflector regions will increase the reactivity.

12.3 Doppler Feedback

For an 18% overpower condition, the fuel peak temperature increases by 20K; the contribution of Doppler broadening is smaller than the error in the calculation, however, the Doppler reactivity coefficient was calculated by increasing the fuel temperature dramatically (to 3200 K) in the model. The core eigenvalue was recalculated for the nominal and very high temperature cases with 10 times more neutron histories to reduce the error by a factor of roughly three.

The core reactivity is calculated based on the two eigenvalues, and the Doppler reactivity coefficient is approximated as the ratio of the reactivity difference to the temperature difference. The Doppler reactivity contribution can then be calculated for any case by multiplying the Doppler reactivity coefficient by the temperature difference from the nominal case. In any case, the measures noted for reducing the error in calculations in order to calculate the Doppler reactivity indicate that the contribution will be very small in either direction; this is because of the very high enrichment.

Table XV summarizes the results of the calculation. The calculation at first seems to indicate that the Doppler reactivity coefficient is negative. However, even with the dramatic temperature difference of 1600 K from the nominal case, the difference in the core eigenvalues is still on the order of one standard deviation, therefore one cannot even confidently report the nature of the Doppler reactivity coefficient.

Table XV: Doppler Reactivity Coefficient Data

Temperature	Core Eigenvalue	Standard Deviation
[K]		
1600	1.08103	0.00022
3200	1.08080	0.00021

The Doppler reactivity coefficient was calculated based on the average core eigenvalues, despite the fact that the errors are larger than the difference between them, and is $-2 \times 10^{-5} / \text{K}$. What can be said with confidence, however, is that the Doppler reactivity coefficient for the core will be on the order of millicents and therefore will not have a significant impact during any transients.

The Doppler reactivity coefficient is small due to the hardness of the neutron spectrum and the very high enrichment. The neutron spectrum is fast and Figure 20 indicates that a large portion of the neutron population is above the resonance region and in the continuum regime. In the continuum regime the resonances are so close together that broadening does not have any substantial affect.

The fuel enrichment is highest in the inner zone of the core; however, this is also where the portion of the neutron spectrum in the resonance range is smallest. In the outer zone, the enrichment is lower, hence there is more fertile absorber material, and there is a softer tail to the neutron flux because of the return neutron current from the reflector. In the outer zone, as the temperature increases, absorption resonances in fertile isotopes, fuel constituents, and the fissile isotopes will all broaden. In the case of SELENE-30 the negative contribution from parasitic resonant absorption broadening effectively cancels the positive reactivity contribution from fissile resonant absorption broadening.

13.0 Launch Accidents

Several areas are candidates for future work, in particular the results of launch accidents. Though the SELENE concept has been largely specified in terms of core and systems design, the exact arrangement of systems, and launch vehicle are not as certain. To this extent, since a whole design picture will be necessary for accident analysis, discussion of potential launch accidents is primarily qualitative. Though in instances referring to core behavior quantitative assessments may be made.

The reactor will not be operational until SELENE is in a Nuclear Safe Orbit (NSO) around the Earth. Therefore, the fuel contains no fission products prior to reaching NSO. In the event of a catastrophic launch accident in the atmosphere or on the surface, since the uranium mass is quite small, it is unlikely that there is a significant radiological or environmental concern with dispersing the material.

One of the primary concerns with the reactor system is a potential launch accident where the system becomes immersed in water. Firstly, the sodium reactor coolant has a violent chemical reaction with water, and secondly, if water penetrates the primary system, and the reactor is not disassembled by the chemical reaction, there is a potential criticality concern when the reactor is submerged in water. Each of these concerns will be briefly addressed.

13.1 Sodium Reaction with Water

The SELENE system should be hermetically sealed to prevent sodium reaction with the environment in the event of a launch accident. In the event of a water immersion, if the primary coolant is exposed to the water, the sodium will very rapidly oxidize. The oxidation will release a large amount of energy and most likely cause the SELENE to disassemble. We can calculate the energy released from the sodium oxidization assuming that the entire inventory of sodium is oxidized.

The reaction is very rapid, so one can assume that this energy is produced almost instantaneously. The violent oxidation reaction is also associated with an increase in volume and the production of hydrogen gas. The mass of the sodium in the entire system is not known, but assuming a density of 1 g/cc under launch conditions, and assuming we are only interested in the energy released from the sodium that inhabits the coolant channels in the core we can approximate the initial mass of sodium reactant of interest to be approximately 10 kg. As the sodium may be solid during launch conditions, the reaction may not be quite as rapid because water will interact at the exposed surface of the solid sodium.

Neglecting the explosive potential of the hydrogen gas produced by the sodium-water reaction, we can calculate the energy released by the reaction of the sodium inventory in the core with water. The chemical equation and enthalpy change are shown in Equation 59 [Kottowski].



where, ΔH is the enthalpy change per mole of sodium reacted.

Assuming that the entire inventory of sodium reacts rapidly, which may not be a reasonable assumption depending on the type of accident and system configuration, the total energy released by oxidation alone is 82,000 kJ. This amount of energy being deposited in the core in a very short time will be sufficient to cause significant structural damage and probably disassemble the core. Though this is a substantial amount of energy, the analysis does not include the damage that will be caused by the rapid expansion of the inventory in the core, nor does it include the explosive potential of the hydrogen gas released.

The next section will discuss the consequences of water immersion if the sodium coolant can be evacuated from the system prior to water immersion. However, this is a very unlikely scenario, particularly because the sodium may be in the solid state when launched. It is an interesting safety case to make that perhaps the reaction between sodium and water will prevent the potentiality of reactor super-criticality under water.

13.2 Water Moderation and Criticality

In the case of the sodium-cooled system, water flooding and criticality is not the primary concern. Since the core may be used with another coolant, though the system performance will most likely be greatly degraded compared with the sodium coolant, it is worthwhile to examine the reactor response to water flooding. The SELENE core is similar to variants that have been analyzed with a variety of different reactor coolants. The MSFR core for example, which the SELENE core is based on, was analyzed with lithium and molten salt coolants [Dostal, et al.].

Assuming a hypothetical, worst-case launch accident where the SELENE-30 core is voided of sodium, submerged in water, and separated from the BeO reflector (and consequently ex-core control mechanisms), one can calculate the resultant reactivity using the full core model by replacing the sodium coolant and BeO radial reflector with water and increasing the reflector dimensions significantly (to a radius of 250 cm).

The eigenvalue of the worst-case water submersion case is 1.294(2). This is far supercritical and not entirely unexpected given that the fuel, highly enriched uranium, is submerged in an effectively infinite moderator, water. However, it is unclear how the core could be voided of the sodium coolant before being submerged in water, especially if the coolant is solid at the time of launch.

14.0 Conclusions and Recommended Future Work

The SELENE system is a transformational high power space reactor system. SELENE can be scaled from 1 to 2.6 MWe with minor design changes. Therefore, low power SELENE variants can be used to test the technology and materials under less demanding conditions than the SELENE-30.

The core is a rectangular honeycomb grid of UC fuel plates clad with Nb-1Zr cladding. The fuel is in two zones, the inner zone is 97 a/o enriched while the outer zone is 70 a/o enriched to flatten the radial power profile. The power would otherwise be peaked towards the BeO reflector, which softens the neutron spectrum significantly near the core periphery.

The SELENE core power profile is very flat with an axial power peaking factor of only 1.1 and a radial power peaking factor of 1.03, due to the large migration length and leakage as well as the graded enrichment strategy. The power shape remains constant during burnup and the SELENE is designed for roughly 9 months of EFPL.

One could reconfigure the core to increase the reactivity limited burnup either by increasing the size of the reactor, or by reconfiguring the geometry to reduce the surface area to volume ratio. The SELENE core is specifically designed to have a large surface area to volume ratio to increase leakage and hence the worth of the radial reflector, and hence have a much larger control margin with ex-core control drums. If it is acceptable to reduce this margin, reconfiguring the core geometry into a more cylindrical shape may prove advantageous.

The core is cooled with boiling sodium that is also the working fluid in a direct Rankine power conversion unit. The Rankine cycle was selected above other competing technologies because the quasi-isothermal heat rejection in the cold leg of the cycle maximizes the usefulness of the limited radiator surface area. The direct Rankine cycle is also advantageous from the standpoint of the reactor physics because it allows for a zero reactivity-power coefficient as leakage and spectrum hardening affects may be balanced to yield a zero net change in core reactivity at higher power levels.

The system is safe in that there are no positive reactivity feedback mechanisms with reactor power during operation and while water submersion during a potential launch accident remains a reactivity concern, it is highly likely that the energetic sodium-water reaction in the core would ensure a subcritical configuration.

The purpose for designing the core to have a zero reactivity-power coefficient is to simultaneously meet the requirement that the system can be scaled to higher power (by approximately a factor of 3) and still be safe in the event of an accident. As was shown, the core will not suffer damage by operating under accident conditions at higher thermal power levels, on the order of 20 – 30% higher. The reactivity-power coefficient can be made slightly negative by pancaking the core somewhat. The improved neutron streaming during overpower conditions contributes to higher neutron leakage, and hence negative reactivity feedback. However, the scalability of the system is impeded by such a design change.

Though the core thermal hydraulic analysis and reactor physics calculations have been completed, and the core examined under some accident conditions, there is a body of recommended future work on this design.

The fuel bond material has yet to be selected, and while lead may be promising, it is certainly not the only alternative. The density variation upon expansion and melting may overcomplicate the fuel design. A solid, porous carbon buffer may be an interesting alternative because it will also act as an absorber for fission gas. Neither alternative can be ruled out as of yet.

In the area of system architecture, the sodium turbine has yet to be designed. Additionally, the main coolant piping architecture has not been completely specified either. For a more accurate analysis of the system performance, pressure losses through the piping system ought to be accounted for and the exact efficiency of the turbine must be calculated. The reliability of the system and lifetime of the system also hinge on the design of the turbine.

The next design iteration of the SELENE must also account for a series of performance goals other than those considered here. While liquid metal is considered for the reactor coolant because of the heat removal properties, and sodium in particular for a host of other reasons (including low density), the initial reactor startup is going to be a very complicated procedure. The coolant will most likely require some form of electrical heating elements to remelt the coolant after the reactor has reached a NSO. Regardless of the system employed to assure the coolant will be in liquid form during startup; a more complete set of system specifications will be required to carry out the associated transient modeling of the reactor startup. While the steady state analyses indicate favorable performance of the SELENE, the practicality of reactor startup and transient response will weigh heavily on the applicability of this technology.

Also, automatic on-board control systems must be developed, particularly if the reactor is being used for an unmanned mission. During unmanned missions to Mars, the reaction delay time between controllers on Earth and the reactor (in Martian orbit) will be nine minutes on average [Dostal, et al.], hence all short-term control action must be automatic or based on inherent feedback mechanisms.

15.0 References

1. Chen, J.C. 'A proposed mechanism and method of correlation for convective boiling heat transfer with liquid metals'. Paper presented at the 3rd Annual Conference on High Temperature Liquid Metal Heat Transfer Technology, ORNL, Sept. (1963). Also BNL 7319.
2. Deickamp, H.: Nuclear Space Power systems, Atomics International. Canoga Park, CA 1967.
3. Dostal, V., Gezelius, K., Horng, J., Koser, J., Palaia, J., Shwageraus, E., Yarsky, P.: "Mission to Mars: How to get people there and back with Nuclear Energy" MIT-NSA-TR-001, 2003.
4. Driscoll, M.J., Downar, T.J., Pilat, E.E.: The Linear Reactivity Model for Nuclear Fuel Management. American Nuclear Society. La Grange Park, IL 1990.
5. Eisberg, R, Resnick, R.: Quantum Physics of Atoms, Molecules, Solids, Nuclei, and Particles, 2nd Ed. John Wiley & Sons, Inc. New York, NY 1985.
6. Fan, J., Boyd, I., Shelton, C. 'Monte Carlo Modeling of YBCO Vapor Deposition' AIP Conference Proceedings Vol. 585 pp.214-221, August 2001.
7. Fink, J.K., Liebowitz, L. report ANL/RE-95/2 (1995).
8. Fitzpatrick, G.O., Allen, D.T. "Cascaded Thermionic Converters" *Nuclear Power Engineering in Space*, Conference Proceedings, 2 (Oct 1991)
9. Hodgman, C. ed.: Handbook of Chemistry and Physics, 44th ed. Chemical Rubber Publishing Company. Cleveland, OH 1962.
10. Kottowski, H.M., ed.: Safety Problems Related to Sodium Handling in Liquid Metal Fast Breeder Reactors and Large Test Facilities. Hartwood Academic Publishing. New York, NY 1981.
11. Lewis, H., Kerrisk, J., report LA-6096-MS (1975).
12. Matzke, H.J., Science of Advanced LMFBR Fuels, North-Holland, (1986)
13. National Technical University of Athens – Nuclear Engineering Section – Thermodynamic and Transport Properties of Sodium Liquid Metal Saturation States. NTUA. 2004.
< <http://arcas.nuclear.ntua.gr/codes/sodium.html> >
14. Oggianu, S.M., Kazimi, M.S.: "A Review of Properties of Advanced Nuclear Fuels" MIT-NFC-TR-021, 2000.
15. Parrington, J., Knox, H. , Brenneman, S., Baum, E., and Feiner, F. eds. Chart of the Nuclides, 15th Ed rev. 1996. Knolls Atomic Power Laboratory. Schenectady, NY
16. Stahl, D., Strasser, A., in Carbides in Nuclear Energy, ed. L.E. Russel, B.T. Bradbury, J.D.L. Harrison, H.J. Hedger, P.G. Mardon, MacMillan, London (1964).
17. Todreas, N., Kazimi, M.: Nuclear Systems I Thermal Hydraulic Fundamentals, Taylor and Francis. New York, NY 1993.
18. Valota, L. 'Microgravity Flow Regime Identification Using Void Fraction Signals' Paper presented at the ANS Student Conference, University of Wisconsin at Madison, April 2004.
19. Zinov'ev, V. E.: Handbook of Thermophysical Properties of Metals at High Temperature, Nova Science Publishers. New York, NY 1996.

This Page Left Intentionally Blank.

16.0 Appendices

Appendix A: MCNP4c2 SELENE-30 input deck.

Appendix B: MCODE SELENE-10-HT input deck

Appendix C: SELENE-30 Average Channel Thermal Hydraulic Data

Appendix D: SELENE-30 1.3PPF Hot Channel Thermal Hydraulic Data

16.1 Appendix A: SELENE-30 MCNP4c2 Input Deck

```
c Full Core Model (5 axial zones)
c
c Pete Yarsky
c 4.15.04
c 1/8 core symmetric model
c
c cell specification
c
21      1 -3.01
        -14 +13 u=21 tmp=1.38e-7 imp:n=1 $BeO Axial Lower
22      2 -8.4
        -13 +12 u=21 tmp=1.38e-7 imp:n=1 $Nb cladding
23      3 -0.08866
        -12 u=21 tmp=1.38e-7 imp:n=1 $Sodium coolant
24      1 -3.01
        -14 +13 u=22 tmp=1.38e-7 imp:n=1 $BeO Axial Upper
25      2 -8.4
        -13 +12 u=22 tmp=1.38e-7 imp:n=1 $Nb cladding
26      3 -0.08866
        -12 u=22 tmp=1.38e-7 imp:n=1 $Sodium coolant
1011    101 6.20037e-02
        -14 +13 u=11 tmp=1.38e-7 imp:n=1 vol=2175.81 $UC fuel
1012    2 -8.4
        -13 +12 u=11 tmp=1.38e-7 imp:n=1 $Nb cladding
1013    3 -0.08866
        -12 u=11 tmp=1.38e-7 imp:n=1 $Sodium coolant
1021    102 6.20037e-02
        -14 +13 u=12 tmp=1.38e-7 imp:n=1 vol=445.267 $UC fuel
1022    2 -8.4
        -13 +12 u=12 tmp=1.38e-7 imp:n=1 $Nb cladding
1023    3 -0.08866
        -12 u=12 tmp=1.38e-7 imp:n=1 $Sodium coolant
1031    103 6.20037e-02
        -14 +13 u=13 tmp=1.38e-7 imp:n=1 vol=2175.81 $UC fuel
1032    2 -8.4
        -13 +12 u=13 tmp=1.38e-7 imp:n=1 $Nb cladding
1033    3 -0.08866
        -12 u=13 tmp=1.38e-7 imp:n=1 $Sodium coolant
1041    104 6.20037e-02
        -14 +13 u=14 tmp=1.38e-7 imp:n=1 vol=445.267 $UC fuel
1042    2 -8.4
        -13 +12 u=14 tmp=1.38e-7 imp:n=1 $Nb cladding
1043    3 -0.08866
        -12 u=14 tmp=1.38e-7 imp:n=1 $Sodium coolant
1051    105 6.20037e-02
        -14 +13 u=15 tmp=1.38e-7 imp:n=1 vol=2175.81 $UC fuel
1052    2 -8.4
        -13 +12 u=15 tmp=1.38e-7 imp:n=1 $Nb cladding
1053    3 -0.08866
        -12 u=15 tmp=1.38e-7 imp:n=1 $Sodium coolant
1061    106 6.20037e-02
        -14 +13 u=16 tmp=1.38e-7 imp:n=1 vol=445.267 $UC fuel
1062    2 -8.4
        -13 +12 u=16 tmp=1.38e-7 imp:n=1 $Nb cladding
1063    3 -0.08866
        -12 u=16 tmp=1.38e-7 imp:n=1 $Sodium coolant
1071    107 6.20037e-02
        -14 +13 u=17 tmp=1.38e-7 imp:n=1 vol=15.53226 $UC fuel
1072    2 -8.4
        -13 +12 u=17 tmp=1.38e-7 imp:n=1 $Nb cladding
1073    3 -0.08866
        -12 u=17 tmp=1.38e-7 imp:n=1 $Sodium coolant
1081    108 6.20037e-02
        -14 +13 u=18 tmp=1.38e-7 imp:n=1 vol=15.53226 $UC fuel
1082    2 -8.4
        -13 +12 u=18 tmp=1.38e-7 imp:n=1 $Nb cladding
1083    3 -0.08866
        -12 u=18 tmp=1.38e-7 imp:n=1 $Sodium coolant
c
c end cell specification
```



```

3335 2 -8.4 +1 +2 +3 -4 +34 -35 imp:n=1
c 3335 4 0.046299 +1 +2 +3 -4 +34 -35 imp:n=1
3333 1 -3.01 +1 +2 +3 -4 -33 +35
      imp:n=1 $ radial reflector
9999 0 (-1:-2:-3:+4:+33) imp:n=0 $ void
c

c surface specification
c
12 rpp -0.184475 0.184475 -0.184475 0.184475 -100 100
13 rpp -0.193015 0.193015 -0.193015 0.193015 -100 100
14 rpp -0.275000 0.275000 -0.275000 0.275000 -100 100
c
21 rpp 0 12.925 0 12.925 0 6 $ reflector bottom
22 rpp 0 12.925 0 12.925 6 14.3333 $ core lower
23 rpp 0 12.925 0 12.925 14.3333 22.8633 $ core middle
24 rpp 0 12.925 0 12.925 22.8633 31.3 $ core higher
25 rpp 0 12.925 0 12.925 31.3 37.3 $ reflector top
20 rpp 0 12.925 0 12.925 0 37.3 $ whole core
c
*1 p 1 -1 0 0 $ symmetry
*2 py 1e-5 $ symmetry
3 pz 0 $ lower z plane (below reflector)
4 pz 37.3 $ upper z plane (above reflector)
c
c radial reflector
c
33 cz 25 $ radial reflector
34 rpp 0 13.1 0 13.1 0 37.3 $ cladding
35 rpp 0 13.6 0 13.6 0 37.3 $ sheild
c
c
c end surface specification

c materials specification
c
m1 04009.60c 0.5
    08016.60c 0.5 $ BeO Reflector
m2 41093.60c -0.99 $ Nb (93) cladding
    40000.60c -0.01 $ 1 w/o Zr
m3 11023.50c 1.0 $ Sodium Coolant
m4 48000.50c 1.0
c 48106.50c 0.000579
c 48108.50c 0.000412
c 48110.50c 0.005783
c 48111.50c 0.005926
c 48112.50c 0.011172
c 48113.50c 0.005658
c 48114.50c 0.013302
c 48116.50c 0.003468
m101 006000.50c 0.029741 $ Carbon in U-Carbide
      38088.96c 1.0000e-24 $ begin_mcode_FP
      39089.60c 1.0000e-24
      42095.50c 1.0000e-24
      42097.60c 1.0000e-24
      42098.50c 1.0000e-24
      43099.50c 1.0000e-24
      42100.50c 1.0000e-24
      44101.50c 1.0000e-24
      44102.60c 1.0000e-24
      45103.50c 1.0000e-24
      44104.96c 1.0000e-24
      46105.50c 1.0000e-24
      46106.96c 1.0000e-24
      46108.50c 1.0000e-24
      47109.60c 1.0000e-24
      53129.60c 1.0000e-24
      52130.96c 1.0000e-24
      54131.50c 1.0000e-24
      54132.96c 1.0000e-24
      55133.60c 1.0000e-24

```

	54134.35c	1.0000e-24	
	55135.60c	1.0000e-24	
	54136.96c	1.0000e-24	
	55137.60c	1.0000e-24	
	56138.60c	1.0000e-24	
	57139.60c	1.0000e-24	
	58140.96c	1.0000e-24	
	59141.50c	1.0000e-24	
	58142.96c	1.0000e-24	
	60143.50c	1.0000e-24	
	60144.96c	1.0000e-24	
	60145.50c	1.0000e-24	
	60146.96c	1.0000e-24	
	61147.50c	1.0000e-24	
	61148.50c	1.0000e-24	
	61149.50c	1.0000e-24	
	62147.50c	1.0000e-24	
	60148.50c	1.0000e-24	
	62149.50c	1.0000e-24	
	62151.50c	1.0000e-24	
	63151.60c	1.0000e-24	
	63153.60c	1.0000e-24	\$ end_mcode_FP
	90232.60c	1.0000E-24	\$ begin_mcode_ACT
	90233.35c	1.0000E-24	
	91231.60c	1.0000E-24	
	91233.50c	1.0000E-24	
	92232.60c	1.0000E-24	
	92233.60c	1.0000e-24	
	92234.60c	1.0000e-24	
	92235.60c	0.02884905	
	92236.60c	1.0000E-24	
	92237.50c	1.0000E-24	
	92238.60c	8.9224e-4	
	92239.35c	1.0000E-24	
	93235.35c	1.0000E-24	
	93236.35c	1.0000E-24	
	93237.60c	1.0000E-24	
	93238.35c	1.0000E-24	
	94237.60c	1.0000E-24	
	94238.60c	1.0000E-24	\$ fuel Pu238
	94239.60c	1.0000E-24	\$ fuel Pu239
	94240.60c	1.0000E-24	\$ fuel Pu240
	94241.60c	1.0000E-24	\$ fuel Pu241
	94242.60c	1.0000E-24	\$ fuel Pu242
	95241.60c	1.0000E-24	\$ fuel Am241
	95242.96c	1.0000e-24	
	95243.60c	1.0000E-24	
	96242.60c	1.0000e-24	
	96243.60c	1.0000e-24	
	96244.60c	1.0000E-24	
	96245.60c	1.0000E-24	\$ end_mcode_ACT
m102	006000.50c	0.029741	\$ Carbon in U-Carbide
	38088.96c	1.0000e-24	\$ begin_mcode_FP
	39089.60c	1.0000e-24	
	42095.50c	1.0000e-24	
	42097.60c	1.0000e-24	
	42098.50c	1.0000e-24	
	43099.50c	1.0000e-24	
	42100.50c	1.0000e-24	
	44101.50c	1.0000e-24	
	44102.60c	1.0000e-24	
	45103.50c	1.0000e-24	
	44104.96c	1.0000e-24	
	46105.50c	1.0000e-24	
	46106.96c	1.0000e-24	
	46108.50c	1.0000e-24	
	47109.60c	1.0000e-24	
	53129.60c	1.0000e-24	
	52130.96c	1.0000e-24	
	54131.50c	1.0000e-24	
	54132.96c	1.0000e-24	

	55133.60c	1.0000e-24	
	54134.35c	1.0000e-24	
	55135.60c	1.0000e-24	
	54136.96c	1.0000e-24	
	55137.60c	1.0000e-24	
	56138.60c	1.0000e-24	
	57139.60c	1.0000e-24	
	58140.96c	1.0000e-24	
	59141.50c	1.0000e-24	
	58142.96c	1.0000e-24	
	60143.50c	1.0000e-24	
	60144.96c	1.0000e-24	
	60145.50c	1.0000e-24	
	60146.96c	1.0000e-24	
	61147.50c	1.0000e-24	
	61148.50c	1.0000e-24	
	61149.50c	1.0000e-24	
	62147.50c	1.0000e-24	
	60148.50c	1.0000e-24	
	62149.50c	1.0000e-24	
	62151.50c	1.0000e-24	
	63151.60c	1.0000e-24	
	63153.60c	1.0000e-24	\$ end_mcode_FP
	90232.60c	1.0000E-24	\$ begin_mcode_ACT
	90233.35c	1.0000E-24	
	91231.60c	1.0000E-24	
	91233.50c	1.0000E-24	
	92232.60c	1.0000E-24	
	92233.60c	1.0000e-24	
	92234.60c	1.0000e-24	
	92235.60c	0.0208189	
	92236.60c	1.0000E-24	
	92237.50c	1.0000E-24	
	92238.60c	0.0089224	
	92239.35c	1.0000E-24	
	93235.35c	1.0000E-24	
	93236.35c	1.0000E-24	
	93237.60c	1.0000E-24	
	93238.35c	1.0000E-24	
	94237.60c	1.0000E-24	
	94238.60c	1.0000E-24	\$ fuel Pu238
	94239.60c	1.0000E-24	\$ fuel Pu239
	94240.60c	1.0000E-24	\$ fuel Pu240
	94241.60c	1.0000E-24	\$ fuel Pu241
	94242.60c	1.0000E-24	\$ fuel Pu242
	95241.60c	1.0000E-24	\$ fuel Am241
	95242.96c	1.0000e-24	
	95243.60c	1.0000E-24	
	96242.60c	1.0000e-24	
	96243.60c	1.0000e-24	
	96244.60c	1.0000E-24	
	96245.60c	1.0000e-24	\$ end_mcode_ACT
m103	006000.50c	0.029741	\$ Carbon in U-Carbide
	38088.96c	1.0000e-24	\$ begin_mcode_FP
	39089.60c	1.0000e-24	
	42095.50c	1.0000e-24	
	42097.60c	1.0000e-24	
	42098.50c	1.0000e-24	
	43099.50c	1.0000e-24	
	42100.50c	1.0000e-24	
	44101.50c	1.0000e-24	
	44102.60c	1.0000e-24	
	45103.50c	1.0000e-24	
	44104.96c	1.0000e-24	
	46105.50c	1.0000e-24	
	46106.96c	1.0000e-24	
	46108.50c	1.0000e-24	
	47109.60c	1.0000e-24	
	53129.60c	1.0000e-24	
	52130.96c	1.0000e-24	
	54131.50c	1.0000e-24	

	54132.96c	1.0000e-24	
	55133.60c	1.0000e-24	
	54134.35c	1.0000e-24	
	55135.60c	1.0000e-24	
	54136.96c	1.0000e-24	
	55137.60c	1.0000e-24	
	56138.60c	1.0000e-24	
	57139.60c	1.0000e-24	
	58140.96c	1.0000e-24	
	59141.50c	1.0000e-24	
	58142.96c	1.0000e-24	
	60143.50c	1.0000e-24	
	60144.96c	1.0000e-24	
	60145.50c	1.0000e-24	
	60146.96c	1.0000e-24	
	61147.50c	1.0000e-24	
	61148.50c	1.0000e-24	
	61149.50c	1.0000e-24	
	62147.50c	1.0000e-24	
	60148.50c	1.0000e-24	
	62149.50c	1.0000e-24	
	62151.50c	1.0000e-24	
	63151.60c	1.0000e-24	
	63153.60c	1.0000e-24	\$ end_mcode_FP
	90232.60c	1.0000E-24	\$ begin_mcode_ACT
	90233.35c	1.0000E-24	
	91231.60c	1.0000E-24	
	91233.50c	1.0000E-24	
	92232.60c	1.0000E-24	
	92233.60c	1.0000e-24	
	92234.60c	1.0000e-24	
	92235.60c	0.02884905	
	92236.60c	1.0000E-24	
	92237.50c	1.0000E-24	
	92238.60c	8.9224e-4	
	92239.35c	1.0000E-24	
	93235.35c	1.0000E-24	
	93236.35c	1.0000E-24	
	93237.60c	1.0000E-24	
	93238.35c	1.0000E-24	
	94237.60c	1.0000E-24	
	94238.60c	1.0000E-24	\$ fuel Pu238
	94239.60c	1.0000E-24	\$ fuel Pu239
	94240.60c	1.0000E-24	\$ fuel Pu240
	94241.60c	1.0000E-24	\$ fuel Pu241
	94242.60c	1.0000E-24	\$ fuel Pu242
	95241.60c	1.0000E-24	\$ fuel Am241
	95242.96c	1.0000e-24	
	95243.60c	1.0000E-24	
	96242.60c	1.0000e-24	
	96243.60c	1.0000e-24	
	96244.60c	1.0000E-24	
	96245.60c	1.0000e-24	\$ end_mcode_ACT
m104	006000.50c	0.029741	\$ Carbon in U-Carbide
	38088.96c	1.0000e-24	\$ begin_mcode_FP
	39089.60c	1.0000e-24	
	42095.50c	1.0000e-24	
	42097.60c	1.0000e-24	
	42098.50c	1.0000e-24	
	43099.50c	1.0000e-24	
	42100.50c	1.0000e-24	
	44101.50c	1.0000e-24	
	44102.60c	1.0000e-24	
	45103.50c	1.0000e-24	
	44104.96c	1.0000e-24	
	46105.50c	1.0000e-24	
	46106.96c	1.0000e-24	
	46108.50c	1.0000e-24	
	47109.60c	1.0000e-24	
	53129.60c	1.0000e-24	
	52130.96c	1.0000e-24	

	54131.50c	1.0000e-24	
	54132.96c	1.0000e-24	
	55133.60c	1.0000e-24	
	54134.35c	1.0000e-24	
	55135.60c	1.0000e-24	
	54136.96c	1.0000e-24	
	55137.60c	1.0000e-24	
	56138.60c	1.0000e-24	
	57139.60c	1.0000e-24	
	58140.96c	1.0000e-24	
	59141.50c	1.0000e-24	
	58142.96c	1.0000e-24	
	60143.50c	1.0000e-24	
	60144.96c	1.0000e-24	
	60145.50c	1.0000e-24	
	60146.96c	1.0000e-24	
	61147.50c	1.0000e-24	
	61148.50c	1.0000e-24	
	61149.50c	1.0000e-24	
	62147.50c	1.0000e-24	
	60148.50c	1.0000e-24	
	62149.50c	1.0000e-24	
	62151.50c	1.0000e-24	
	63151.60c	1.0000e-24	
	63153.60c	1.0000e-24	\$ end_mcode_FP
	90232.60c	1.0000E-24	\$ begin_mcode_ACT
	90233.35c	1.0000E-24	
	91231.60c	1.0000E-24	
	91233.50c	1.0000E-24	
	92232.60c	1.0000E-24	
	92233.60c	1.0000e-24	
	92234.60c	1.0000e-24	
	92235.60c	0.0208189	
	92236.60c	1.0000E-24	
	92237.50c	1.0000E-24	
	92238.60c	0.0089224	
	92239.35c	1.0000E-24	
	93235.35c	1.0000E-24	
	93236.35c	1.0000E-24	
	93237.60c	1.0000E-24	
	93238.35c	1.0000E-24	
	94237.60c	1.0000E-24	
	94238.60c	1.0000E-24	\$ fuel Pu238
	94239.60c	1.0000E-24	\$ fuel Pu239
	94240.60c	1.0000E-24	\$ fuel Pu240
	94241.60c	1.0000E-24	\$ fuel Pu241
	94242.60c	1.0000E-24	\$ fuel Pu242
	95241.60c	1.0000E-24	\$ fuel Am241
	95242.96c	1.0000e-24	
	95243.60c	1.0000E-24	
	96242.60c	1.0000e-24	
	96243.60c	1.0000e-24	
	96244.60c	1.0000E-24	
	96245.60c	1.0000e-24	\$ end_mcode_ACT
m105	006000.50c	0.029741	\$ Carbon in U-Carbide
	38088.96c	1.0000e-24	\$ begin_mcode_FP
	39089.60c	1.0000e-24	
	42095.50c	1.0000e-24	
	42097.60c	1.0000e-24	
	42098.50c	1.0000e-24	
	43099.50c	1.0000e-24	
	42100.50c	1.0000e-24	
	44101.50c	1.0000e-24	
	44102.60c	1.0000e-24	
	45103.50c	1.0000e-24	
	44104.96c	1.0000e-24	
	46105.50c	1.0000e-24	
	46106.96c	1.0000e-24	
	46108.50c	1.0000e-24	
	47109.60c	1.0000e-24	
	53129.60c	1.0000e-24	

	52130.96c	1.0000e-24	
	54131.50c	1.0000e-24	
	54132.96c	1.0000e-24	
	55133.60c	1.0000e-24	
	54134.35c	1.0000e-24	
	55135.60c	1.0000e-24	
	54136.96c	1.0000e-24	
	55137.60c	1.0000e-24	
	56138.60c	1.0000e-24	
	57139.60c	1.0000e-24	
	58140.96c	1.0000e-24	
	59141.50c	1.0000e-24	
	58142.96c	1.0000e-24	
	60143.50c	1.0000e-24	
	60144.96c	1.0000e-24	
	60145.50c	1.0000e-24	
	60146.96c	1.0000e-24	
	61147.50c	1.0000e-24	
	61148.50c	1.0000e-24	
	61149.50c	1.0000e-24	
	62147.50c	1.0000e-24	
	60148.50c	1.0000e-24	
	62149.50c	1.0000e-24	
	62151.50c	1.0000e-24	
	63151.60c	1.0000e-24	
	63153.60c	1.0000e-24	\$ end_mcode_FP
	90232.60c	1.0000E-24	\$ begin_mcode_ACT
	90233.35c	1.0000E-24	
	91231.60c	1.0000E-24	
	91233.50c	1.0000E-24	
	92232.60c	1.0000E-24	
	92233.60c	1.0000e-24	
	92234.60c	1.0000e-24	
	92235.60c	0.02884905	
	92236.60c	1.0000E-24	
	92237.50c	1.0000E-24	
	92238.60c	8.9224e-4	
	92239.35c	1.0000E-24	
	93235.35c	1.0000E-24	
	93236.35c	1.0000E-24	
	93237.60c	1.0000E-24	
	93238.35c	1.0000E-24	
	94237.60c	1.0000E-24	
	94238.60c	1.0000E-24	\$ fuel Pu238
	94239.60c	1.0000E-24	\$ fuel Pu239
	94240.60c	1.0000E-24	\$ fuel Pu240
	94241.60c	1.0000E-24	\$ fuel Pu241
	94242.60c	1.0000E-24	\$ fuel Pu242
	95241.60c	1.0000E-24	\$ fuel Am241
	95242.96c	1.0000e-24	
	95243.60c	1.0000E-24	
	96242.60c	1.0000e-24	
	96243.60c	1.0000e-24	
	96244.60c	1.0000E-24	
	96245.60c	1.0000e-24	\$ end_mcode_ACT
m106	006000.50c	0.029741	\$ Carbon in U-Carbide
	38088.96c	1.0000e-24	\$ begin_mcode_FP
	39089.60c	1.0000e-24	
	42095.50c	1.0000e-24	
	42097.60c	1.0000e-24	
	42098.50c	1.0000e-24	
	43099.50c	1.0000e-24	
	42100.50c	1.0000e-24	
	44101.50c	1.0000e-24	
	44102.60c	1.0000e-24	
	45103.50c	1.0000e-24	
	44104.96c	1.0000e-24	
	46105.50c	1.0000e-24	
	46106.96c	1.0000e-24	
	46108.50c	1.0000e-24	
	47109.60c	1.0000e-24	

	53129.60c	1.0000e-24	
	52130.96c	1.0000e-24	
	54131.50c	1.0000e-24	
	54132.96c	1.0000e-24	
	55133.60c	1.0000e-24	
	54134.35c	1.0000e-24	
	55135.60c	1.0000e-24	
	54136.96c	1.0000e-24	
	55137.60c	1.0000e-24	
	56138.60c	1.0000e-24	
	57139.60c	1.0000e-24	
	58140.96c	1.0000e-24	
	59141.50c	1.0000e-24	
	58142.96c	1.0000e-24	
	60143.50c	1.0000e-24	
	60144.96c	1.0000e-24	
	60145.50c	1.0000e-24	
	60146.96c	1.0000e-24	
	61147.50c	1.0000e-24	
	61148.50c	1.0000e-24	
	61149.50c	1.0000e-24	
	62147.50c	1.0000e-24	
	60148.50c	1.0000e-24	
	62149.50c	1.0000e-24	
	62151.50c	1.0000e-24	
	63151.60c	1.0000e-24	
	63153.60c	1.0000e-24	\$ end_mcode_FP
	90232.60c	1.0000E-24	\$ begin_mcode_ACT
	90233.35c	1.0000E-24	
	91231.60c	1.0000E-24	
	91233.50c	1.0000E-24	
	92232.60c	1.0000E-24	
	92233.60c	1.0000e-24	
	92234.60c	1.0000e-24	
	92235.60c	0.0208189	
	92236.60c	1.0000E-24	
	92237.50c	1.0000E-24	
	92238.60c	0.0089224	
	92239.35c	1.0000E-24	
	93235.35c	1.0000E-24	
	93236.35c	1.0000E-24	
	93237.60c	1.0000E-24	
	93238.35c	1.0000E-24	
	94237.60c	1.0000E-24	
	94238.60c	1.0000E-24	\$ fuel Pu238
	94239.60c	1.0000E-24	\$ fuel Pu239
	94240.60c	1.0000E-24	\$ fuel Pu240
	94241.60c	1.0000E-24	\$ fuel Pu241
	94242.60c	1.0000E-24	\$ fuel Pu242
	95241.60c	1.0000E-24	\$ fuel Am241
	95242.96c	1.0000e-24	
	95243.60c	1.0000E-24	
	96242.60c	1.0000e-24	
	96243.60c	1.0000e-24	
	96244.60c	1.0000E-24	
	96245.60c	1.0000e-24	\$ end_mcode_ACT
m107	006000.50c	0.029741	\$ Carbon in U-Carbide
	38088.96c	1.0000e-24	\$ begin_mcode_FP
	39089.60c	1.0000e-24	
	42095.50c	1.0000e-24	
	42097.60c	1.0000e-24	
	42098.50c	1.0000e-24	
	43099.50c	1.0000e-24	
	42100.50c	1.0000e-24	
	44101.50c	1.0000e-24	
	44102.60c	1.0000e-24	
	45103.50c	1.0000e-24	
	44104.96c	1.0000e-24	
	46105.50c	1.0000e-24	
	46106.96c	1.0000e-24	
	46108.50c	1.0000e-24	

	47109.60c	1.0000e-24	
	53129.60c	1.0000e-24	
	52130.96c	1.0000e-24	
	54131.50c	1.0000e-24	
	54132.96c	1.0000e-24	
	55133.60c	1.0000e-24	
	54134.35c	1.0000e-24	
	55135.60c	1.0000e-24	
	54136.96c	1.0000e-24	
	55137.60c	1.0000e-24	
	56138.60c	1.0000e-24	
	57139.60c	1.0000e-24	
	58140.96c	1.0000e-24	
	59141.50c	1.0000e-24	
	58142.96c	1.0000e-24	
	60143.50c	1.0000e-24	
	60144.96c	1.0000e-24	
	60145.50c	1.0000e-24	
	60146.96c	1.0000e-24	
	61147.50c	1.0000e-24	
	61148.50c	1.0000e-24	
	61149.50c	1.0000e-24	
	62147.50c	1.0000e-24	
	60148.50c	1.0000e-24	
	62149.50c	1.0000e-24	
	62151.50c	1.0000e-24	
	63151.60c	1.0000e-24	
	63153.60c	1.0000e-24	\$ end_mcode_FP
	90232.60c	1.0000E-24	\$ begin_mcode_ACT
	90233.35c	1.0000E-24	
	91231.60c	1.0000E-24	
	91233.50c	1.0000E-24	
	92232.60c	1.0000E-24	
	92233.60c	1.0000e-24	
	92234.60c	1.0000e-24	
	92235.60c	0.0208189	
	92236.60c	1.0000E-24	
	92237.50c	1.0000E-24	
	92238.60c	0.0089224	
	92239.35c	1.0000E-24	
	93235.35c	1.0000E-24	
	93236.35c	1.0000E-24	
	93237.60c	1.0000E-24	
	93238.35c	1.0000E-24	
	94237.60c	1.0000E-24	
	94238.60c	1.0000E-24	\$ fuel Pu238
	94239.60c	1.0000E-24	\$ fuel Pu239
	94240.60c	1.0000E-24	\$ fuel Pu240
	94241.60c	1.0000E-24	\$ fuel Pu241
	94242.60c	1.0000E-24	\$ fuel Pu242
	95241.60c	1.0000E-24	\$ fuel Am241
	95242.96c	1.0000e-24	
	95243.60c	1.0000E-24	
	96242.60c	1.0000e-24	
	96243.60c	1.0000e-24	
	96244.60c	1.0000E-24	
	96245.60c	1.0000e-24	\$ end_mcode_ACT
m108	006000.50c	0.029741	\$ Carbon in U-Carbide
	38088.96c	1.0000e-24	\$ begin_mcode_FP
	39089.60c	1.0000e-24	
	42095.50c	1.0000e-24	
	42097.60c	1.0000e-24	
	42098.50c	1.0000e-24	
	43099.50c	1.0000e-24	
	42100.50c	1.0000e-24	
	44101.50c	1.0000e-24	
	44102.60c	1.0000e-24	
	45103.50c	1.0000e-24	
	44104.96c	1.0000e-24	
	46105.50c	1.0000e-24	
	46106.96c	1.0000e-24	

```

46108.50c 1.0000e-24
47109.60c 1.0000e-24
53129.60c 1.0000e-24
52130.96c 1.0000e-24
54131.50c 1.0000e-24
54132.96c 1.0000e-24
55133.60c 1.0000e-24
54134.35c 1.0000e-24
55135.60c 1.0000e-24
54136.96c 1.0000e-24
55137.60c 1.0000e-24
56138.60c 1.0000e-24
57139.60c 1.0000e-24
58140.96c 1.0000e-24
59141.50c 1.0000e-24
58142.96c 1.0000e-24
60143.50c 1.0000e-24
60144.96c 1.0000e-24
60145.50c 1.0000e-24
60146.96c 1.0000e-24
61147.50c 1.0000e-24
61148.50c 1.0000e-24
61149.50c 1.0000e-24
62147.50c 1.0000e-24
60148.50c 1.0000e-24
62149.50c 1.0000e-24
62151.50c 1.0000e-24
63151.60c 1.0000e-24
63153.60c 1.0000e-24 $ end_mcode_FP
90232.60c 1.0000E-24 $ begin_mcode_ACT
90233.35c 1.0000E-24
91231.60c 1.0000E-24
91233.50c 1.0000E-24
92232.60c 1.0000E-24
92233.60c 1.0000e-24
92234.60c 1.0000e-24
92235.60c 0.02884905
92236.60c 1.0000E-24
92237.50c 1.0000E-24
92238.60c 8.9224e-4
92239.35c 1.0000E-24
93235.35c 1.0000E-24
93236.35c 1.0000E-24
93237.60c 1.0000E-24
93238.35c 1.0000E-24
94237.60c 1.0000E-24
94238.60c 1.0000E-24 $ fuel Pu238
94239.60c 1.0000E-24 $ fuel Pu239
94240.60c 1.0000E-24 $ fuel Pu240
94241.60c 1.0000E-24 $ fuel Pu241
94242.60c 1.0000E-24 $ fuel Pu242
95241.60c 1.0000E-24 $ fuel Am241
95242.96c 1.0000e-24
95243.60c 1.0000E-24
96242.60c 1.0000e-24
96243.60c 1.0000e-24
96244.60c 1.0000E-24
96245.60c 1.0000e-24 $ end_mcode_ACT
c
c end materials specification
c
ksrc 3.3 2.5 18.65
mode n
kcode 1200 1.00 200 1200
prdmp 1200 1200 1200
print
f114:n 1031 1021 1041 1051 1061 1071
e114:n 1.000E-11 6.220E-10 6.874E-10 7.597E-10 8.396E-10 9.279E-10
1.026E-09 1.133E-09 1.253E-09 1.384E-09 1.530E-09 1.691E-09
1.869E-09 2.065E-09 2.282E-09 2.522E-09 2.788E-09 3.081E-09
3.405E-09 3.763E-09 4.159E-09 4.596E-09 5.079E-09 5.614E-09

```

6.204E-09 6.856E-09 7.578E-09 8.374E-09 9.255E-09 1.023E-08
1.130E-08 1.249E-08 1.381E-08 1.526E-08 1.686E-08 1.864E-08
2.060E-08 2.276E-08 2.516E-08 2.780E-08 3.073E-08 3.396E-08
3.753E-08 4.148E-08 4.584E-08 5.066E-08 5.599E-08 6.188E-08
6.839E-08 7.558E-08 8.353E-08 9.231E-08 1.020E-07 1.128E-07
1.246E-07 1.377E-07 1.522E-07 1.682E-07 1.859E-07 2.054E-07
2.271E-07 2.509E-07 2.773E-07 3.065E-07 3.387E-07 3.743E-07
4.137E-07 4.572E-07 5.053E-07 5.585E-07 6.172E-07 6.821E-07
7.538E-07 8.331E-07 9.207E-07 1.018E-06 1.125E-06 1.243E-06
1.374E-06 1.518E-06 1.678E-06 1.854E-06 2.049E-06 2.265E-06
2.503E-06 2.766E-06 3.057E-06 3.378E-06 3.734E-06 4.126E-06
4.560E-06 5.040E-06 5.570E-06 6.156E-06 6.803E-06 7.519E-06
8.310E-06 9.184E-06 1.015E-05 1.122E-05 1.240E-05 1.370E-05
1.514E-05 1.673E-05 1.849E-05 2.044E-05 2.259E-05 2.496E-05
2.759E-05 3.049E-05 3.370E-05 3.724E-05 4.116E-05 4.549E-05
5.027E-05 5.556E-05 6.140E-05 6.786E-05 7.500E-05 8.288E-05
9.160E-05 1.012E-04 1.119E-04 1.236E-04 1.367E-04 1.510E-04
1.669E-04 1.845E-04 2.039E-04 2.253E-04 2.490E-04 2.752E-04
3.041E-04 3.361E-04 3.715E-04 4.105E-04 4.537E-04 5.014E-04
5.541E-04 6.124E-04 6.768E-04 7.480E-04 8.267E-04 9.136E-04
1.010E-03 1.116E-03 1.233E-03 1.363E-03 1.506E-03 1.665E-03
1.840E-03 2.033E-03 2.247E-03 2.484E-03 2.745E-03 3.033E-03
3.352E-03 3.705E-03 4.095E-03 4.525E-03 5.001E-03 5.527E-03
6.108E-03 6.751E-03 7.461E-03 8.246E-03 9.113E-03 1.007E-02
1.113E-02 1.230E-02 1.359E-02 1.502E-02 1.660E-02 1.835E-02
2.028E-02 2.241E-02 2.477E-02 2.738E-02 3.026E-02 3.344E-02
3.695E-02 4.084E-02 4.514E-02 4.988E-02 5.513E-02 6.093E-02
6.733E-02 7.442E-02 8.224E-02 9.089E-02 1.005E-01 1.110E-01
1.227E-01 1.356E-01 1.499E-01 1.656E-01 1.830E-01 2.023E-01
2.236E-01 2.471E-01 2.731E-01 3.018E-01 3.335E-01 3.686E-01
4.074E-01 4.502E-01 4.975E-01 5.499E-01 6.077E-01 6.716E-01
7.422E-01 8.203E-01 9.066E-01 1.002E+00 1.107E+00 1.224E+00
1.352E+00 1.495E+00 1.652E+00 1.826E+00 2.018E+00 2.230E+00
2.464E+00 2.724E+00 3.010E+00 3.326E+00 3.676E+00 4.063E+00
4.490E+00 4.963E+00 5.484E+00 6.061E+00 6.699E+00 7.403E+00
8.182E+00 9.042E+00 1.000E+01 1.105E+01 1.221E+01 1.350E+01
1.492E+01 1.649E+01 1.822E+01 2.000E+01

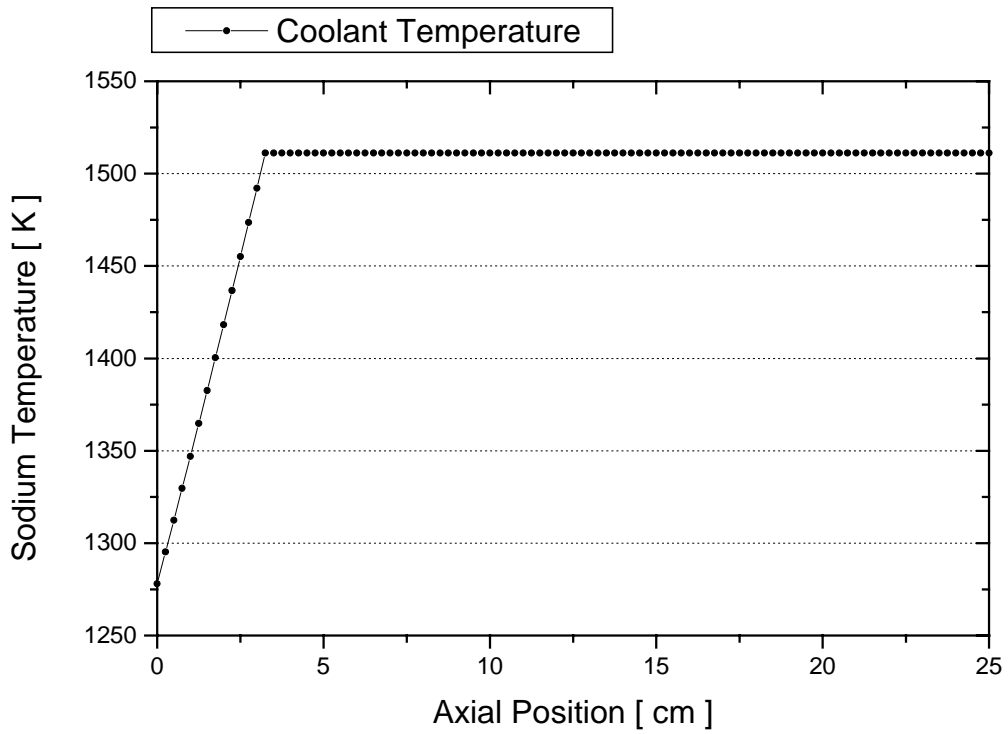
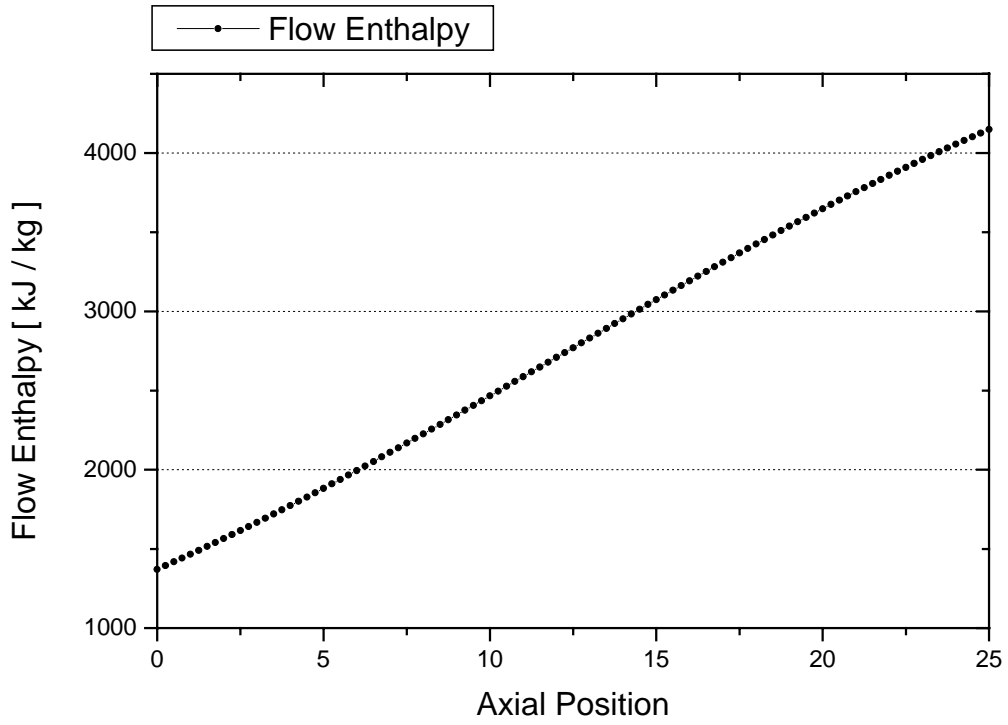
16.2 Appendix B: SELENE-10-HT MCODE Input Deck

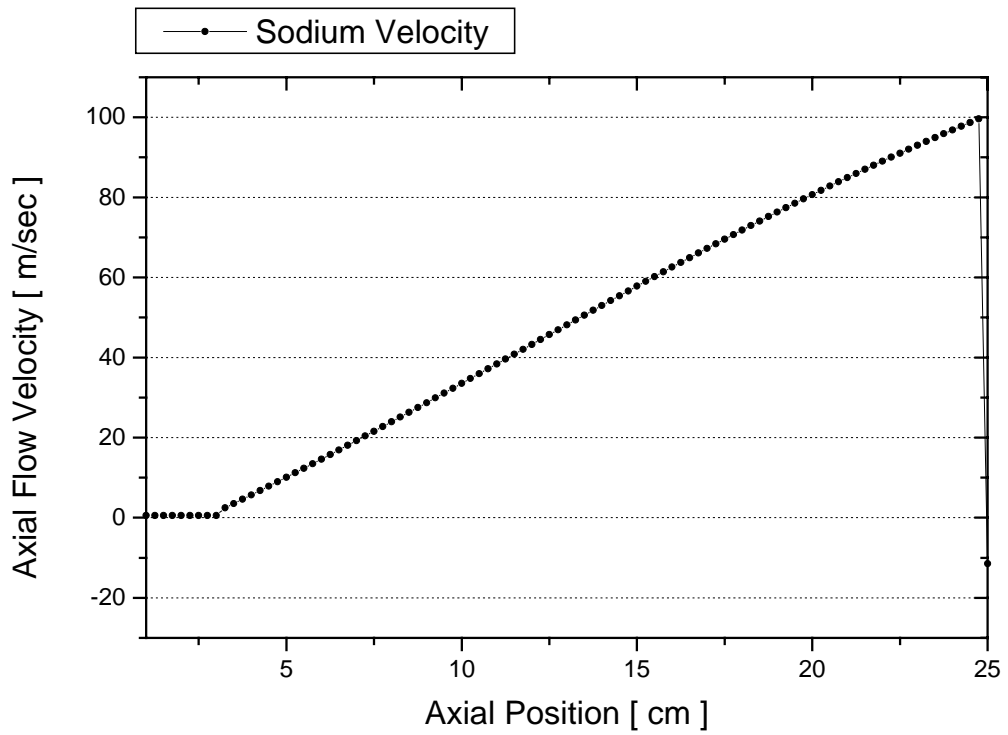
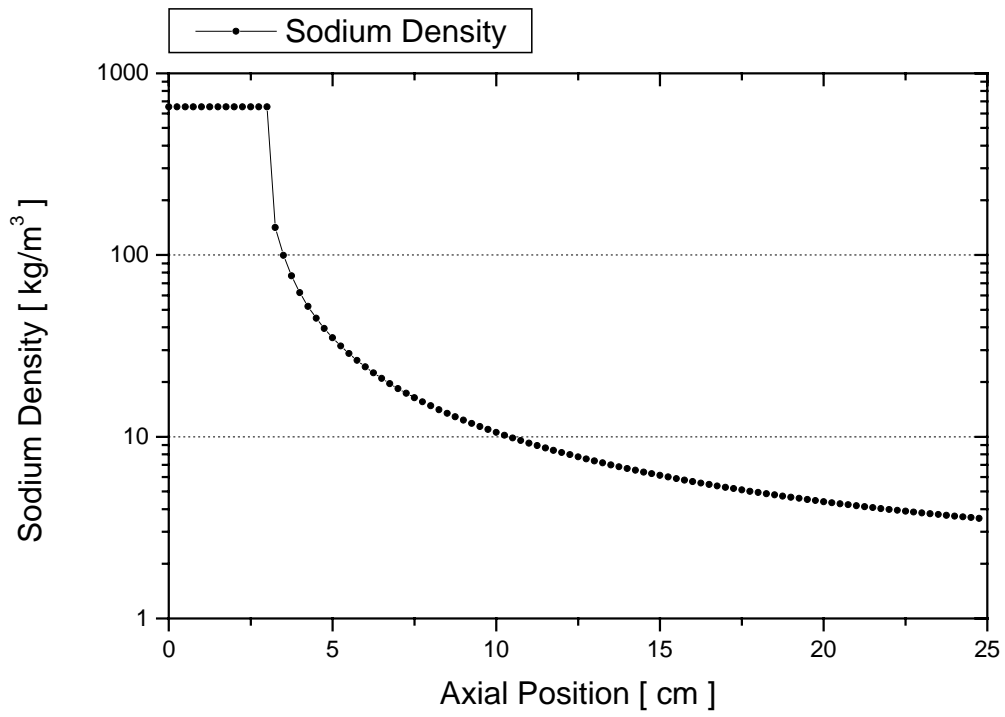
```

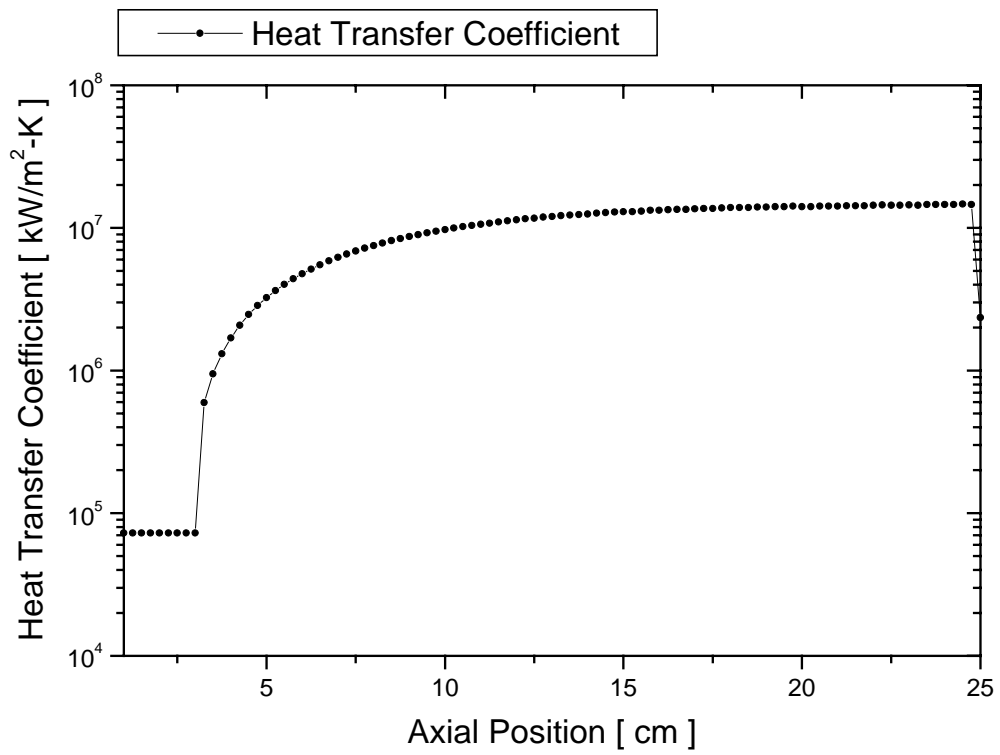
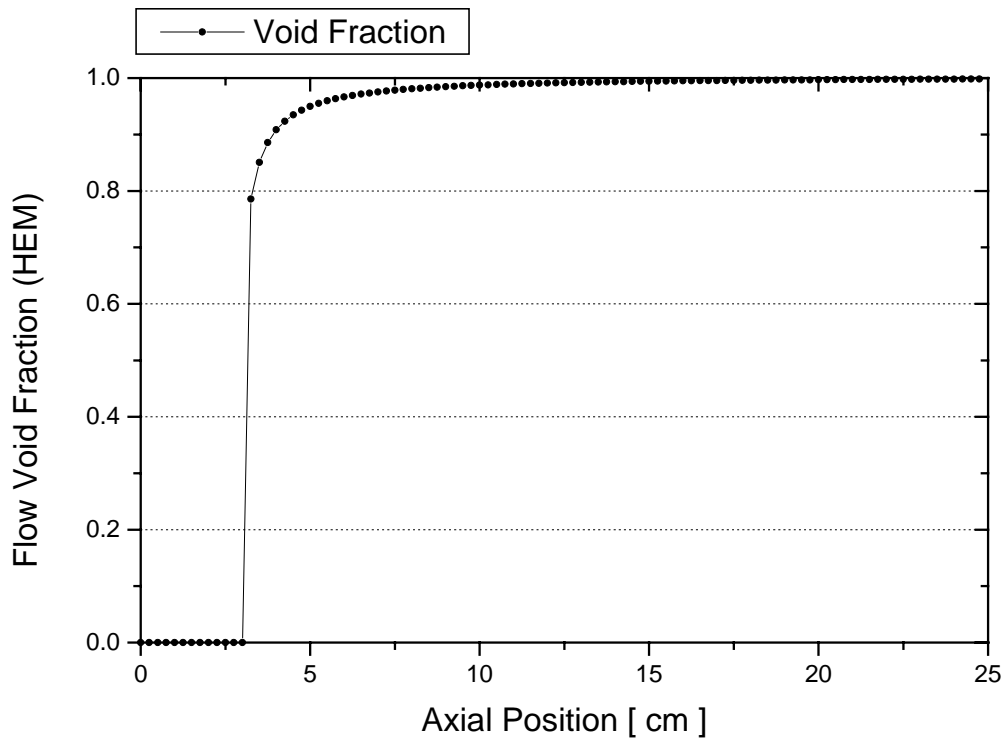
$ MCODE input file for HEU UHPDC
$ HEU Core burnup$ defines title
$ CTRL command initial-inp
MCD 0 mcnp.exe core $ MCNP files def. 0=start from ksrc source
$ ORIGEN-COMMAND ORIGEN-LIBRARIES
ORG /usr/local/bin/origen22/origen22 /usr/local/bin/origen22/LIBS DECA.Y.LIB GXUO2BRM.LIB
$ total# ID TYPE IHM(g) VOL(cm3)
CEL 8 1011 1 24173.25 2175.81 FFTFC.LIB
      1021 1 4946.916 445.267 FFTFC.LIB
      1031 1 24173.25 2175.81 FFTFC.LIB
      1041 1 4946.916 445.267 FFTFC.LIB
      1051 1 24173.25 2175.81 FFTFC.LIB
      1061 1 4946.916 445.267 FFTFC.LIB
      1071 1 172.5627 15.5322 FFTFC.LIB
      1081 1 172.5627 15.5322 FFTFC.LIB
$ total volume of fuel (cm3)
VOL 7870
$ normalization method, 1=flux, 2=power
NOR 1
$ predictor-corrector option, 1=P-C on, 0=P-C off
COR 0
$ core power density per liter of core volume, opt: WGU=W/gIHM, KWL=kW/(liter fuel)
PDE 1160 KWL
$points 0 1 2 3 4 5 6 7 8 9 10 11 12 13
DEP E 0 2 4 6 10 14 18 22 26 30 34 40 45 50
NMD 40 40 40 40 40 40 40 40 40 40 40 40 40 40
STA 0 $ starting point !!If first time, must start with 0
END 4 $ ending point

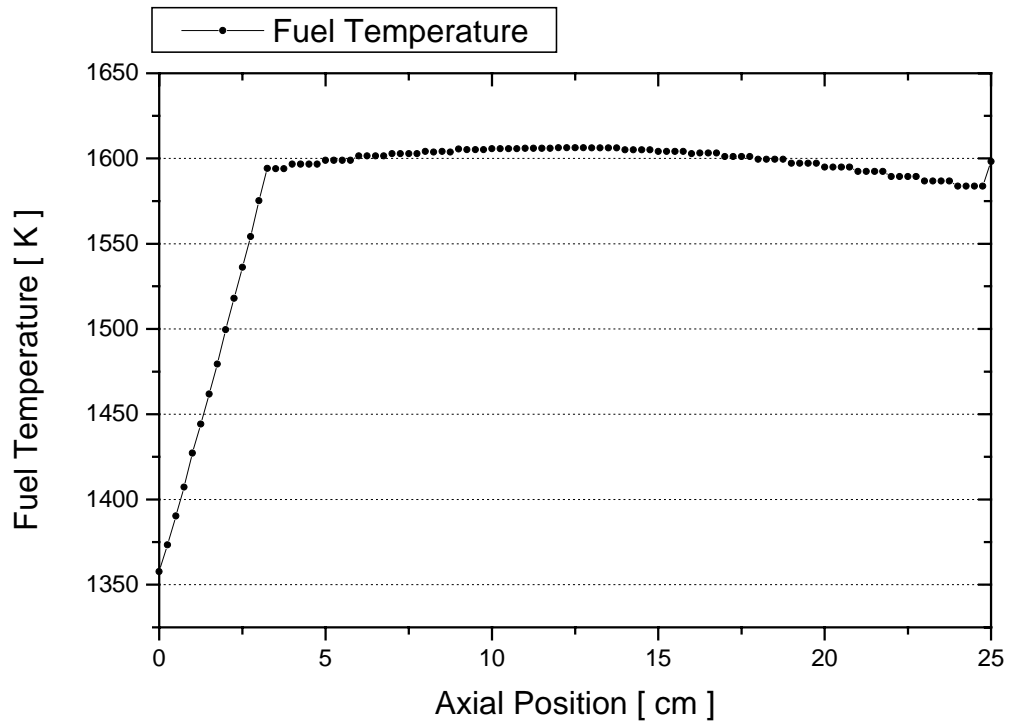
```

16.3 Appendix C: SELENE-30 Average Channel Thermal Hydraulic Data









16.4 Appendix D: SELENE-30 1.3PPF Hot Channel Thermal Hydraulic Data

